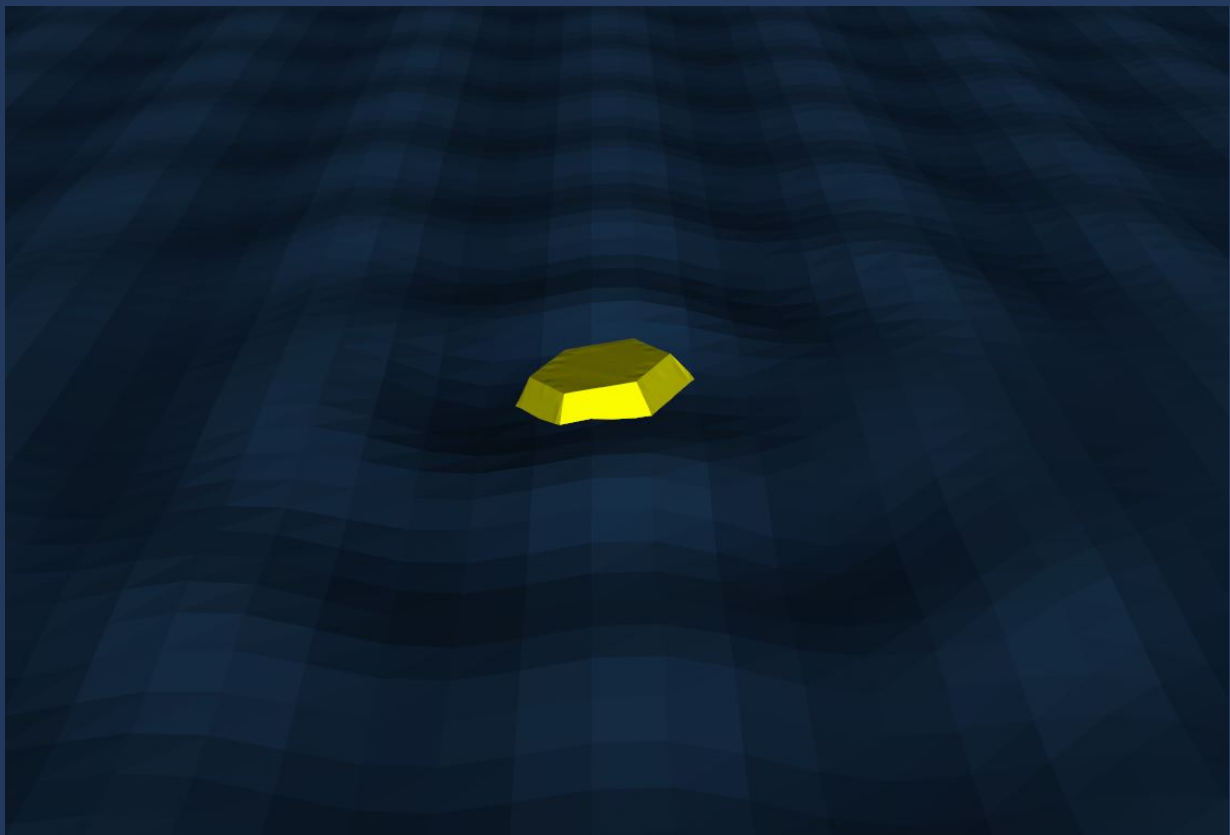


Developing a Wave Energy Converter in Offshore Environments with Sea Ice

Techno-Economic Assessment of a Point Absorber in Sea Ice

Alexander Kolset



Developing a Wave Energy Converter in Offshore Environments with Sea Ice

Techno-Economic Assessment of a Point Absorber in
Sea Ice

Thesis report

by

Alexander Kolset

to obtain the degree of Master of Science
at the Delft University of Technology
to be defended publicly on May 3, 2024 at 13:00

Thesis committee:

Chairman & Supervisor: Dr. George Lavidas

Supervisor: Dr. Ir. Hayo Hendrikse

Place: Faculty of Civil Engineering and Geosciences, Delft

Student number: 4468813

An electronic version of this thesis is available at <http://repository.tudelft.nl/>.

Abstract

In recent years, there has been growing interest in exploring the deployment of wave energy converters (WECs) in remote and harsh environments. However, research in this area remains limited, particularly concerning offshore environments with sea ice. This study focuses on investigating the energy production and economic feasibility of a point absorber in the Baltic Sea, specifically off the coast of Åland, which experiences seasonal ice cover. Four winter seasons with varying ice conditions are examined, ranging from ice-free to severe ice conditions. Additionally, the study aims to assess the survivability of the WEC under extreme level ice action and extreme wave conditions.

Based on literature review, a hexagonal slope-shaped buoy has shown promise in withstanding ice conditions up to 15 cm thickness in the Baltic Sea and is selected as the WEC design in this study. Metocean and sea ice data spanning from 2006 to 2021 are analysed from the NORA3 database. Through extreme value analysis, key parameters such as wave height, period, and ice thickness are determined. Survivability analysis is conducted to understand the forces exerted on the WEC during extreme ice load cases and extreme sea states. To evaluate energy production, hydrodynamic coefficients are computed using the Boundary Element Method solver Capytaine in the frequency domain. Subsequently, simulations are conducted using WEC-Sim to derive the power output of the WEC under varying sea states. Optimisation of the Power Take-Off (PTO) damping is performed to enhance performance for the specific site conditions. A comparison of power output is made among different WEC configurations with varying translator sizes.

The survivability analysis reveals important design considerations, especially regarding extreme ice conditions. When subjected to an extreme level ice thickness of 60 cm this results in calculated horizontal and vertical forces of 615 kN and 315 kN, respectively. In extreme sea states, simulations in WEC-Sim shows a maximum heave response of 4.16 m and a maximum heave force of 133 kN. Additionally, the investigation reveals significant fluctuations in wave energy converter (WEC) power production across the analysed winter seasons, characterised by varying ice conditions. During severe ice conditions (2009-2010), energy output decreased by nearly 50% compared to ice-free periods (2019-2020), potentially leading to a 95% increase in the levelised cost of energy (LCOE) if solely derived from that single season. These findings give valuable insights into the optimal WEC configuration, the maximising of power output and offer important considerations to WEC survivability for deployment in ice-covered regions.

Preface

As my studies at Delft draw to a close, I want to extend my heartfelt gratitude to those who have supported me along this journey. First and foremost, I am deeply thankful to Professor George Lavidas for his continued guidance, support, and expertise in this field of research. He helped me overcome many challenges throughout the writing of this thesis and I have learned a great deal. I would also like to express my appreciation to Professor Hayo Hendrikse for steering me in the right direction at the beginning of this thesis and getting me interested in the field of arctic engineering. I am grateful to my family for their unwavering support and encouragement, especially during difficult times. Additionally, I want to thank my friends for their moral support and all the good times we have together.

Alexander Kolset
March 2024, Delft

Contents

List of Figures	vi
List of Tables	viii
I Literature Review	1
1 Introduction	2
1.1 Background and Scope	2
1.2 Objectives and Motivation	2
1.3 Literature Review Methodology	2
1.4 Thesis Outline	3
2 Wave Energy and the Baltic Sea	4
2.1 Current State of Wave Energy Technology	4
2.2 Baltic Sea and its Characteristics	14
3 Research Proposal	17
3.1 Case Study: Project WESA	17
3.2 Site Selection	18
3.3 Research Questions	20
II Theoretical Background	21
4 Sea Ice: WEC Survivability and Energy Production	22
4.1 Ice Features	22
4.2 Effects of Sea Ice on Wave Energy	24
4.3 Ice Failure Mechanisms	24
4.4 Determining Design Ice Actions for Bending Failure	27
4.5 Buoy-Ice Interaction	29
5 Hydrodynamics of WECs	30
5.1 Linear Potential Flow Theory	30
5.2 Equation of Motion for a WEC	35
5.3 Response Amplitude Operator	39
5.4 Power Absorption	39
5.5 Time-domain modelling	40
III Methodology	42
6 Metocean and Ice Data	43
6.1 Extracting Time Series of Data	43
6.2 Sea Ice Statistics	48
6.3 Wave Scatter Diagrams	51
6.4 Extreme Value Analysis	57
7 Numerical Modelling	61
7.1 Overview of WEC-Sim	61
7.2 Geometry	62
7.3 Boundary Element Method and Capytaine	64
7.4 Running WEC-Sim	66

7.5	Verification	68
IV	Results	75
8	Results and Discussion	76
8.1	WEC Survivability	76
8.2	Mean Annual Energy Production	80
8.3	Optimising power production.	80
8.4	Seasonal Variability	90
8.5	Economics	92
V	Conclusion	95
9	Conclusion & Recommendations	96
9.1	Conclusion	96
9.2	Recommendations	97
	References	102
A	Ice Interaction Local Forces	103
A.1	Buoy-Ice interaction (project WESA)	103
B	Capytaine and BEMIO	106
C	WEC-Sim	108
D	Wave Scatter Diagrams	110

Nomenclature

List of Abbreviations

AEP	Annual Energy Production
BEM	Boundary Element Method
BEMIO	Boundary Element Method Input/Output
BIE	Boundary Integral Equation
CAPEX	Capital Expenditure
CF	Capacity Factor
CFDD	Cumulative Freezing Degree Days
LCOE	Levelised Cost of Energy
OPEX	Operational Expenditure
OWC	Oscillating Water Column
PTO	Power Take-Off
RAO	Response Amplitude Operator
SIC	Sea Ice Concentration
SIT	Sea Ice Thickness
TRL	Technology Readiness Level
WEC	Wave Energy Converter
WESA	Wave Energy Sustainable Archipelago

List of Symbols

ω	Wave Frequency
\vec{V}	Velocity Vector of Fluid Particle
ϕ	Velocity Potential
ρ	Water Density
$\sigma(\vec{x}_s)$	Source Strength
σ_f	Flexural Strength of Ice
ξ	Device Displacement
$G(\vec{x}, \vec{x}_s)$	Greens Function

p	Annual Probability of Exceedance
A	Added Mass Coefficient
B	Radiation Damping Coefficient
B_{PTO}	PTO Damping
C	Hydrostatic Coefficient
c_g	Group Velocity
C_{PTO}	PTO Stiffness
E	Effective Modulus of Elasticity
E	Wave Energy Density
F_{exc}	Wave Excitation Force
F_H	Horizontal Design Ice Action
F_{PTO}	Power Take-Off Force
F_V	Vertical Design Ice Action
g	Gravitational Constant
H	Wave Height
h_{ice}	Ice Thickness
H_s	Significant Wave Height
k	Wave Number
$K_e(t)$	Excitation Impulse Response Function
$K_r(t)$	Radiation Impulse Response Function
M	Mass of System
P	Wave Energy Flux
p	Pressure of Fluid
P_G	Ice Pressure due to Ice Crushing
T_e	Energy Period
T_p	Peak Wave Period

List of Figures

2.1	Motion of a water particle in a wave [6]	4
2.2	Examples of ocean wave spectra for different wind speeds and fetch lengths [11]	6
2.3	Global offshore annual wave power level distribution [IPCC report 2012] [13]	7
2.4	WEC classification by orientation	8
2.5	Overview of WEC classifications [12]	9
2.6	Working principle of a OWC	10
2.7	Single Heaving Buoy with linear generator by Uppsala University [12]	11
2.8	Photo of Pelamis [25]	11
2.9	Model and working principle of the offshore Oyster 1 device [8]	12
2.10	Schematic and working principle of the Wave Dragon WEC [12]	12
2.11	Map of the Baltic Sea	14
2.12	Sea ice cover of the Baltic Sea from ISO 19906 [38]	15
3.1	Manufactured HSST buoy on the left, WEC deployment on the right [36]	17
3.2	Bathymetry of the Baltic Proper and the Åland Sea, WEC study site in red	19
3.3	Bathymetry plot, WEC study site in red	19
4.1	Different forms of landfast and drift ice [42, 43]	22
4.2	Crushing and bending failure modes	25
4.3	Ice action on a two-dimensional sloping structure	26
4.4	Configuration of ice actions on a sloping structure	27
4.5	Sketch of the interaction process with an ice ridge	29
5.1	Basic Element for Continuity Definition	30
5.2	Boundary conditions for potential flow	32
5.3	Diffraction and radiation pattern for a cylindrical point absorber in waves	33
5.4	Six degrees of freedom (6DOF) of motion for a floating body	35
5.5	Overview of the forces acting on the floating body	36
5.6	Schematic of a linear PTO spring damper system	39
6.1	Season 2019-2020, Ice Free Conditions	44
6.2	Season 2006-2007, Mild Ice Conditions	45
6.3	Season 2010-2011, Moderate Ice Conditions	46
6.4	Season 2009-2010, Severe Ice Conditions	47
6.5	Maximum ice extent in the Baltic Sea [39]	48
6.6	Ice thickness distribution	49
6.7	Gumbel fitted plot with the return period for extreme ice thicknesses	50
6.8	Wave scatter diagram of season 2019-2020, Ice Free , number of occurrences = 8438	51
6.9	Wave scatter diagram of season 2019-2020, Ice Free , shown in percentages and the curves represent the wave power density obtained with eq. 6.1	52
6.10	Wave scatter diagram of season 2006-2007, Mild Ice Conditions , number of occurrences = 8414	53
6.11	Wave scatter diagram of season 2006-2007, Mild Ice Conditions , shown in percentages and the curves represent the wave power density obtained with eq. 6.1	53
6.12	Wave scatter diagram of season 2010-2011, Moderate Ice Conditions , number of occurrences = 8414	54
6.13	Wave scatter diagram of season 2010-2011, Moderate Ice Conditions shown in percentages and the curves represent the wave power density obtained with eq. 6.1	54
6.14	Wave scatter diagram of season 2009-2010, Severe Ice Conditions , number of occurrences = 8414	55

6.15	Wave scatter diagram of season 2009-2010, Severe Ice Conditions , shown in percentages and the curves represent the wave power density obtained with eq. 6.1	55
6.16	Wave scatter diagram September 2006 - September 2021, number of occurrences = 131520	56
6.17	Wave scatter diagram September 2006 - September 2021, shown in percentages and the curves represent the wave power density obtained with eq. 6.1	56
6.18	Extraction of extreme values over a 15 year period using the 'Block Maxima' method	57
6.19	Return value plot of extreme wave heights at given return periods	58
6.20	QQ plots of the significant wave height and the peak wave period	59
6.21	Environmental contour for a 50-year sea state	60
7.1	Flowchart of the numerical processes	61
7.2	Illustration of forces acting on the floating body assuming still water	62
7.3	Geometry of WEC meshed in BEMRosetta	63
7.4	Mesh of 312 panels showing normals from its respective collocation point	65
7.5	Flowchart of the Capytaine processes	65
7.6	Block diagram of the simulink model (Left) and a schematic representation of the WEC system (Right)	66
7.7	Internal mechanics of the PTO	66
7.8	Active power output in kW for the most common occurring sea state $H_s = 0.5m$ and $T_p = 4s$ giving a mean active power of 0.75 kW. It uses a simulation time of 30 minutes.	67
7.9	Convergence analysis for added mass coefficient in heave	68
7.10	Convergence analysis for radiation damping coefficient in heave	69
7.11	Convergence analysis for RAOs in heave	69
7.12	Added mass and radiation damping coefficient comparison for Nemoh and Capytaine	70
7.13	Excitation magnitude and phase comparison for Nemoh and Capytaine	71
7.14	Excitation force magnitude and phase comparison for Nemoh and Capytaine	72
7.15	Excitation force and radiation damping impulse response functions comparison for Nemoh and Capytaine	73
7.16	Response amplitude operator comparison for Nemoh and Capytaine	74
8.1	Simulated force and response in irregular waves from design load case 1	76
8.2	Simulated force and response in irregular waves from design load case 2	77
8.3	Simulated force and response in irregular waves from design load case 3	77
8.4	Design ice action forces plotted against extreme ice thickness	79
8.5	Flowchart for the mean annual energy production	80
8.6	Three WEC configurations with changed translators	81
8.7	Heave RAOs for the three WEC configurations, the vertical lines depict their natural frequencies	82
8.8	Power matrices for different PTO dampings (1st configuration: 17.1kW)	84
8.9	Power matrices for different PTO dampings (2nd configuration: 30kW)	85
8.10	Power matrices for different PTO dampings (3rd configuration: 40kW)	86
8.11	Mean annual energy production to its PTO damping and mass configurations	87
8.12	Heave RAOs for the three WEC configurations tuned to a PTO damping of 80 kN s m^{-1}	88
8.13	Power Matrix at optimal damping of 80 kN s m^{-1}	88
8.14	Average of the mean monthly significant wave height and peak period at site for seasons with sea ice presence and ice free seasons	90
8.15	Monthly Mean Power Output for Seasons with Sea Ice, black line = Mean Power and blue line = Sea Ice Concentration (top to bottom: Mild, Moderate, Severe Ice Conditions)	91
8.16	Monthly Mean Power Output Ice Free Season	92
A.1	Observations from project WESA [44]	103
A.2	Local contact forces on HSST buoy [44]	104
A.3	Contact plane $1-\tau$ [44]	104
D.1	Monthly wave scatter diagram season 2019-2020 Ice Free	111
D.2	Monthly wave scatter diagram season 2006-2007 Mild Ice Conditions	112
D.3	Monthly wave scatter diagram season 2010-2011 Moderate Ice Conditions	113
D.4	Monthly wave scatter diagram season 2009-2010 Severe Ice Conditions	114

List of Tables

1.1	List of search terms used in the literature methodology	3
6.1	Characterisation of local ice conditions based on ice thickness data and the Finnish Meteorological Institute [39]	43
6.2	Parameter of ice thickness distribution	48
6.3	Annual maximum ice thickness, ice concentration and number of days with sea ice cover at investigation site	49
6.4	Extreme significant wave heights based on different return periods and their confidence intervals (ci)	58
6.5	H_s and T_p joint distribution parameters	59
6.6	Design sea states based on the 50 year contour	60
7.1	Parameters of mesh geometry	63
7.2	Computational effort for different mesh resolutions	68
8.1	Maximum heave force and response from the simulated design load cases	77
8.2	Parameters used in ice bending calculations [38][46]	78
8.3	List of parameters for the three WEC configurations	81
8.4	Non-zero hydrostatic stiffness parameters for the three WEC configurations	82
8.5	Overall energy production and the capacity factors for the specified cases	92
8.6	Cost breakdown for a point absorber WEC with a direct-driven linear generator	93
8.7	Sensitivity Analysis: Levelised Cost of Energy (LCOE) for different discount rates and cost scenarios ranging from worst to best	94

Part I

Literature Review

Introduction

1.1. Background and Scope

By 2030 the European Commission aims to reduce greenhouse gas emissions by at least 40% or more compared to 1990 and increase the share for renewable energy to at least 32% [1]. Furthermore, the EU commission has set ambitious goals to increase the installed capacity of ocean energy to 40 GW by the year 2050 [2]. There is a gap between global energy demand and carbon reduction promises as the world works toward zero carbon emissions by 2050. Wave energy has great potential for generating electricity for carbon emission reduction, with advantages of higher power intensity and predictability than solar and wind power, as well as being environmentally friendly. However, there are challenges in its implementation such as the low frequency and high amplitude of wave forces, the harsh environments, the presence of sea ice and the survivability of wave energy converters (WEC). The question arises whether it is possible to deploy wave energy converters in areas where sea ice is present and how this will impact the survivability and power production of these devices. This is an important topic as it investigates the feasibility of expanding wave energy conversion to new areas, as well as the possible benefits and challenges it brings.

1.2. Objectives and Motivation

This study aims to investigate wave energy converters in an offshore environment with sea ice in the Baltic Sea. The selection of the Baltic Sea for the research site stems from several factors, including its seasonal ice coverage across multiple regions, its classification as a low-energy sea, and its historical association with previous wave energy projects. The objective of the literature study is to gain a better understanding of the workings of wave energy converters and use the literature to select the best concept and research site. Since there is a large variety of wave energy converter concepts and a lack of design consensus among them it is beneficial to give an overview into some of the most notable concepts. Compared to oceans, only a small percentage of existing literature on studying wave energy focuses on low-energy seas such as the Baltic Sea and even less studies have been done on wave energy converters in ice regions [3]. This thesis attempts to fill the gaps of knowledge in this field of research as the topic can be helpful in advancing existing technology and contribute to the energy transition.

1.3. Literature Review Methodology

In order to identify and review the body of knowledge of studies of wave energy in the Baltic sea as well as the impact of sea ice the Scopus, Elsevier, ScienceDirect and ResearchGate databases were searched. Keywords used to search the database were “wave”, “energy”, “converter”, “device”, “baltic”, “sea ice” whilst using the “AND” boolean operator. A number of articles, books, technical reports that are relevant to the topic have been reviewed and used as background knowledge. Some articles that were relevant to the topic at hand were found using the bibliographies and references of research studies found through the databases.

Search Terms	Search Results	Relevant Documents
"wave energy converter" AND "baltic"	153	15
"wave" AND "energy" AND "converter" AND "baltic"	400	19
"wave energy converter" AND "sea ice"	77	2
"wave energy" AND "sea ice"	145	4

Table 1.1: List of search terms used in the literature methodology

1.4. Thesis Outline

The literature review provides an overview into wave energy, the workings of WECs and the Baltic Sea. Then an introduction into a case study is given which calls for further investigation and forms the basis of this thesis. The research questions and subquestions are given in section 3.3.

Chapter 4 discusses ice features in the Baltic Sea, its effects on wave resource assessment, and a brief overview of common ice failure mechanisms

Chapter 5 gives a summary of linear potential flow theory and the equations of motion for WECs. This theory forms the foundation on which WEC-Sim and Capytaine is built.

Chapter 6 describes how metocean and sea ice data are extracted, analysed and used in calculations. Based on the gathered data wave scatter diagrams are made and an extreme value analysis is performed for the significant wave height, peak period and sea ice thickness.

Chapter 7 provides an overview of WEC-Sim's workflow. The chosen WEC design is analysed and discussed. The boundary element method is described and how this relates to Capytaine's processes. The model is verified through a mesh convergence analysis and comparisons of the hydrodynamic coefficients using NEMOH.

Chapter 8 showcases the results from the numerical modelling and the calculated design ice actions. The power matrices for varying Power Take-Off (PTO) damping and varying translator sizes are given and the seasonal variability of power output is analysed. Using an economical model the levelised cost of energy (LCOE) is also calculated.

Chapter 9 gives the conclusion of this thesis and answers the research questions. Results are summarised and recommendations for future research are given.

Wave Energy and the Baltic Sea

2.1. Current State of Wave Energy Technology

This chapter gives an overview on wave energy harvesting and the current state of the technology. Section 2.1.1 and 2.1.2 briefly discusses the theory and calculations on wave energy. An overview of the benefits and challenges of wave energy as well as classifications are presented in section 2.1.3. Various types of WECs and their working principles are also briefly reviewed. Section 2.1.4 goes over the key performance metrics used to assess and compare different concepts with each other.

2.1.1. Theory on Wave Energy

When the sun radiates on the earth's atmosphere it causes air circulation to occur. Subsequently, this air circulation, also known as the wind, can transfer energy onto the sea surface causing wave propagation. The wavelength and the period depend on the wind speed. A longer duration of the wind blowing and the greater the fetch (surface area where the ocean waves are generated by the wind) the higher the waves will be. Waves can travel over vast distances with only minor losses in energy [4]. If the wind ceases to blow, the waves can still carry energy for some time before stopping as well. This implies that the resource availability of wave energy is larger than wind or solar [5]. Wave energy can be harvested using a wave energy converter (WEC) by the pressure fluctuations below the sea surface or by the oscillating motion of the waves. The purpose of the WEC is to convert the energy of the waves into usable energy.

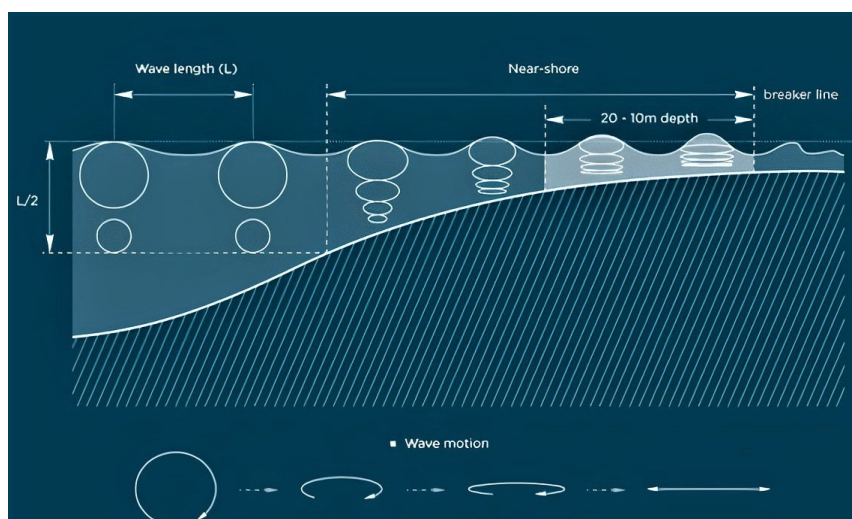


Figure 2.1: Motion of a water particle in a wave [6]

An oscillatory wave in deep water, where the depth is more than half the wavelength, consists of water particles at the surface that move in circles which is called the orbital motion. The radius of this circle is equal to the amplitude of the wave and decreases exponentially with the depth and ceases at depths larger than half the wavelength. Therefore a WEC looking to exploit the pressure fluctuation of waves would not

benefit at greater depths as well and should do so closer to the surface [4]. As the waves propagate in shallow water, where the depth is less than 5% of the wavelength, the motion of the water particles are affected by the interaction with the seabed. Due to this interference, the particle path stretches and flattens to form an elliptical shape. The horizontal movement of the particles remain constant while the vertical movement decreases with the depth and thus flattening the elliptical shape even more [7]. The horizontal movement of the water particles dominates in nearshore coastal zones and thus makes it more attractive for oscillating wave surge converters [8].

Wave energy can be characterised by the wave energy density per unit horizontal area or by the wave energy flux which is the wave power in kW/m of crest length. According to linear wave theory [7], the total average wave energy density is:

$$E = \frac{1}{8} \rho g H^2 \quad (2.1)$$

Where ρ represents the density of the sea water, g is the gravitational constant, and H is the wave height. In reality, however, the waves of a sea state do not all share a constant height and can therefore be characterised with the significant wave height H_s . The significant wave height represents the average wave height of the highest one-third of the waves. It can also be obtained from the wave spectrum for a specific location $H_s = 4\sqrt{m_0}$. The variable m_0 is called the zeroth order moment and is a mathematical parameter characterising the wave spectrum. Using the wave energy density E from the equation above, the wave energy flux P that is aligned with the wave direction can be written in the following form:

$$P = E c_g \quad (2.2)$$

Ocean waves propagate as groups and travel times should therefore be calculated with the group velocity. The c_g in the equation represents the group velocity of the waves which depends on the wavelength and the wave period. The Baltic Sea is relatively shallow [9] and deep water estimations are not always applicable for calculations when analysing the wave energy therefore it is necessary to use the dispersion relationship $\omega = \sqrt{gk \tanh(kd)}$. With $\omega = \frac{2\pi}{T}$ being the radian frequency, k the wavenumber, and d the water depth. The group velocity of the waves can then be written as:

$$c_g = \frac{\omega}{2k} \left(1 + \frac{2kd}{\sinh(2kd)} \right) \quad (2.3)$$

According to [7], when $k \cdot d > 3$ it is assumed to be deep water and when $k \cdot d < 0.3$ it is assumed to be shallow water (and everything in between being intermediate water).

Substitution into 2.2 for wave energy flux becomes:

$$P = \frac{\rho g H_s^2}{16} \left(1 + \frac{2kd}{\sinh(2kd)} \right) \frac{\pi}{k T_e} \quad (2.4)$$

The mean energy period $T_e = \frac{m_{-1}}{m_0}$. The expression above does not take into account that many wave components of natural wave fields propagate in a certain range of directions and could therefore overestimate the actual wave energy resource available for a WEC [9] [10].

2.1.2. Sea State and Ocean Wave Spectra

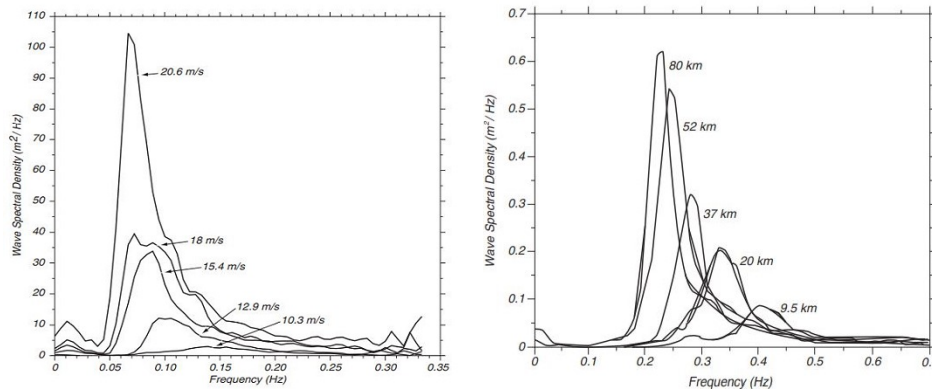


Figure 2.2: Examples of ocean wave spectra for different wind speeds and fetch lengths [11]

The wave spectrum can be a useful tool for predicting the impact of waves on marine structures, assessing the feasibility of wave energy conversion technologies, and for navigation and offshore operations. The parameters of the spectra, such as the significant wave height, wave period, and spectral bandwidth, can be used to characterize the severity and frequency of sea states, and to design offshore structures and vessels that can withstand the forces of the ocean. The JONSWAP and Pierson-Moskowitz spectra are two commonly used models for describing the statistical distribution of wave energy across various frequencies and wave lengths [11].

The Pierson-Moskowitz spectrum is an idealised theoretical model, proposed in 1964, that describes the spectral shape of a fully developed sea state. It is based on the assumption that wind blowing for a long period of time on a large enough sea surface would lead to fully developed ocean waves. The wind would be in equilibrium with the waves. In addition, the spectrum assumes that the waves are in deep water, fully developed, uniform, with wind blowing for a sufficient period. The spectrum predicts the energy distribution of wave heights and frequencies based on the wind speed, duration and fetch. The model is commonly used in wave forecasting and design of marine structures [11].

Almost a decade later, an improved version of the Pierson-Moskowitz spectrum was proposed called the JONSWAP spectrum. This spectrum accounts for real sea states which can differ from the idealised conditions assumed in the Pierson-Moskowitz spectrum. It found that wave spectra are never fully-developed. The JONSWAP spectrum includes an additional parameter, the peak enhancement factor, which accounts for the effects of wave nonlinearities on the spectral shape of waves. It is used to characterize sea states that differ from the fully developed sea state, such as storm-driven waves, shallow water, and coastal regions [11].

2.1.3. Wave Energy Converters

Wave energy converters have been developed and experimented with ever since 1799 when Pierre-Simon Girard patented a concept for a wave-powered device. Since 2015, over a 1000 wave energy concepts have been patented each year worldwide [5]. Nevertheless, developments in wave power are still in the relatively early stages compared to wind and solar energy. The oil crisis in the 1970s further caused rapid development of renewable energy resources and raised interest in wave energy production [12]. In recent years, society has started to realise that there is a significant potential for energy harvesting from the world's oceans. According to a 2012 report on Renewable Energy Sources and Climate Change Mitigation, the total theoretical wave energy potential is estimated to be 32,000 TWh/yr [13]. In 2019, the total global electricity consumption reached 22,848 TWh [14]. This means that the theoretical wave energy potential globally could meet the world's electricity demand. In practice however, this becomes a challenge as wave energy technology has not yet reached its maturity [5].

There are several advantages with wave energy making it a useful addition to the global energy mix. According to Drew et al., one of the benefits when it comes to wave energy is that the energy density of sea waves is the highest of all renewable energy sources [15]. Additionally, wave energy resources have a high availability compared to other renewables such as wind and solar. Up to 90% of the time wave

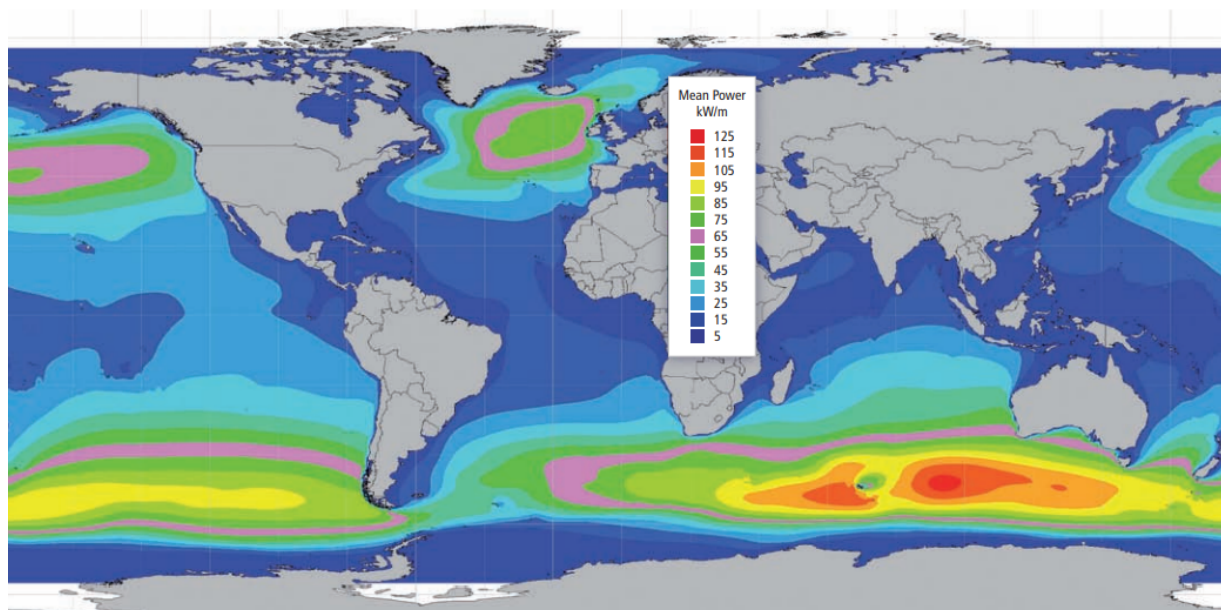


Figure 2.3: Global offshore annual wave power level distribution [IPCC report 2012] [13]

energy is suitable for electricity generation whereas solar and wind can only operate 20-30% of the time [5]. Another benefit is that the natural seasonal variability in wave energy follows the electricity demand. There is little energy loss when waves travel long distances [15]. From an environmental perspective, wave energy has one of the lowest levels of life-cycle greenhouse gas emissions compared to other resources [5].

Some of the major challenges when it comes to wave energy relates to the efficiency of energy conversion, current development status of WECs and the capability to withstand the environmental conditions. Waves are irregular and have a large variability in several time-scales: from wave to wave and month to month [12]. This variability in the waves leads to varying power levels of the WEC. Consequently, this requires a system for storing energy so the power can be converted into smooth electrical output [15]. Furthermore, hurricanes and storms pose extreme loading conditions that affect the performance and survivability of the WEC. Also the corrosiveness of sea water poses a risk to the lifecycle of a WEC. A comprehensive operation and maintenance strategy is required at the design stage, which will add to the lifecycle cost [16]. Moreover, it is important to note that wave energy converters are still in their early stages compared to other mature renewable energy technologies such as wind and solar. Various technologies for capturing wave energy have been considered with over a thousand patents and prototypes, this also means that wave energy technology has not yet converged [16].

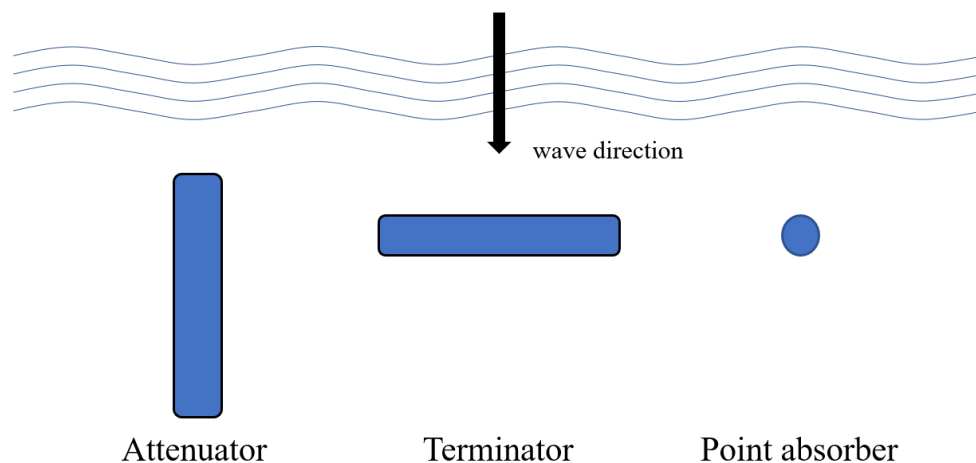


Figure 2.4: WEC classification by orientation

There exists several types of wave energy converters. Different classifications can be made based on operating principle, orientation, PTO and application [17]. WECs can be categorised based on their dimensions and orientation as either a point absorber, attenuator or terminator [17]. The point absorber is omni-directional dependent, meaning that it does not depend on the direction of the wave rays and generates electricity by converting the energy of the heave motion. Point absorbers have relatively small horizontal dimensions in comparison to the wave length. An example of such a WEC is the AquabuOY and Wavestar which is a multiple-point absorber type of WEC. The attenuator wave energy converters are oriented parallel to the wave rays for it to work effectively. It mostly consists of multiple bodies interacting with each other using joints. One example of this type of WEC is "The Pelamis". Terminators are WECs that extend in the cross-wave direction so that their principal axis is oriented perpendicular to the wave rays. According to a 2014 report from the International Renewable Energy Agency a trend in WEC developments shows that 53% are point absorbers, 33% are terminators, and 14% are attenuators [17].

WECs can be designed to suit different wave conditions and locations. Some are optimized for use in shallower waters, while others are designed for use in deeper water. WEC structural and operational features may differ based on the intended site and the sorts of waves that exist in that area. Wave energy converters are categorized in a variety of ways to reflect the diversity of current WEC technology. To make it simpler, this study classifies WECs primarily based on their operational concept. The main types of WECs can be categorised into oscillating water column, oscillating bodies, and overtopping devices.

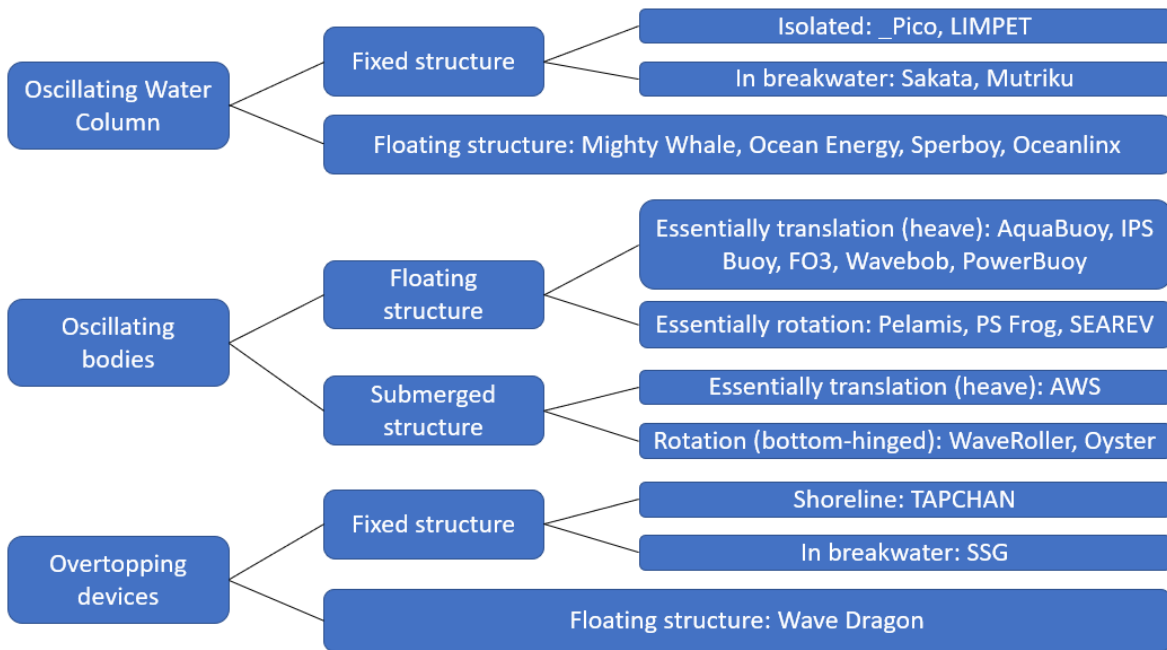


Figure 2.5: Overview of WEC classifications [12]

The Oscillating Water Column

The oscillating water column (OWC) consists of a submerged structure with an opening below the sea surface level allowing air to be trapped inside a chamber. The incident waves in the structure cause fluctuations in the air pressure and a reciprocating air flow that can be used to power the power take off system. The power take off system used to convert power in OWCs are air turbines. The most commonly used air turbine in OWCs is the Wells turbine. The Wells turbine is an axial flow self-rectifying turbine. The reason for this is that the rotor blade airfoil geometry from the two acting surfaces are shaped symmetrical enabling the rotational direction to remain unchanged regardless of the direction of airflow. Another type of turbine is the self-rectifying impulse turbine. This turbine uses two rows of identical guide vanes mirrored on the opposite sides of the rotor. These fixed vanes on the turbine guide the air flow in a manner that drives the rotor blades and achieves self-rectifying behaviour [18]. The rotor blade has the same inlet and outlet angle as can be seen in the schematic representation below.

There are two different types of OWCs namely fixed and floating. Most fixed OWC are installed nearshore where the water depth is not an issue, no deep water mooring and no deep sea cabling is required deep. It is also easier to install and maintain shoreline OWC plants. In addition, some OWC are installed into a breakwater such as the Mutriku plant at the coast of northern Spain [19]. This is useful since integrating such a device into a breakwater system makes it multi-purpose. The breakwater provides protection against coastal erosion as well as tides, currents, storm surges while the OWC is able to generate electricity. This helps divide the construction costs and makes it more accessible for construction, operation and maintenance.

One of the first floating deployed OWC was developed by Yoshio Masuda, a Japanese naval commander. Masuda developed the concept of a floating backwards bent duct buoy which consists of an L-shaped duct that captures energy from the heave, surge and pitch motion of the waves [20]. The name backwards bent refers to the duct backwards facing the incident wave direction. Masuda's concept of a floating backward bent duct buoy was studied and later commercialised and integrated to power navigation buoys. Another floating OWC concept is the Mighty Whale that is deployed near Gokasho bay in Japan. This is a large floating structure that consists of buoyancy tanks and three air chambers equipped with Wells turbines capable of generating a total rated power of 110 kW [18].

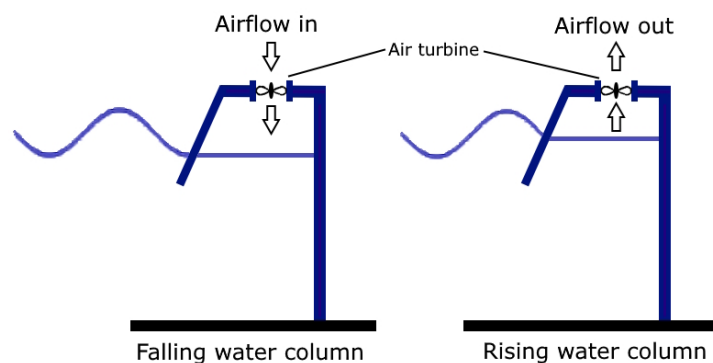


Figure 2.6: Working principle of a OWC

Oscillating Bodies

Oscillating bodies (OB) refer to WECs moving with the motion of the waves. This motion can be either a translational such as surge and heave or a rotational such as pitch [16]. Compared to other types of WECs, they exploit the more powerful wave regimes [12]. One of the main challenges when it comes to oscillating bodies is accessibility for maintenance, mooring and installation of underwater electrical cables [21]. OBs can also be classified in different categories such as single heaving buoys, two-body heaving systems, fully submerged heaving systems, pitching devices, bottom hinged systems or a multi body OB system. A single heaving buoy is an oscillating body device that reacts against the sea bottom or a bottom-fixed structure. Such systems are commonly known as point absorbers where the horizontal dimensions of the device are much smaller than the wavelength. Point absorbers are floating devices that are designed to capture the energy of waves in all directions. It consists of a buoyant structure that is attached to a mooring system, which keeps the device in place while allowing it to move up and down with the waves. The heaving motion of the buoy drives a power take-off system that drives a generator, which converts the mechanical energy into electrical energy. Usually, these are deployed further offshore at considerable water depths where the waves are more powerful.

Sometimes there can be difficulties due to the long distance from the buoy to the fixed frame of reference combined with changing tides. As an alternative, two-body systems can be used. A two body system relies on the relative motion between the two bodies and this motion is used to power a piston or linear generator. This is the case of the Powerbuoy, a floating WEC developed by Ocean Power Technology in the USA. A floating disc shaped buoy oscillates with the motions of the waves and reacts against the inertia of the second body, a submerged cylindrical body [21]. At the bottom of this cylindrical body is a damper plate that increases the inertia through the added mass of the surrounding water [12]. Electrical energy is generated by a hydraulic motor driven by this relative motion [21]. Another notable example of this is AquaEnergy's AquabuOY. The AquabuOY consists of a floater connected to a piston centred in a cylindrical tube. The natural frequencies of the piston and the buoy are different by design that cause significant relative motions between the two. Through the piston cylinder assembly, water is being pumped and used to drive a Pelton turbine as the float oscillates with the waves [22].

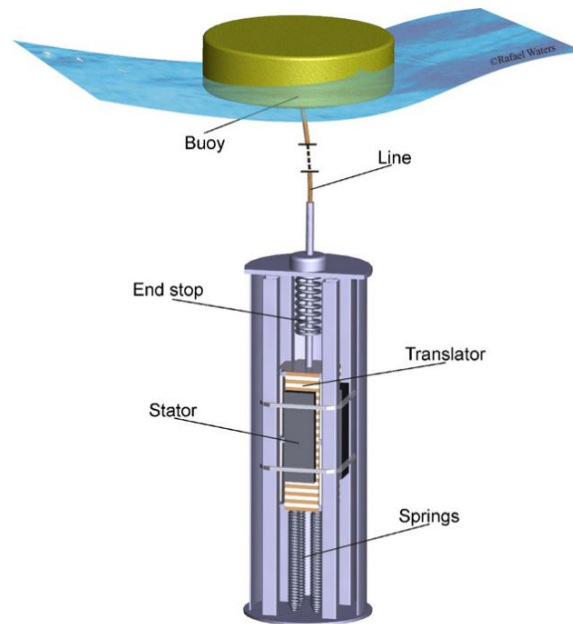


Figure 2.7: Single Heaving Buoy with linear generator by Uppsala University [12]

Then there are WEC systems using multiple bodies. An example of this is the WaveStar developed in Denmark. Floats are connected via arms to a bottom-founded platform. The heave motion of the floats caused by the waves travel via hydraulics to an electrical generator on the platform [23]. Another example of this is The Pelamis, an attenuator type WEC developed in the UK which looks like a steel snake. It has four cylindrical bodies attached using hinge joints. The power take off system is driven by the relative pitch and yaw motion in the joints caused by the waves. The joints drive hydraulic motors which in turn drives the electrical generators. In 2008, the first grid-connected wave farm in the world was installed utilising three Pelamis devices [12]. The survival mode for the Pelamis is $H_s = 8\text{m}$ and for Wave Star up to $H_s = 6\text{m}$ [24].



Figure 2.8: Photo of Pelamis [25]

The Archimedes Wave Swing (AWS) is a fully submerged heaving system that was deployed off the coast of Portugal in 2004. It consists of a bottom fixed part and an oscillating air-filled upper part that is fully submerged. The waves create a pressure differential above the device causing the motion of the upper part to oscillate. The upper part moves down under a wave crest and moves back up under a wave trough. This linear motion is converted into rotary motion which is then converted to electrical energy using a conventional generator. The device also uses a control system to optimise its performance. This control system can adjust the buoy's position, and the angle of the drive shaft to the waves to maximise the power output, and also reduce the structural loads during extreme wave conditions [26]. It is reported that the AWS has a survival limit of $H_s = 6.5\text{m}$ [24].



Figure 2.9: Model and working principle of the offshore Oyster 1 device [8]

Bottom-hinged oscillating wave surge converters are based on the concept of an inverted pendulum. These WECs consist of a buoyant oscillating flap that is hinged to the sea floor. It is installed using the terminator configuration meaning that it is oriented perpendicular to the dominant wave direction. Typically, these devices are deployed near-shore and in shallow waters. Two examples of this type of WEC are the Aquamarine Power Oyster and WaveRoller, from AW Energy. The Oyster is a surface piercing WEC meaning that the flap fully penetrates the water column while the WaveRoller's flap remains fully submerged. Both devices use different PTO systems as well. The Oyster uses a Pelton turbine located onshore while the WaveRoller uses an on board generator connected to a hydraulic motor [12].

Overtopping Devices

An overtopping device uses the wave crests to overspill into a reservoir where water is stored at a higher elevation than the free surface. This potential energy can be converted into electricity by releasing the stored water back into the sea through a conventional low-head turbine. These devices can be fixed to the shoreline or integrated into a breakwater or even floating offshore in some cases where the waves are generally more powerful [12].

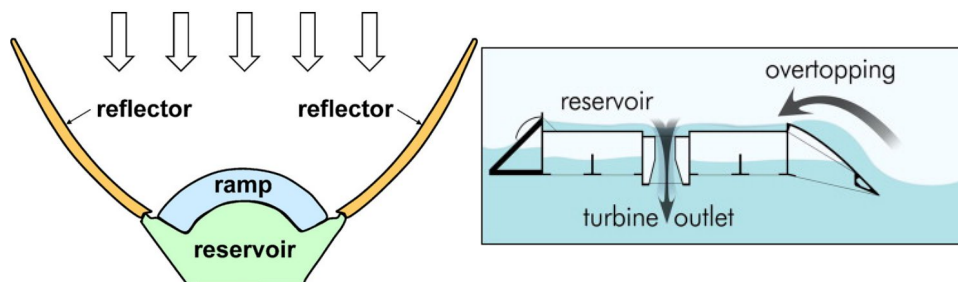


Figure 2.10: Schematic and working principle of the Wave Dragon WEC [12]

One example of such a WEC is the Tapchan which uses a collector to concentrate the incoming waves before entering the reservoir. The waves enter the wide end of the channel and as they approach the reservoir the channel gets increasingly narrower and the waves increase in height. At a certain wave height the top of the waves go over the edge of the vertical walls and spill into the reservoir where water is filled. With enough water the reservoir can provide a stable water flow to the turbine. An example of a floating offshore overtopping device is the Wave Dragon, an overtopping device developed in Denmark. Here the incident waves approach a sloping wall or ramp. The same principle applies as the previous example but instead two reflectors are used to concentrate the incoming waves towards the ramp [12].

2.1.4. Performance Metrics

Technology Readiness Level

The Technology Readiness Level (TRL) is an indicator used to assess the developmental maturity of a technology on a scale from 1-9. A TRL of 1-3 is used to describe the research phase of a new technology, levels 4-6 represent the development phase and levels 7-9 represents the deployment and testing phase. The highest level TRL of 9 means that the technology has undergone testing multiple times and is commercially available. In terms of renewable energies, wind and solar power technologies have reached a TRL 9, meaning that they are widely used in commercial and grid-connected deployments. Wave energy converters, on the other hand, are primarily in the development phase at TRLs 5, 6, and 7, with many other conceptual designs at even lower TRLs. There are many reasons for this, such as the large range of wave energy technologies proposed and the absence of infrastructure and processes for planning and licensing marine activities. In addition, unwillingness to allocate research investment into a new, competing technology is in part because wind and solar power are already proven technologies deployed in commercial, grid-connected applications. In recent years, there is an increased interest in wave energy converters as more wave energy devices have been constructed and governmental support for the technology has increased. To achieve maturity in the industry, all of these efforts are necessary for advancing technology along the TRL scale. According to JRC ocean energy status report 2016, the most advanced WEC devices are the oscillating water column and point absorbers, some of these devices having been tested with an TRL of 8. The rotating mass and oscillating wave surge converters are relatively high and expected to follow.

Annual Energy Production

In order to assess a wave energy project's technological and economic feasibility, the annual energy production (**AEP**) is an essential power performance metric. The scatter diagram represents the probability of occurrence of each sea state in a particular wave climate. The **AEP** can be calculated using the following equation taken from D. Ning et al. (2022) [5]:

$$AEP[Wh] = \frac{8760[h/year]}{100[\%]} \sum_{H_s, T_p} (Powermatrix[W] \times Scatterdiagram[\%]) \quad (2.5)$$

Levelised Cost of Energy

The Levelised Cost of Energy (**LCOE**) is an important measure used to assess the economic feasibility of a technology and is defined by the total costs over its lifetime divided by total energy produced over its lifetime. According to the EU Strategic Energy Technology Plan, the **LCOE** of wave energy is expected to decrease to 0.15 EUR/kWh by 2030 and 0.10 EUR/kWh by 2035 [27].

$$LCOE = \frac{CAPEX + \sum_{t=1}^n \frac{OPEX}{(1+r)^t}}{\sum_{t=1}^n \frac{AEP_t}{(1+r)^t}} \quad (2.6)$$

The capital expenditure (**CapEx**) signifies the total capital costs of the wave energy device, this includes the costs of manufacturing and installation of the device itself but also the costs associated with the development, project management, power cabling and moorings. The operational expenditure (**OpEx**) are all costs related to the operation and maintenance of the system in the year t , as well as insurance for all equipment and renting the seabed at the chosen deployment site. Parameter r is the discount rate and n is the expected lifetime of the system in years. The **AEP** is an estimate of the energy produced by the wave energy converter over a one year period. In order to make calculations on the **LCOE**, specific information about the location and type of device are necessary. Factors such as the size and design of the device and the specific location where it is deployed can also affect the **LCOE** [28].

2.2. Baltic Sea and its Characteristics

2.2.1. Metocean Conditions

The Baltic Sea is the world's largest brackish water sea with a surface area of more than 393,000 km². The sea is bounded by Finland, Sweden, Estonia, Latvia, Lithuania, Poland, Germany and Russia and ranges from 53°N to 66°N in latitude and 10°E to 30°E in longitude. It is considered to be relatively shallow with a mean depth of 54 m and a maximum depth of 459 m at the Landsort Deep, which is situated in the western Gotland Basin off the Swedish coast [29, 30]. The Baltic Sea can be divided into different regions depending on the sea bottom form. These regions include the Gulf of Bothnia Sea and the Bay of Bothnia to the north, the central Baltic Proper, the Gulf of Riga and the Gulf of Finland to the east and the Bay of Gdańsk to the south [31]. The sounds between Sweden and Denmark are the only connection to more open seas [32].

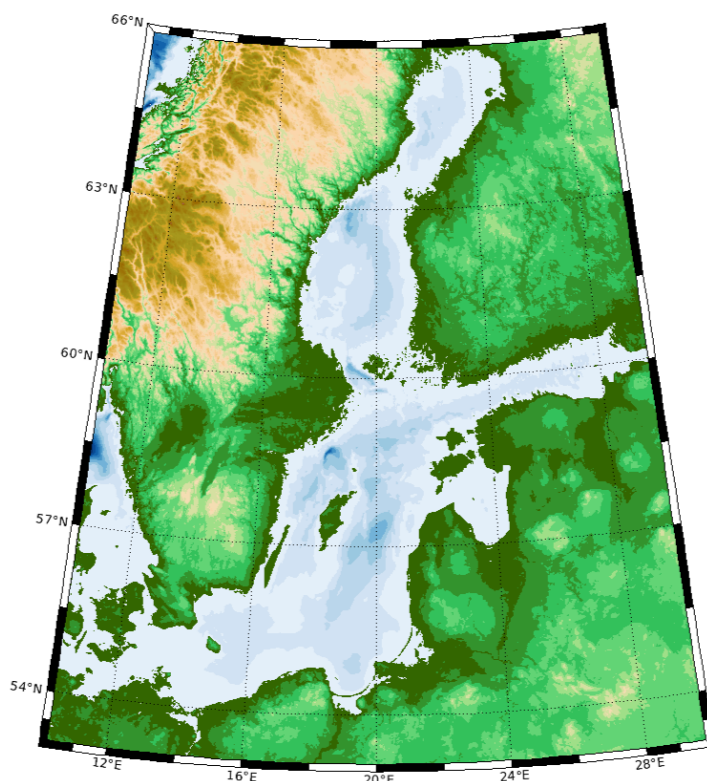


Figure 2.11: Map of the Baltic Sea

2.2.2. Hydrography

Water exchange to the Baltic Sea and North Sea is limited due to the shallow and narrow straits connecting the two water bodies. Saline water from the North Sea enters through the southwestern strait into the Baltic Sea. At the opposite end, a large supply of freshwater is concentrated in the northeastern area of the sea and in the large gulfs [33]. The flow resembles a two-layer flow system in which fresh water in the surface layer flows out of the Baltic and denser saline water enters near the bottom [30]. In the Baltic Sea there are four mechanisms that induce currents: wind stress at the sea surface, sea surface tilt, thermohaline horizontal gradients of density and tidal forces. Additionally, the coriolis-acceleration, topography and friction play a role in the steering of the currents. It is found that the long-term mean surface circulation is anticlockwise in the main Baltic basins [30]. The currents in the Baltic are heavily dependent on the weather conditions and therefore highly variable. The Baltic Sea has no noticeable permanent currents.

The surface currents generated by winds and freshwater drive short term currents with typical speeds of up to 10 cm/s. Deep-water currents on the other hand are driven by the density differences of freshwater and seawater and generally travel at much slower speeds [34]. In general, the salinity of the Baltic Sea increases from east to west and from the north to south. A clear salinity gradient can be seen between the different regions of the Baltic Sea. The Gulf of Bothnia has a measured sea surface salinity of 1-3 ppt in the northern part and 3-6 ppt in the southern part. For the Baltic central a sea surface salinity of 6-8 ppt can be seen and Kattegat 18-30 ppt which has seawater flowing from Skagerrak [32]. The central Baltic Proper has a permanently stratified water column meaning that the less saline cold water is separated from the more saline warm deep water. This varies in the shallow western area where a change between well-mixed and stratification conditions can be seen [33, 30].

2.2.3. Waves

In order to work efficiently, wave energy converters need to be adapted to their local wave climate. This is why knowledge and understanding of the wave climate is of importance. In the Baltic Sea the colder polar easterlies and warmer westerlies create a belt of low pressures known as the Polar Front. As a consequence, a large variation in the wind field can be seen. Seasonal variations with higher wind speeds during winter periods than the summer lead to higher significant wave heights with longer periods for different regions of the Baltic Sea. The largest seasonal variation of the significant wave height and period is found at Gotland Deep with a 0.5 m and 0.5 s difference between the summer and winter seasons [35]. In general, wave heights in the Baltic Sea are larger than those in lakes but smaller than those in the oceans [30]. It is estimated that the Baltic open sea offers a mean power density of 1.3-2.8 kW/m wave front and the annual energy potential to be between 24-56 TWh [36].

2.2.4. Sea Ice

The development of winter shipping has led to many studies relating to sea ice in the Baltic Sea. During normal winters, ice covers 15-50% of the sea area in its northeastern part. Typically, the duration of yearly ice coverage is 5-7 months in the Bothnian Bay, 3-5 months in the Bothnian Sea, 0-4 months in the Archipelago Sea, over 4 months in the Eastern Gulf of Finland and 1-3 months in the Western Gulf of Finland. In the Gotland Sea on the other hand it only lasts less than a month and even then there are parts of open water present. This could extend to the whole sea during exceptionally cold and severe winters [30, 33, 37].

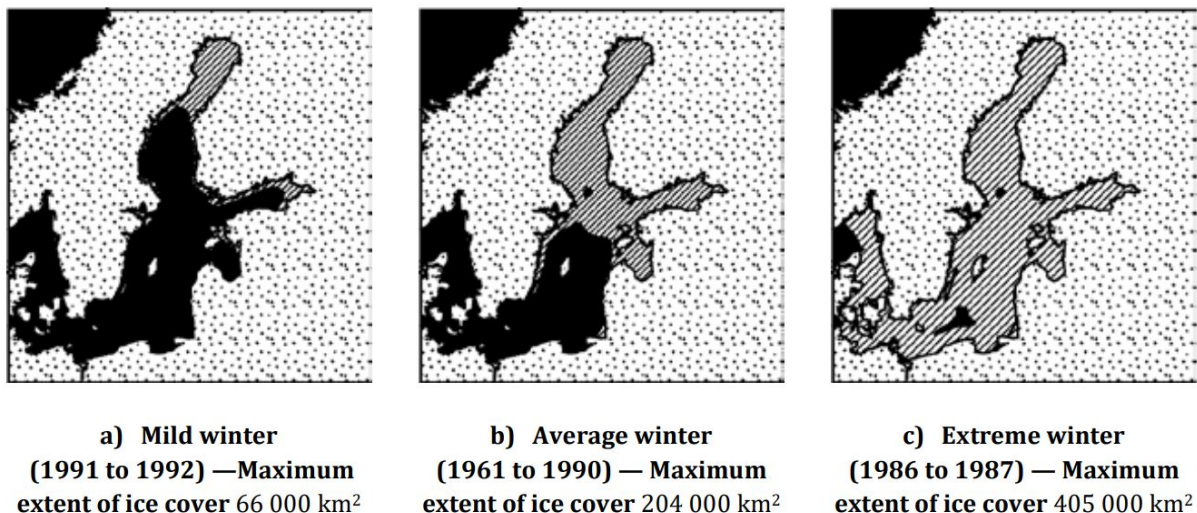


Figure 2.12: Sea ice cover of the Baltic Sea from ISO 19906 [38]

According to a review on ice in the Baltic Sea, sea ice covers a mean of 40% of the Baltic Sea annually with the median maximum ice extent from the years 1971-2000 being 157,000 km² [37]. In recent years 2000-2020 this was 129,000 km² [39]. Ice formation typically starts in the months October-November up

north in the Bothnian Bay and in the eastern parts of the Gulf of Finland. The inner part of the Bothnian Bay is relatively shallow and contains a considerable amount of freshwater, thus having a lower heat content providing good conditions for freezing. Initially, land-fast ice gets formed that is anchored to islands and shoals preventing break-up of thin ice cover by winds or waves. The freezing then extends to the coastal areas around the Bothnian Sea, the Archipelago Sea and the entirety of the gulfs. During a normal winter the central part of the Bothnian Sea as well as the Northern Baltic Proper freeze but during severe and infrequent cold winters, ice coverage may extend southwards towards the Southern Baltic Proper and the Danish Strait [37]. The ice in the Baltic Sea consists mainly of landfast ice and drift ice. Landfast ice forms at shallower depths up to 15 m along coasts and islands and drift ice is dynamic by nature. Drift ice can be categorized as either rafted, ridged or level ice.

Since the northern reaches of the Baltic Sea are frequently covered by sea ice for long periods of the year, wave energy development is limited. Sea ice dampens waves, reducing the effective fetch length and consequently the potential wave energy. In addition, survivability becomes a concern as drifting sea ice might damage WECs. For seasonally ice-covered oceans, specific types of converters are required. The majority of literature on this topic suggests that point absorbers are the optimal wave energy devices for deployment in ice-affected regions [3, 9]. One research project focused on solving and investigating this problem by developing a single heaving-buoy WEC operating and surviving ice interaction [36] as is explained in detail in section 3.1.

Research Proposal

3.1. Case Study: Project WESA

The Wave Energy for a Sustainable Archipelago (WESA) project was initiated with the goal of developing a WEC capable of operating and surviving ice interaction in the Baltic Sea. It's a collaborative effort between Åland Innovation Cluster, the University of Turku, Uppsala University, and Seabased AB. The project led to the creation of a point absorber type WEC manufactured by Seabased AB, which underwent full-scale sea trials during two winter seasons (2011-2013) at the Hammarudda research site, situated 800 meters off the southwest coast of Åland. These trials, documented in [36], tested the WEC using two different buoys, both of which successfully withstood the harsh winter conditions, including encounters with drifting ice fields measuring up to 15 cm in thickness.

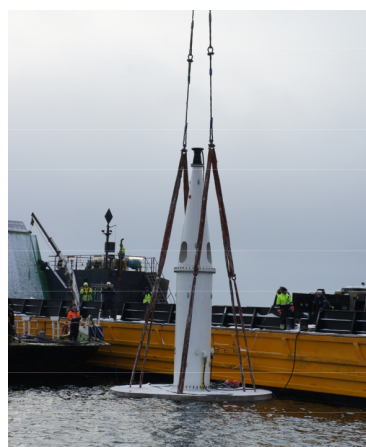


Figure 3.1: Manufactured HSST buoy on the left, WEC deployment on the right [36]

Seabased's WEC is of the point absorber type consisting of a single heaving floating buoy attached to a steel wire driving an encapsulated linear generator that is placed on the seabed. The linear generator uses a direct drive permanent magnet to generate electricity. As the translator moves in a vertical motion within the stator it converts kinetic energy into electric energy. The permanent magnets attached to the translator induce a change in the magnetic flux of the coil windings of the stator and this generates an alternating current. The linear generator is optimised to produce high power even for slow wave motions so no intermediate mechanical gearing is needed. The linear generator has a nominal power rating of 17.1 kW. The capsule serves as a boundary between the generator and the surrounding environment and is pressurised using nitrogen gas that is equal to the average outside seawater pressure. On top of the capsule is the superstructure, a conical shaped structure that absorbs the side forces where the buoy line moves through and transmits the forces to the concrete foundation below. Based on local wave and seabed conditions, the concrete foundation measures around 6 m wide and weighs around 50 tonnes. The seabed does not need to be prepared for this concept [31, 36, 40].

3.2. Site Selection

Determining the precise location is of utmost importance in offshore projects, as it significantly influences the project's success and serves as the fundamental basis for all the following calculations. There are several factors when deciding on a location that needs to be taken into account for the chosen wave energy converter. As outlined in [36] the main contributing factors are listed below:

- Seabed slope
- Seabed sediment composition
- Water depth
- Distance to shore
- Underwater obstacles

The seabed slope is of great importance since the WEC needs to be placed on a suitable flat surface for the concrete foundation of the WEC to be stable. The seabed sediment composition needs to also be taken into account when deciding on a deployment site as it can have an impact on operation during its lifetime. Another factor to consider is the water depth. According to Chatzigiannakou et al. (2019) [41] this should be between 20-100 m which the WEC in chapter 3.1 is designed for. The distance from the WEC to the shore can't be too large either since this leads to higher capital costs, being more difficult to monitor and less accessible for maintenance. The accessibility is shown to be strongly influenced by distance from shore and sea-ice conditions. The sheltered Baltic Sea has very high accessibility as long as infrastructure is designed for significant wave heights of 3 m, while in the northern basins, waiting periods are increased if critical ice-conditions are found [24]. Prior to deployment investigation should be made assessing the site and seeking out any underwater obstacles. This inspection can be undertaken by a remote operated vehicle or by a team of divers. One study evaluated the accessibility to near-shore and offshore marine sites based on wave and ice conditions in the Swedish Exclusive Economic Zone [24]. In the paper, a joint analysis is made of average relative suitability indexes for various aspects that could be used in the site selection process. These aspects include wave power, ice concentration, ice thickness, ice/wind speed, significant wave height, weather window and mean waiting periods. The results identified areas on a chart and compared these based on their relative wave resource classification. It can be a useful tool for finding a suitable location of deployment for wave energy converters. For the WESA project (Wave Energy for a Sustainable Archipelago) in Åland, Finland, the choice of the Hammarudda research site for a full-scale demonstration of a wave energy converter in sea ice was guided by multiple considerations. Firstly, the site's distinguishing characteristics include high waves with a relatively short wave period, which are commonly observed in the Baltic Sea. Secondly, Hammarudda boasts a high likelihood of encountering ice during the winter season, a crucial factor for investigating the interactions between the buoy and ice. Lastly, the site offers convenient accessibility and well-developed infrastructure, which greatly facilitates the execution of the research project. Given these factors, the region surrounding Hammarudda research site emerges as the one of the most logical choices for this study. The final site selection used in this study is shown in figures 3.2 and 3.3 and is located at the coordinates 60°30'00"N 20°00'00"E which is about 6.5 km from the nearest coast line. The site has a higher probability of ice occurrence than the Hammarudda Research Site located along the Southwest coast of the island while also having a substantial wave energy potential. This makes it ideal for studying the influence of sea ice on wave energy and the survivability during ice-structure interactions.

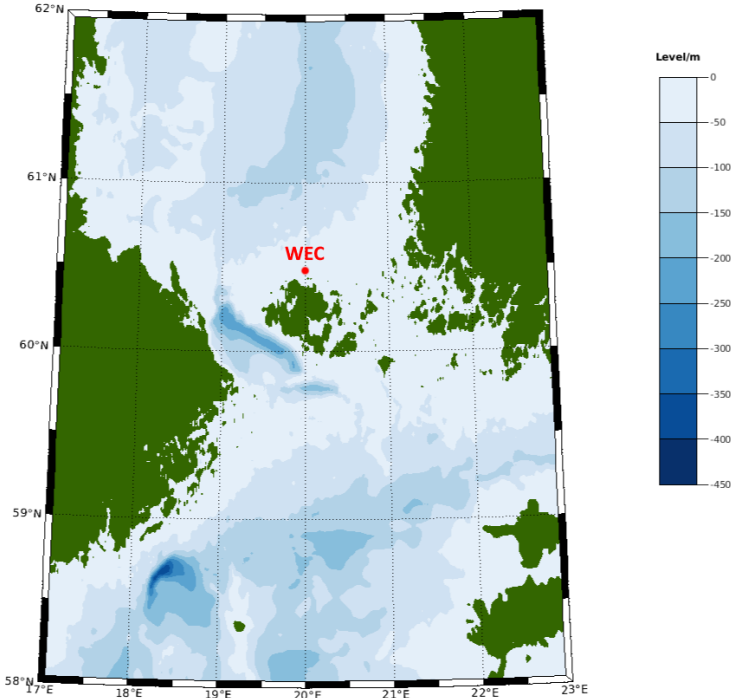


Figure 3.2: Bathymetry of the Baltic Proper and the Åland Sea, WEC study site in red

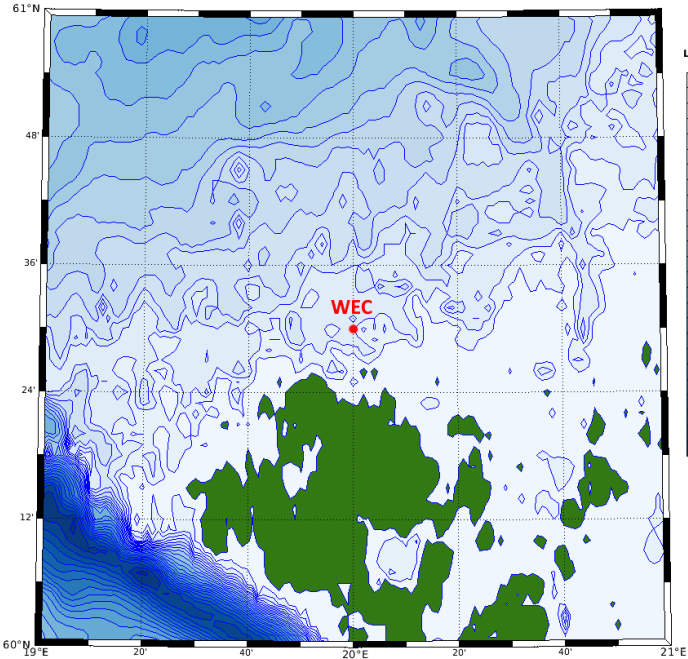


Figure 3.3: Bathymetry plot, WEC study site in red

3.3. Research Questions

As the wave energy project described in section 3.1 already focused on the survivability of a point absorber in sea ice, one could further this research by investigating at how extreme level ice load cases would affect the WEC. In other words, design ice actions on the structure for ice thicknesses with a return period of 50 or 100 years. Another aspect to look into would be to provide a seasonal overview of the days with sea ice coverage for the selected location based on current sea ice data. It would be interesting to see how WEC power output varies throughout the seasons. This leads to the following research and sub-questions:

Research Question 1

How do ice floes and level ice affect the WEC and what are the implications for WEC survivability and energy production during these periods?

- *How do extreme level ice load cases affect the WEC, and what are the survival characteristics of the device under these conditions?*

Research Question 2

What is the seasonal pattern of days with ice coverage, and how does this impact the overall energy output and the economic viability of a WEC investment, taking into consideration the lost energy production due to lack of waves?

- *What are the radiation damping, added mass, and stiffness coefficients of the WEC?*
- *What are the RAOs (Response Amplitude Operators) of the WEC, and how do they impact the WEC's power output under various environmental conditions?*

Part II

Theoretical Background

4

Sea Ice: WEC Survivability and Energy Production

To understand the implications of sea ice on WEC survivability and energy production, chapter 4 explores these aspects specifically within the context of the Baltic Sea. As pointed out in section 3.3, this research investigates the energy production and design ice actions on a point absorber type WEC in the Baltic Sea such as the one shown in section 3.1. The WEC consists of a hexagonal slope shaped buoy that should be capable of surviving ice interactions either by breaking the ice or by diving underneath the unbroken ice sheet. Section 4.1 shows the ice features that can be expected in the Baltic Sea, crucial for engineering considerations. The effects of sea ice on wave energy is explored in section 4.2. Section 4.2 investigates the impact of sea ice on wave energy, while sections 4.3 and 4.4 analyses various ice failure mechanisms and prescribe a design method for ice sheet bending, respectively. Finally, section 4.5 discusses how the buoy would behave when subjected to thicker ice features such as ice ridges and proposes a measure to ensure survivability.

4.1. Ice Features

Sea ice in the Baltic Sea consists mainly of landfast ice and drift ice. Landfast ice is defined as ice that remains attached to a shoreline, island or grounded ice feature. Landfast ice forms at shallower depths up to 15 m along coasts and islands and drift ice is dynamic by nature. Drift ice can be categorized as either rafted, ridged or level ice [38].



Landfast level ice



Rafted ice



Ice ridge

Figure 4.1: Different forms of landfast and drift ice [42, 43]

Different ice features in the Baltic Sea determine the type of ice-structure interaction, the strength and the dynamics of the ice loads. Level ice is defined as a region of ice with a relatively uniform thickness [38]. This thickness can be up to 90 cm in the northern parts of the Gulf of Bothnia. The top layer of level ice is typically granular, followed by the transition zone and columnar grains runs through the bottom layer. Rafted ice is an ice feature formed from the superposition of two or more thin layers of ice. The interaction between thin ice sheets can cause the submersion of one ice sheet beneath the other and are caused by actions from currents, wind and waves. This forces the ice sheets to interact and causes them to override and underide each other, gradually freezing together to form thicker ice than level ice [43]. Thicker ice

sheets under compression or shear forces in ice fields can lead to ridged ice formation, characterised by a build up of rubble along the edges of the interacting ice sheets. Ice ridges consist of ice blocks, water, slush and air. An ice ridge can be divided into a "sail" above the waterplane and a "keel" below the waterplane. The sail mainly consists of ice blocks with air and snow in between. The keel contains submerged rafted ice as well as a consolidated layer consisting of ice blocks and rafted ice frozen together. The upper part of the keel contains the consolidated layer which can grow over time while the lower part contains the unconsolidated layer [38, 43].

The severity of ice and weather conditions for a particular location can be characterised by the accumulated freezing degree days C_{FDD} . This parameter gives the the daily temperatures that are below the freezing point of water summed over the total number of days n_{days} as shown in equation 4.1.

$$C_{FDD} = \left| \sum (T_s - T_{fr}) \right| = |avg(T_s - T_{fr}) \cdot n_{days}| \quad (4.1)$$

where T_s is the mean daily air temperature in $^{\circ}C$ and T_{fr} is the freezing point of water in $^{\circ}C$. The freezing degree days C_{FDD} can be used when determining the thickness of refrozen rafted ice and pressure ridge consolidated ice. According to ISO19906, approximate values for C_{FDD} are given as follows; 4000 for arctic regions, 2000 for subarctic regions and 1000 for temperate ice regions (such as the Baltic Sea). If the exact freezing degree days C_{FDD} of an area during a single winter is known then the total ice thickness for that winter can be calculated using what is known as Stefan's law in equation 4.2:

$$h_{ice} = \sqrt{\frac{2k_{ice}}{\rho_{ice}l}} \sqrt{C_{FDD}} \quad (4.2)$$

where k_{ice} is the thermal conductivity of ice, l is the latent heat of fusion of water and ρ_{ice} is the density of ice. Stefan's law gives a relation between the air temperature and ice thickness.

The mechanical properties of sea ice are necessary for engineering applications. Here, the focus is on flexural failure, given this work involves a slope shaped floater similar to the one used in Project WESA [44]. The flexural strength σ_f is an important property that is used for most design ice action calculations which is a function of the brine volume v_{br} . A smaller brine volume means a smaller porosity of the ice and a stronger ice sheet. The brine volume is generally dependant on the salinity of the ice and the temperature of the ice. According to a study on the flexural strength of sea ice and freshwater ice [45], the brine volume in the Baltic Sea is said to lie between $0.1 < \sqrt{v_{br}} < 0.35$. The flexural strength is assumed to take a value of approximately $\sigma_f = 0.57$ MPa. The flexural strength σ_f and the effective modulus of elasticity of the ice E are calculated using the following equations 4.3 and 4.4 [38, 46].

$$\sigma_f = 1,76 \exp(-5,88 \cdot v_{br}^{0.5}) \quad (4.3)$$

$$E = 5.31 - 0.436 \cdot v_{br}^{0.5} \quad (4.4)$$

4.2. Effects of Sea Ice on Wave Energy

In this research, it is crucial to examine not only the impact of sea ice on offshore structures but also its influence on wave resource assessment, given the focus on wave energy conversion. The effects of sea ice on wave resource assessment are complex and regionally dependent, as shown by two recent studies [10], [47] focusing on different geographical areas. The first study [10] investigated the impact of sea ice on wave energy flux distribution in the Bohai Sea. It explains that the presence of sea ice causes a dampening effect on the waves and reduces the transferred momentum from the air to the ocean surface. The simulations revealed that during extreme winter weather conditions, the presence of sea ice led to significant reductions in wave energy flux, particularly in Liaodong Bay, Bohai Bay, and Laizhou Bay, with reductions of up to 80%, 50%, and 40%-90% respectively. Moreover, even in ice-free areas, the decrease in effective wind fetch due to ice cover in neighbouring bays resulted in large reductions in wave energy flux, showing the importance of considering sea ice effects in wave resource assessment.

Similarly, [47] focused on Alaska's coastline and shows the need to account for seasonal sea ice variability in wave energy assessments as many numerical wave models have overestimated the wave resource of an area by neglecting the presence of sea ice. This study used high-resolution sea ice imagery and demonstrated significant reductions in wave power, particularly during December, along the coastline of Montague Island and the mouth of Prince William Sound. These results indicate a strong seasonal variability in wave power due to sea ice presence. Future research should account for this effect in order to improve the predictions of wave energy flux.

The key takeaways from these studies are listed below:

- Ice cover causes a dampening effect on the waves and can cause a significant reduction in wave energy flux
- Ice free areas experience a reduced effective wind fetch due to neighbouring ice covered areas
- Ice cover reduces the transferred momentum from air to the ocean surface
- The presence of sea ice can cause a strong seasonal variability in wave power
- Sea ice can't be ignored in the deployment locations of WECs

4.3. Ice Failure Mechanisms

In order to determine the ice loads and model the ice-structure interaction it is necessary to identify the ice failure mode. The failure mechanism is determined by variables such as the shape of the structure, the speed and thickness of the ice. The feature used in the ice-structure interaction is considered to be of level ice. Two main mechanisms of failure are crushing and bending, with the latter typically resulting in smaller ice loads. This is because the flexural strength of ice is lower than its compressive strength. Crushing failure is most likely to occur against vertical structures, whereas bending failure occurs against sloped structures. Other mechanisms that can be identified are creep, splitting, spalling and buckling. Bending failure and buckling can be categorised as out-of-plane modes, whereas the other ones are in-plane modes.

4.3.1. Creep

For very low indentation velocities, creep is observed as the main failure mode. As the ice moves slowly against the structure, the ice deforms in a ductile manner, with low stress rates. A uniform pressure distribution can be observed since full contact is made between the ice and the structure. For sea ice, this failure mechanism is quite unusual and short-lived and not likely to be used as a design condition for offshore structures.

4.3.2. Buckling

Buckling is an instability mechanism that typically occurs for very thin ice floes on wide structures, in other words for ice-interactions with a high aspect ratios. Buckling is caused by in-plane forces resulting in out-of-plane deformation. As soon as the stress caused by buckling exceeds the flexural strength of the ice, the ice will fail. This is different from bending failure where out-of-plane forces (due to a sloped structure) cause out-of-plane deformations.

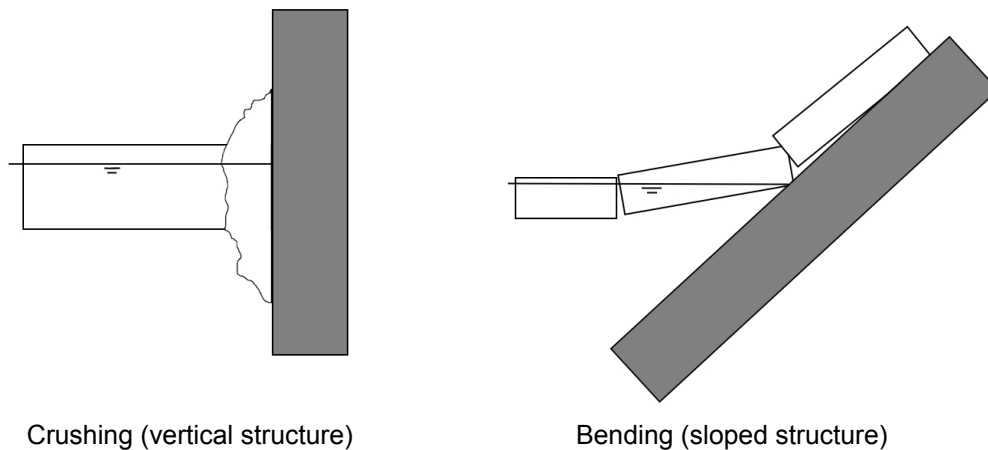


Figure 4.2: Crushing and bending failure modes

4.3.3. Crushing Failure

Crushing failure is a mechanism where cracks propagate in random directions which lead to pulverisation and flaking of the ice. This is usually the case for interactions with high indentation velocities and low aspect ratios (ratio of structure width to ice thickness). The global ice action due to crushing can be expressed through the following equation:

$$F_G = P_G \cdot A_N \quad (4.5)$$

The ice pressure averaged over the nominal contact area is given as P_G and the nominal contact area is given as A_N . The ice pressure term P_G can be calculated using equation 4.6:

$$P_G = C_R \left[\left(\frac{h}{h_1} \right)^n \left(\frac{w}{h} \right)^m + f_{AR} \right] \quad (4.6)$$

where h is the level ice thickness, h_1 is a reference thickness of 1 m, w is the projected width of the structure, n and m are empirical coefficients. The empirical term f_{AR} , can be neglected for aspect ratios $w/h > 5$. The ice strength coefficient C_R (in MPa) has different values depending on the region. According to ISO 19906[38], the C_R for arctic regions is 2.8 MPa, for subarctic regions this is 2.4 MPa, and for temperate areas such as the Baltic Sea this is 1.8 MPa.

4.3.4. Bending Failure

Another way ice can fail is through bending failure. The interaction between a sloped structure and an ice sheet is more likely to fail in bending failure mode although this does not always have to be the case. The ice actions for such a failure mode tends to be significantly lower than in crushing failure mode. There is a lot of research done into ice-interaction on conical structures with either circular waterlines or multi-faceted ones with flat sloping faces. Depending on the slope of the structure it can either break an oncoming ice sheet upwards or downwards. For an upward sloped structure the interaction process can be quite complex with many variables needing to be taken into account. Not only the ice break action needs to be calculated, but also the accumulation of ice rubble on top of the structure will result in additional loads on the structure. The bending of the ice sheet can be modeled similar to an elastic beam. Figure 4.3 shows the contact forces due to level ice acting on a two-dimensional upward breaking sloping structure.

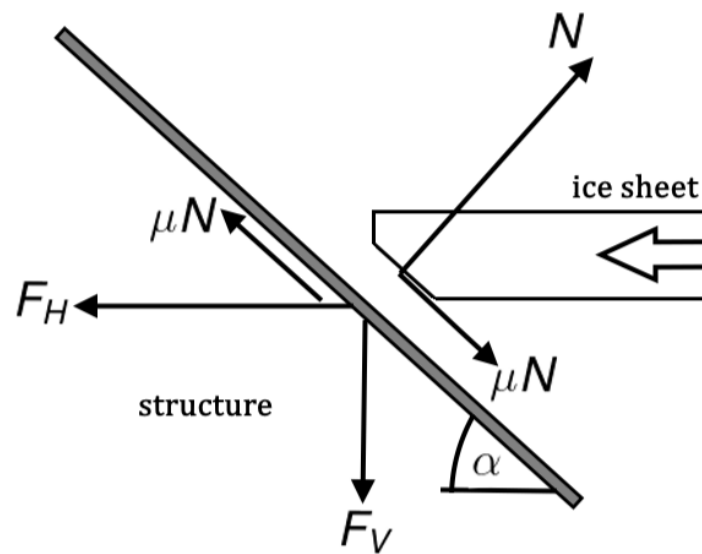


Figure 4.3: Ice action on a two-dimensional sloping structure

- N normal component of reaction to ice action on structure
- μ ice-structure friction coefficient
- α slope of structure face from horizontal
- F_H horizontal component of ice action
- F_V vertical component of ice action

The horizontal and vertical components of ice action can be expressed as:

$$\begin{aligned} F_H &= N \sin \alpha + \mu N \cos \alpha \\ F_V &= N \cos \alpha - \mu N \sin \alpha \end{aligned} \quad (4.7)$$

It then follows that:

$$F_H = \zeta \cdot F_V \quad (4.8)$$

where,

$$\zeta = \frac{\sin \alpha + \mu \cos \alpha}{\cos \alpha - \mu \sin \alpha} \quad (4.9)$$

4.4. Determining Design Ice Actions for Bending Failure

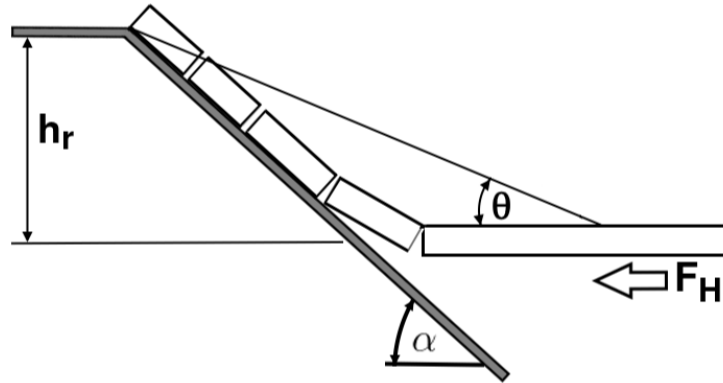


Figure 4.4: Configuration of ice actions on a sloping structure

An ice sheet can be modelled using linear elastic first-order beam theory. For design ice action on sloped structures, the action components are divided into a horizontal and vertical component. The horizontal action component can be calculated using equation 4.10:

$$F_H = (H_B + H_R + H_P + H_L) \cdot I_P \quad (4.10)$$

- H_B is the action to break the ice
- H_R is the action to push the broken ice blocks up the slope
- H_P is the action to push the sheet ice through the ice rubble
- H_L is the action to lift the ice rubble on top of the advancing ice sheet prior to breaking it
- I_P is the correction for the effect of in-plane compression in the ice sheet due to F_H

It is common for upward sloped structures e.g. ice-breaking cones on wind turbines to account for an additional action component that accounts for the turning of an ice block at the top of the slope. Here it is neglected as the ice blocks won't meet a vertical shaft and instead are free to slide over buoy. Timco and Weeks [46] reviewed several studies on ice density measurements of first-year ice and found a wider range from 720 kg m^{-3} to 940 kg m^{-3} with an average of approximately 910 kg m^{-3} . Based on data given in [38], the ice to smooth steel coefficient is assumed to be 0.05 but is likely to increase at lower ice velocities. Additionally, it is recommended to use an ice-ice friction coefficient of $\mu_i = 0.1$ if the exact ice velocity is not known. The selection of the remaining parameters for assessing bending loads relies on sea ice properties outlined in [38], and [46]. In choosing these parameters conservative estimates were selected which are detailed in the following Table 8.2. In order to calculate the load required to break the ice, the effective width for breaking w_B needs to be determined. The width of the structure at the waterline is given as w and R is the distance to the first circumferential crack.

$$w_B = \begin{cases} \left(\frac{\pi^2}{4}\right) L_c, & \text{if } 2R > w \\ w + \left(\frac{\pi^2}{4}\right) L_c, & \text{if } 2R < w \end{cases} \quad (4.11)$$

Where L_c represents the characteristic length of an ice sheet.

$$L_c = \left(\frac{Eh^3}{12\rho_w g(1-v^2)} \right)^{\frac{1}{4}} \quad (4.12)$$

The distance to the first break for a beam depends on the characteristic length L_c .

$$R = \frac{\pi}{4} L_c \quad (4.13)$$

Additionally, the larger vertical forces required to break the ice; V_{B1} for the first break and V_{B2} for the second break need to be calculated:

$$V_{B1} = 0.68\sigma_f w_B (\rho_w g h^5 / E)^{0.25} \quad (4.14)$$

$$V_{B2} = 1,11\sigma_f w h^2 \left(\frac{E h^3}{12\rho_w g (1 - \nu^2)} \right)^{-\frac{1}{4}} \quad (4.15)$$

Once the vertical breaking forces are calculated the horizontal components of ice actions can be calculated. The component required to push the broken ice blocks up the slope through the rubble is given in equation 4.16. The ride-up height is given as h_r and the w_R which is the average of waterline width and the width at the top of the slope.

$$H_R = \frac{w_R h_r \rho_s g}{\cos \alpha - \mu \sin \alpha} \left(\frac{1}{2} (\mu_i + \mu) (1 - e) h_r \cos \alpha \cot \alpha \left(1 - \frac{\tan \theta}{\tan \alpha} \right) + h (1 + \mu \cot \alpha) \right) \quad (4.16)$$

$$H_P = w h_r^2 \mu_i \rho_i g (1 - e) \left(1 - \frac{\tan \theta}{\tan \alpha} \right)^2 \frac{1}{2 \tan \theta} \quad (4.17)$$

$$H_L = w h_r \zeta \left(1 - \frac{\tan \theta}{\tan \alpha} \right) \left(\frac{1}{2} h_r \rho_i g (1 - e) \left(\frac{1}{\tan \theta} - \frac{1}{\tan \alpha} + \tan \phi \left(1 - \frac{\tan \theta}{\tan \alpha} \right) \right) + c \right) \quad (4.18)$$

Similar to equation 4.8, ζ is used to relate the vertical component needed to break the ice to the horizontal component in equation 4.19.

$$H_{B1,2} = \zeta V_{B1,2} \quad (4.19)$$

The compression correction factor can be calculated using equation 4.20.

$$I_{P1} = \left(1 - \frac{H_{B1}}{\sigma_f h \cdot w_B} \right)^{-1} \quad (4.20)$$

$$I_{P2} = \left(1 - \frac{H_{B2}}{\sigma_f h \cdot w} \right)^{-1}$$

$$F_{H1} = (H_{B1} + H_R + H_P + H_L) * I_{P1}$$

$$F_{H2} = (H_{B2} + H_R + H_P + H_L) * I_{P2} \quad (4.21)$$

The total horizontal ice action F_H is given as either F_{H1} or F_{H2} . In order to determine which of the circumferential cracks is governing, both actions need to be calculated and the largest value is selected as the design load. These estimations provide upper bound estimates for the ice action on a sloped structure which is used in this research.

4.5. Buoy-Ice Interaction

The buoy-ice interaction process can be separated into different scenarios which depend on the strength, thickness and form of the ice feature [36]. The first scenario is based on the encounter of thin ice sheets as was shown in the previous section. If sufficient pressure is exerted on the sloped facets of the structure, cracks will start to form in the ice sheet and break. This causes a build up of rubble and ice blocks which will slide over the structure. For encounters with thicker ice sheets, the opposite will happen. When the total downward force on the buoy due to the ice and its own weight exceeds the buoyancy force, the buoy will passively slide in underneath the unbroken ice front as it moves past the structure. During this sliding motion, friction and rough edges on the ice layer will affect its structural integrity which implies the need for a sturdier buoy with a thicker hull. Another scenario to consider is what would happen in the event of encountering an ice ridge. Ice ridges will lead to important design considerations as these often give the largest global forces and can become the determining design load case. For now, what would happen in the case of an encounter with an ice ridge can only be speculated. The following sketch in Figure 4.5 shows what could be expected in the process of an encounter with an ice ridge and the considerations involved.

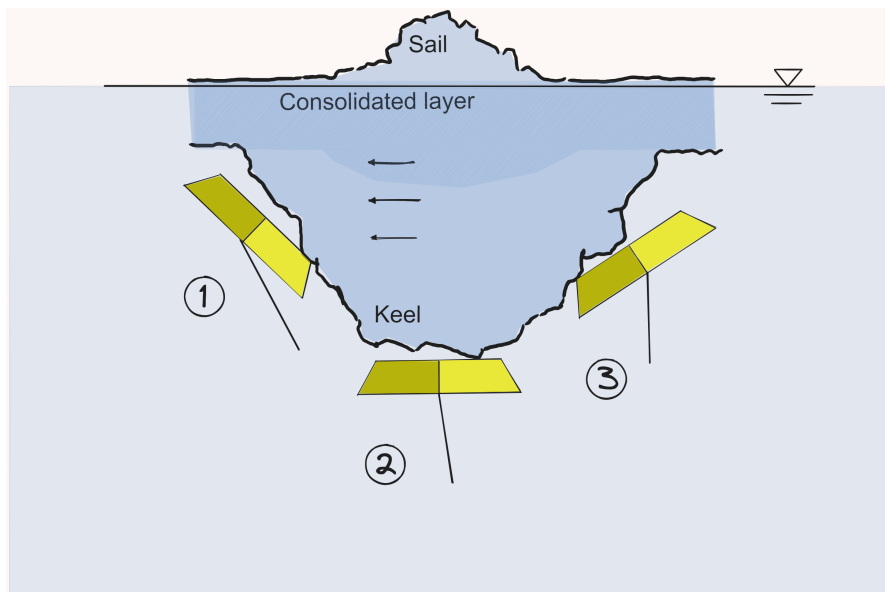


Figure 4.5: Sketch of the interaction process with an ice ridge

1. Initially, the buoy will either already have been submerged due to earlier interactions with thinner ice sheets and get pressed further down under a thicker layer of ice, or it may slide around the ice ridge, depending on the size and shape of it.
2. As the buoy is pressed down to the bottom of the keel, the strain on the buoy line decreases. The buoy begins to slide along the surface of the keel until it reaches the opposite side.
3. Once the buoy reaches the other side of the keel, it begins to ascend again as the ice ridge passes over it. The strain on the buoy line is minimal and this upward movement marks the end of the encounter between the buoy and the ice ridge.

However, it's essential to consider unfavourable scenarios as well. For instance, if the buoy becomes lodged at the point of contact while experiencing tension from the line it would cause an overturning moment that rotates the body potentially resulting in issues with the buoy line. The final anticipated scenario is in the event that the buoy gets entrapped by the ice. This would mean that the ice has completely surrounded or enclosed the buoy preventing it from moving. In this case, the buoy line would be pulled until the translator reaches the upper end stop, where the ice will either break or the force increases until the weakest link of the WEC breaks (typically the buoy line). To save the WEC from damage, Strömstedt et al. [36] proposed using a break load linkage or an automatic release clutch fastened beneath the buoy. This would then detach the buoy when the buoy line force reaches a predetermined maximum. It could then be reattached at a later stage.

Hydrodynamics of WECs

This chapter is dedicated to covering the theory used in boundary element method solvers and time domain modelling of wave energy converters. In order to fully understand the inner workings of software used in this research; Capytaine and WEC-Sim, it is important to understand the physical and mathematical theory behind the simulations. The fundamentals of fluid dynamics are based on potential flow theory which is covered in section 5.1. This theory leads to boundary conditions that can be applied to a floating structure in a fluid. The hydrodynamics of a floating body considers the motions and the forces acting on a body in a fluid. The forces acting on a body can be divided into a diffraction problem due to excitation forces from incoming waves and a radiation problem due to a body's motion in a fluid, described in sections 5.1.3 and 5.1.4 respectively. A full breakdown of the motion equation and its components is explained in section 5.2 and the calculations for power production for wave energy converters are covered in section 5.4. Lastly, in order to deal with non-linear effects and using irregular waves the motion equation can be formulated in the time domain explained in section 5.5.

5.1. Linear Potential Flow Theory

5.1.1. Continuity Condition

In fluid dynamics, describing the complex flow patterns in a fluid domain, especially when dealing with floating objects like ships, typically involves solving the Navier-Stokes equations. However, these equations can be quite challenging to solve. To simplify matters, the continuity condition is used, which ensures that what flows into a control volume must be equal to what flows out, preserving mass.

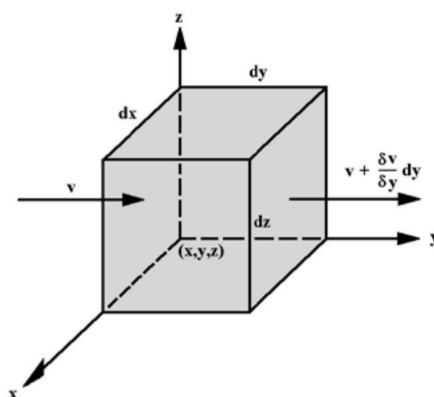


Figure 5.1: Basic Element for Continuity Definition

Figure 5.1 shows that in a fluid element the net mass flow out of the control volume must be equal to the time rate of decrease of mass within the control volume. Thus mass can neither be created nor destroyed. If the fluid is assumed to be incompressible, meaning that the mass and volume remain constant, the Navier-Stokes equation can be simplified to [48]:

$$\nabla \cdot \vec{v} = 0 \quad (5.1)$$

Here \vec{V} represents the velocity vector of the fluid in three dimensions. Equation 5.1 states that the divergence of the velocity vector is zero.

According to linear potential flow theory, used in the boundary element method the following assumptions are made [48]:

- The fluid is inviscid.
- The fluid is incompressible: $\nabla \cdot \vec{V} = 0$
- The flow is irrotational: $\nabla \times \vec{V} = 0$
- The wave amplitude is small with respect to the wavelength.
- The amplitude of the body motion is small with respect to its dimension.
- The sea bottom is flat. The water depth is denoted h .

In this section the concept of a potential function Φ is introduced. Assuming an irrotational and non-viscous flow, the potential function is used to describe the flow. The key property of this function is that its derivatives in different directions correspond to the flow velocities in those directions.

$$\vec{V} = \nabla \phi \quad (5.2)$$

By substituting this potential function into the continuity equation, the Laplace equation is obtained, a second-order partial differential equation that the flow must satisfy. This equation ensures mass continuity; no mass is created or destroyed.

$$\nabla^2 \phi = \frac{\partial^2 \phi}{\partial x^2} + \frac{\partial^2 \phi}{\partial y^2} + \frac{\partial^2 \phi}{\partial z^2} = 0 \quad (5.3)$$

Moreover, in order to calculate forces a floating object experiences in waves one must obtain the pressures in the fluid. From the Navier-Stokes equations one can obtain the Bernoulli equation:

$$p = -\rho \frac{\partial \Phi}{\partial t} - \frac{1}{2} (\nabla \Phi)^2 - \rho g z \quad (5.4)$$

Using this equation it is possible to calculate the forces on objects that are partly submerged in waves. On the right hand side of the equation, the first term represents the first order fluctuating pressure that is induced by the waves. The last term represents the hydrostatic pressure. The second term is a non-linear term and is used when calculating second order wave drift forces. For now, the second order term can be neglected since the flow velocity is relatively small resulting in the linearised Bernoulli equation:

$$p = -\rho \frac{\partial \Phi}{\partial t} - \rho g z \quad (5.5)$$

It's essential to remember that the potential function (denoted as Φ) is not a vector but a scalar function, a single value that varies in space and time. To apply this theory practically, it is necessary to find the specific Φ function for a given flow situation. For linear problems, the solution can be found in the frequency domain.

$$\Phi = \text{Re} \left\{ \hat{\Phi} e^{i\omega t} \right\} \quad (5.6)$$

The conventions of Capytaine are mostly the same as those of Nemoh, where a complex-valued amplitude (phasor) is defined in equation 5.6 above. For regular waves, the potential function can be determined by solving the Laplace equation with appropriate boundary conditions. These boundary conditions ensure that water cannot penetrate the seabed and the hull of the floating body and that fluid particles remain at the free surface [48].

- **Linearised free surface boundary condition.** When a fluid particle is on the free surface, it will remain there.

$$g \frac{\partial \hat{\Phi}}{\partial z} - \omega^2 \hat{\Phi} = 0, \quad \text{on } z = 0 \quad (5.7)$$

- **Impermeable condition on the (flat) sea bottom**

$$\frac{\partial \hat{\Phi}}{\partial z} = 0, \quad \text{on } z = -h \quad (5.8)$$

- **Impermeable condition on the body surface S_b .** The velocity of the flow in the direction normal to the hull must be equal to the velocity of the hull itself in that direction.

$$\frac{\partial \hat{\Phi}}{\partial n} = \hat{V}_n, \quad \text{at } S_b \quad (5.9)$$

- **The radiation wave condition.** Far away from the floating body no disturbances are felt due to the body's presence. R is the radial distance from the body.

$$\lim_{R \rightarrow \infty} \hat{\Phi} = 0 \quad (5.10)$$

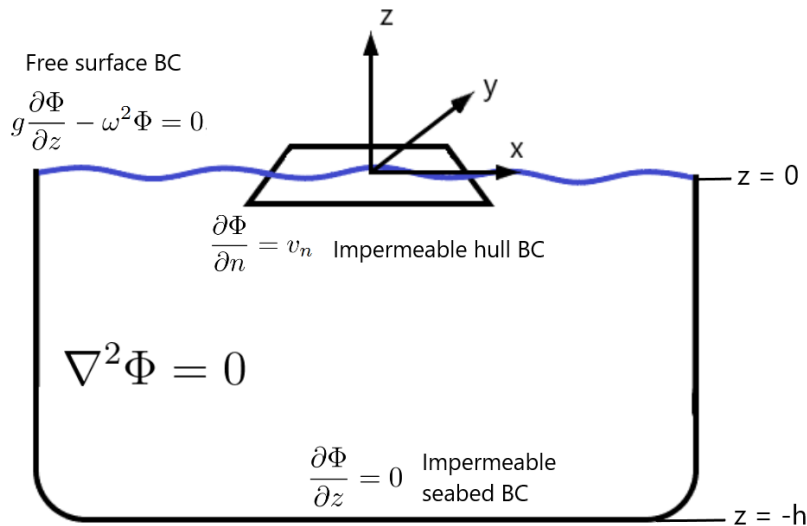


Figure 5.2: Boundary conditions for potential flow

To simplify a complex fluid flow problem the continuity equation is used and the potential function is introduced to describe the flow. This potential function relates flow velocities to derivatives and results in the Laplace equation, which maintains mass continuity. For specific scenarios like regular waves, boundary conditions help determine the potential function.

5.1.2. Velocity Potential Components

The total velocity potential can be split into three components [48]:

$$\Phi = \Phi_R + \Phi_I + \Phi_D \quad (5.11)$$

Φ_R = Radiation potential from the oscillatory motion of the body in still water

Φ_I = Incident undisturbed wave potential

Φ_D = Diffraction potential caused by the scattering of waves

The radiation potential comes as a result radiated waves caused by the motion of the floating body and needs to satisfy the boundary conditions. The incident wave potential and the diffraction potential are caused by the incident wave field and the scattering of waves. Since the incident wave potential represents an incoming wave field without the body, it does not need to satisfy either the radiation condition or boundary condition on the body. In order to solve these potentials the boundary element method defines two problems: the Radiation problem and the Diffraction problem. The normal velocity on the floating body surface serves as the input to these problems.

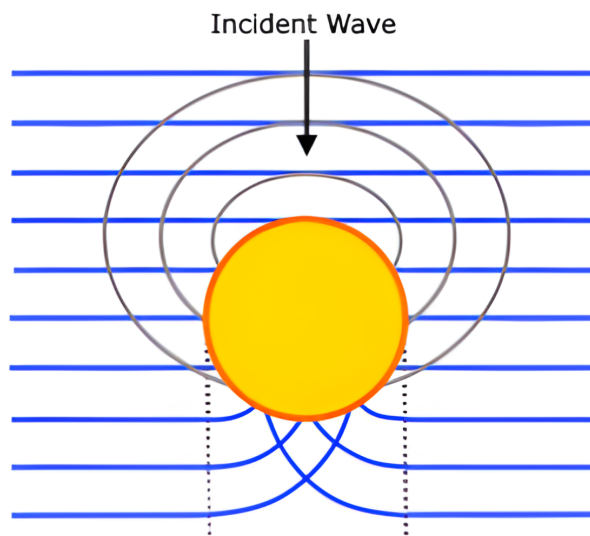


Figure 5.3: Diffraction and radiation pattern for a cylindrical point absorber in waves

5.1.3. Diffraction Problem

For the diffraction problem, it is assumed that the body is kept stationary. The diffracted waves are caused by the interaction of the incident wave field and the motionless body. Solving for this problem, one can compute the excitation forces at different frequencies namely; the Froude-Krylov force and the diffraction force. The Froude-Krylov force is calculated using the incident wave potential while the diffraction force is calculated using the diffraction potential.

According to Airy wave theory [48] an incoming wave field can be described by the incident undisturbed wave potential Φ_I as:

$$\hat{\Phi}_I = -i \frac{g}{\omega} \frac{\cosh(k_0(z+h))}{\cosh(k_0 h)} e^{ik_0(x \cos \beta + y \sin \beta)}, \quad \text{in finite depth} \quad (5.12)$$

where

k_0 = wave number defined by the dispersion relation $\omega^2 = k_0 g \tanh(k_0 h)$

β = wave direction

h = water depth

For deep water the incident potential can be simplified to:

$$\hat{\Phi}_I = -i \frac{g}{\omega} e^{kz} e^{ik(x \cos \beta + y \sin \beta)}, \quad \text{in infinite depth} \quad (5.13)$$

where k represents the wave number based on deep water approximations for the dispersion relation $\omega^2 = kg$. The velocity potential of the scattered wave as a result from the incident wave must respect the boundary conditions on the body, seabed and the free surface.

$$\frac{\partial \hat{\Phi}_D}{\partial n} = - \frac{\partial \hat{\Phi}_I}{\partial n} \quad (5.14)$$

5.1.4. Radiation Problem

In reality, the body is not fixed and thus the presence of the body's motion causes disturbances in the wave field. The radiation potential accounts for a moving body in the absence of an incident wave field and is assumed to oscillate in a harmonic motion [48]. The radiation potential is expressed as:

$$\hat{\Phi}_R = i\omega \sum_{j=1}^6 \hat{\xi}_j \Phi_j, \quad j = 1, 2, \dots, 6 \quad (5.15)$$

The radiation potential consists of six radiation components Φ_j , one for each rigid-body degree of freedom j . The $\hat{\xi}_j$ represents the complex amplitudes of the oscillating motions in its six degrees of freedom. Solving for the radiation problem gives the added mass coefficient and the radiation damping coefficient.

5.2. Equation of Motion for a WEC

An oscillating body at sea can move in 6 degrees of freedom with 3 translational motions and 3 rotational motions; surge, sway, heave, roll, pitch, yaw as depicted in figure 5.4.

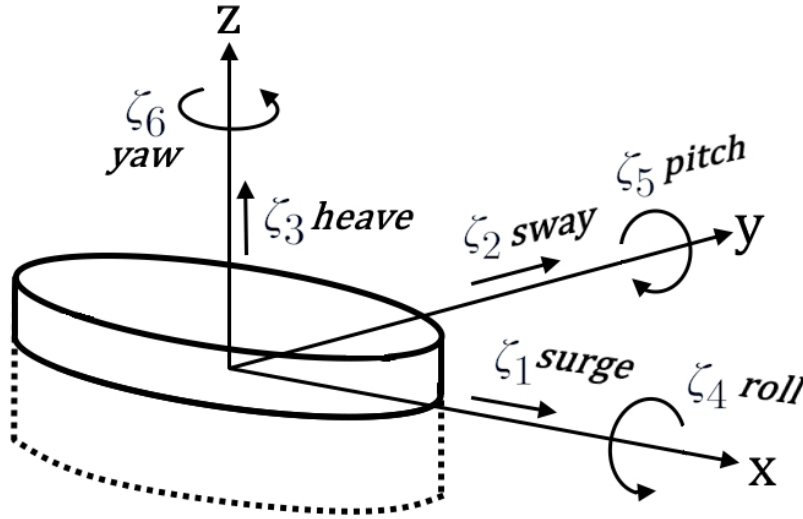


Figure 5.4: Six degrees of freedom (6DOF) of motion for a floating body

In order to calculate the dynamic response for a floating body, the equations of motion need to be solved. Assuming ξ is the displacement vector in 6 degrees, the motions can be characterised by the following equation of motion [16, 48]:

$$(\mathbf{M} + \mathbf{A})\ddot{\xi} + \mathbf{B}\dot{\xi} + \mathbf{C}\xi = \mathbf{F}_{\text{exc}} + \mathbf{F}_{\text{re}} \quad (5.16)$$

Where:

- \mathbf{M} = the mass matrix
- \mathbf{A} = the added mass matrix
- \mathbf{B} = the radiation damping matrix
- \mathbf{C} = the hydrostatic coefficient matrix
- \mathbf{F}_{exc} = the excitation forces vector
- \mathbf{F}_{re} = the reaction forces vector

Using potential flow theory, a force can be written as a function of the velocity potential:

$$F = \int_{S_b} \rho \frac{\partial \Phi}{\partial t} n dS_b \quad (5.17)$$

where n is the unit vector normal to the body's surface, ρ is the density of the fluid and S_b is the wetted surface area. Equation 5.16 can be rewritten and divided into a hydrodynamic force, hydrostatic force and its reaction forces. In accordance with Newton's second law, the general equation of motion for a floating body becomes:

$$m\ddot{\xi} = F_{hd}(t) + F_{hs}(t) + F_{re}(t) \quad (5.18)$$

where m represents the mass, $\ddot{\xi}$ is the acceleration of the device for a particular degree of freedom, $F_{hd}(t)$ is the hydrodynamic force, $F_{hs}(t)$ is the hydrostatic force, and $F_{re}(t)$ is the reaction force. Equation 5.19

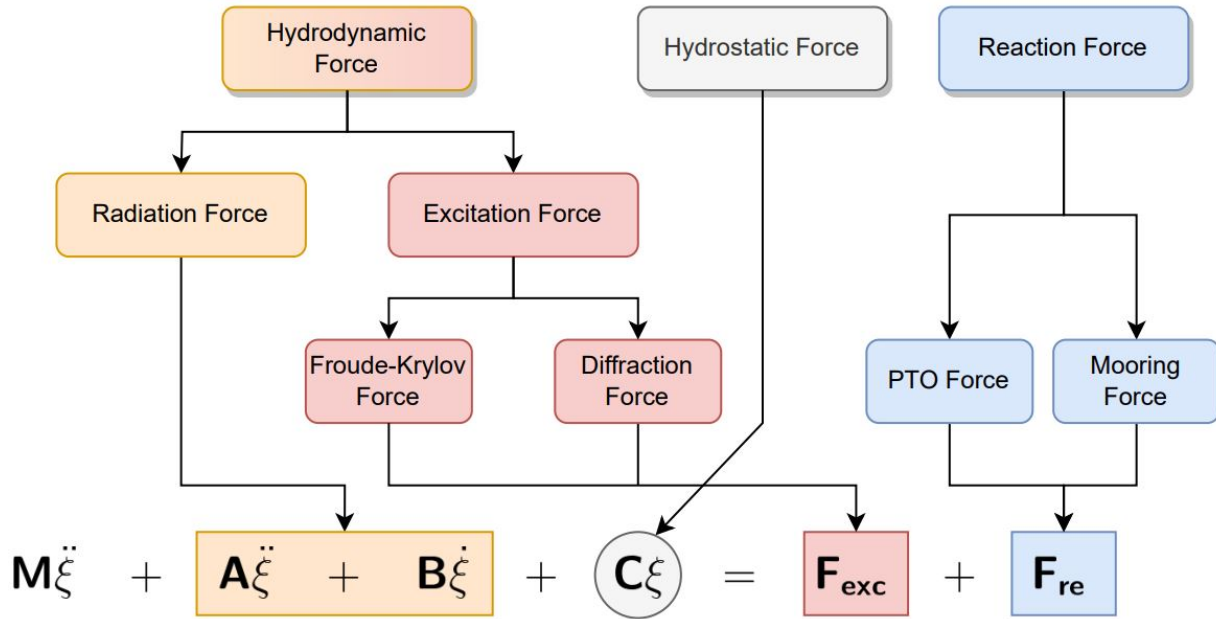


Figure 5.5: Overview of the forces acting on the floating body

shows that the hydrodynamic force can be split into the excitation force and the radiation force while the reaction force can be split into the PTO force and the mooring force [48].

$$\begin{aligned} F_{hd}(t) &= F_{exc}(t) + F_{rad}(t) \\ F_{re}(t) &= F_{PTO}(t) + F_{moor}(t) \end{aligned} \quad (5.19)$$

For the analysis it is assumed that the wave excitation takes a simple harmonic motion meaning that the motions can be described in the frequency domain. By switching from the time domain to the frequency domain, it converts differential equations to algebraic equations making it mathematically easier to solve. In addition, this allows all motions and forces of the device to be described by a complex amplitude (denoted by the hat symbol $\hat{\cdot}$) and a sinusoidal time dependence, $e^{i\omega t}$. The device displacement vector $\xi(t)$ can be written as follows:

$$\xi(t) = \text{Re} \left\{ \hat{\xi}(\omega) e^{i\omega t} \right\} \quad (5.20)$$

It follows that the device's velocity and acceleration vectors can be written as:

$$\dot{\xi}(t) = \text{Re} \left\{ i\omega \hat{\xi}(\omega) e^{i\omega t} \right\} \quad (5.21)$$

$$\ddot{\xi}(t) = \text{Re} \left\{ -\omega^2 \hat{\xi}(\omega) e^{i\omega t} \right\} \quad (5.22)$$

Using equation 5.22, the motion equation 5.18 can be transformed into the frequency domain resulting in:

$$-\omega^2 m \hat{\xi}(\omega) = \hat{F}_{hd}(\omega) + \hat{F}_{hs}(\omega) + \hat{F}_{re}(\omega) \quad (5.23)$$

5.2.1. Hydrodynamic Force

The hydrodynamic force can also be expressed in the frequency domain:

$$\hat{F}_{hd}(\omega) = \hat{F}_{exc}(\omega) + \hat{F}_{rad}(\omega) \quad (5.24)$$

The hydrodynamic force can be determined by substituting the velocity components Φ_I , Φ_D , Φ_R from section 5.1.2 into the definition of a force, using equation 5.17. This yields the following equation [48]:

$$\hat{F}_{hd}(\omega) = i\omega\rho \int_{S_b} (\hat{\Phi}_I + \hat{\Phi}_D)ndS_b - \omega^2\rho \int_{S_b} \sum_{j=1}^6 \hat{\xi}_j \Phi_j ndS_b \quad (5.25)$$

Both the excitation and the radiation force contributions can be seen in equation 5.25. The first term on the right hand side of the equation represents the excitation force by integrating the incident and diffracted wave potential over the wetted surface. The second term represents the radiation force which comes as a result of integration of all the radiation potentials.

5.2.2. Radiation Force

In WEC-Sim, the radiation force is given as:

$$F_{rad}(t) = -A(\omega)\ddot{\xi} - B(\omega)\dot{\xi} \quad (5.26)$$

where $A(\omega)$ represents the added mass term and $B(\omega)$ represents the radiation damping term for a given wave frequency. In the frequency domain, the equation becomes:

$$\hat{F}_{rad}(\omega) = \omega^2 A(\omega)\hat{\xi} - i\omega B(\omega)\hat{\xi} \quad (5.27)$$

5.2.3. Excitation Force

The excitation force can be divided into two separate forces namely; the Froude-Krylov force F_{FK} and the diffraction force F_D .

$$\hat{F}_{exc}(\omega) = \hat{F}_{FK}(\omega) + \hat{F}_D(\omega) \quad (5.28)$$

The Froude-Krylov force F_{FK} is derived from the incident undisturbed wave potential Φ_I and the diffraction force F_D is a result of the diffraction potential Φ_D . As described earlier in section 5.1.3, the body is assumed to be motionless for the calculation of the excitation force.

$$\hat{F}_{exc}(\omega) = i\omega\rho \int_{S_b} (\hat{\Phi}_I \cdot n) dS_b + i\omega\rho \int_{S_b} (\hat{\Phi}_D \cdot n) dS_b \quad (5.29)$$

5.2.4. Hydrostatic Restoring Force

The hydrostatic force is based on Archimedes' principle that when an object is submerged in a fluid, it experiences a buoyancy force that is equal to the weight of the displaced fluid. A change in the displacement of the fluid as a result of the body's motion means a change in the hydrostatic force. This change in pressure causes what is referred to as the hydrostatic restoring force [48]. Integration of the hydrostatic pressure over the wetted surface of the body yields the hydrostatic force which is calculated using the following equation:

$$\hat{F}_{hs} = -C\hat{\xi} \quad (5.30)$$

where C is the hydrostatic coefficient. For a simple heaving point absorber equation 5.31 can be used:

$$C = \rho g S_w \quad (5.31)$$

where the cross-sectional area of the body at the waterline is represented by S_w . For a six degrees of freedom rigid-body, the hydrostatic force and torque vector can be represented by the hydrostatic stiffness matrix C . This matrix is symmetric where the non-zero elements are the following:

$$\begin{aligned}
C_{33} &= \rho g \int_{S_b} n_3 dS_b \\
C_{34} &= \rho g \int_{S_b} y n_3 dS_b \\
C_{35} &= -\rho g \int_{S_b} x n_3 dS_b \\
C_{44} &= \rho g \int_{S_b} y^2 n_3 dS_b + \rho g V z_b - m g z_g \\
C_{45} &= -\rho g \int_{S_b} x y n_3 dS_b \\
C_{55} &= \rho g \int_{S_b} x^2 n_3 dS_b + \rho g V z_b - m g z_g \\
C_{56} &= -\rho g V y_b + m g y_g
\end{aligned} \tag{5.32}$$

The coordinates of the centre of gravity and the centre of buoyancy are given by (x_g, y_g, z_g) and (x_b, y_b, z_b) respectively. The unit vector in heave direction is given by n_3 and the wetted body surface is given by S_b . V represents the volume of the body.

5.2.5. Reaction Force

The reaction forces of wave energy converters are typically caused by the Power Take-Off (PTO) equipment and the mooring system designed for station-keeping of the floating body. The PTO system is a mechanism designed to convert the mechanical power into usable electricity. There are many different types of PTO systems used in WECs but the focus for this thesis is on the linear translational PTO type of system. This PTO mechanism is characterised as a linear-spring damper system. A schematic of a linear PTO spring damper system is shown in figure 5.6. The equation used in WEC-Sim for a linear PTO type is [49]:

$$F_{pto} = -B_{pto}\dot{\xi} - C_{pto}\xi \tag{5.33}$$

The first term on the right hand side of the equation represents the PTO damping force with PTO damping coefficient B_{pto} and the second term represents the PTO spring force with the PTO stiffness coefficient C_{pto} . The behaviour of the PTO system is typically nonlinear but it must be linearised for calculations in the frequency domain to be applied. In the frequency domain the complex amplitude of the PTO force can be expressed as:

$$\hat{F}_{pto} = -i\omega B_{pto}\hat{\xi} - C_{pto}\hat{\xi} \tag{5.34}$$

It is possible to tune the PTO parameters B_{pto} and C_{pto} in order to optimise the total amount of wave energy capture by the WEC. This depends on the dynamics of the WEC.

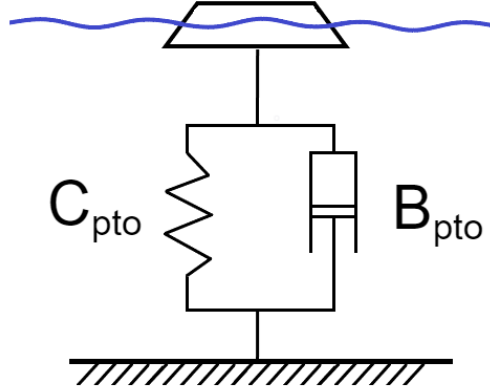


Figure 5.6: Schematic of a linear PTO spring damper system

A mooring system is used for the purpose of station keeping, making sure it does not drift away from its intended position. The mooring force in the frequency domain can be expressed as a linear function of the floating body's motion [48]. The complex amplitude of the mooring force is written as:

$$\hat{F}_{moor} = -C_{moor}\hat{\xi} \quad (5.35)$$

For the scope of this thesis the effect of the mooring system on the behaviour of the WEC has been left out.

5.3. Response Amplitude Operator

From the equation of motion in the frequency domain the following relation can be found [16, 48]:

$$\hat{\xi}(\omega) = \frac{\hat{F}_{exc}(\omega)}{-(m + A(\omega))\omega^2 + i\omega(B(\omega) + B_{pto}) + C + C_{pto}} \quad (5.36)$$

Equation 5.36 calculates the response amplitude operator (RAO) which gives the complex amplitude of the body motion. The PTO parameters B_{pto} and C_{pto} can be tuned to optimise power absorption. The peak of the RAO is known as the resonant frequency ω_n and is the frequency at which maximum power is absorbed by the wave energy converter. For a single-degree of freedom heaving point absorber this can be calculated using equation 5.37:

$$\omega_n = \sqrt{\frac{C + C_{pto}}{m + A}} \quad (5.37)$$

5.4. Power Absorption

5.4.1. Mean Power Capture

Within a wave period, the mean power absorbed by a WEC is the same as the absorbed power by the mechanical damper of the PTO. Only the influence of the mechanical damper of the PTO is taken into account since the average contribution of the mechanical spring to the overall power absorption is zero. The mean absorbed power over one wave period can be calculated, assuming sinusoidal waves:

$$P_a = \frac{1}{T} \int_0^T B_{pto} u_b^2 dt \quad (5.38)$$

Equation 5.38 can be used for a heaving WEC device [48]. u_b denotes the velocity of the body in heave. If the displacement is given as $\xi = |\hat{\xi}| \sin(\omega t)$ and the velocity as $u_b = \omega |\hat{\xi}| \cos(\omega t)$ then it follows that the time averaged power absorption over one wave cycle can be expressed as:

$$\begin{aligned}
P_a &= \frac{1}{T} B_{pto} \left| \hat{\xi} \right|^2 \omega^2 \int_0^T \overline{\cos^2(\omega t)} dt \\
&= \frac{1}{2} B_{pto} \left| \hat{\xi} \right|^2 \omega^2
\end{aligned} \tag{5.39}$$

By substituting the complex motion amplitude from equation 5.36 into equation 5.38 the equation can be written as:

$$P_a = \frac{1}{2} B_{pto} \omega^2 \left| \frac{\hat{F}_{exc}}{-(m + A)\omega^2 + i\omega(B + B_{pto}) + C + C_{pto}} \right|^2 \tag{5.40}$$

5.4.2. Optimal PTO Control

The PTO parameters can be tuned in order to maximise power absorption. The PTO damping can be optimised for a specific wave frequency. If the average significant wave height and wave period are known at the location of deployment then the corresponding PTO damping coefficient can be calculated. The optimal PTO damping coefficient can be found by derivation of equation 5.40 to B_{pto}

$$\frac{\partial P_a}{\partial B_{pto}} = 0 \tag{5.41}$$

This results in an optimal damping coefficient B_{pto} for one specific wave frequency. for a given frequency ω , and radiation terms $A(\omega)$ and $B(\omega)$:

$$B_{pto} = \sqrt{B(\omega)^2 + \left[\omega(m + A(\omega)) - \frac{C}{\omega} \right]^2} \tag{5.42}$$

However, with a varying sea state the PTO damping will not be as efficient. Which is the case for irregular waves. Instead, there are control strategies that can be implemented into the PTO system order to enhance the efficiency of the WEC for all local sea states.

5.5. Time-domain modelling

The equations used up to this point assume steady-state response and are valid for regular waves simulations. In the case for irregular waves however, the fluid memory effect on the dynamic response due to past motion of the body needs to be taken into account. Based on the Cummins equation [48], the radiation force can be calculated by:

$$F_{rad}(t) = -A_\infty \ddot{\xi} - \int_0^t K_r(t - \tau) \dot{\xi}(\tau) d\tau \tag{5.43}$$

The added mass term at infinite frequency is represented as A_∞ . The radiation impulse response function K_r is a function of the radiation damping term $B(\omega)$ and is expressed by:

$$K_r(t) = \frac{2}{\pi} \int_0^\infty B(\omega) \cos(\omega t) d\omega \tag{5.44}$$

An impulse response function (IRF) gives insight into how a system responds over time when an impulse is applied as the input. By solving the linear problem in the frequency domain it is possible to get the hydrodynamic coefficients $A(\omega)$ and $B(\omega)$ which can then be used to derive the time-varying radiation IRF K_r . The excitation force in irregular waves can be expressed according to WEC-Sim as:

$$F_{exc}(t) = \text{Re} \left[R_f(t) \sum_{j=1}^N F_{exc}(\omega_j, \theta) e^{i(\omega_j t + \phi_j)} \sqrt{2S(\omega_j)} d\omega \right] \tag{5.45}$$

Equation 5.45 uses an irregular wave spectrum denoted by $S(\omega)$. This wave spectrum can either be of the Pierson-Moskowitz or of the JONSWAP type. N is the number of frequency bands used in the wave spectrum, ϕ is the randomized phase angle and θ denotes the incident wave direction. For the calculation of the wave excitation force the Ramp function $R_f(t)$ is introduced. The Ramp function is necessary to avoid strong transient flows at earlier time steps.

$$R_f(t) = \begin{cases} \frac{1}{2}(1 + \cos(\pi + \frac{\pi t}{t_r})), & \text{for } \frac{t}{t_r} < 1 \\ 1, & \text{for } \frac{t}{t_r} \geq 1 \end{cases}$$

In addition, the impulse response function of the excitation force can be calculated:

$$K_e(t) = \frac{1}{2\pi} \int_{-\infty}^{\infty} F_{exc}(\omega) e^{i\omega t} d\omega \quad (5.46)$$

By applying the Cummins equation for the heaving point absorber, the equations of motion in the time-domain can be written as:

$$(\mathbf{M} + \mathbf{A}_{\infty})\ddot{\xi}(t) + \int_{-\infty}^t \mathbf{K}_r(t - \tau)\dot{\xi}(\tau)d\tau + \mathbf{C}\xi(t) = \mathbf{F}_{exc}(t) + \mathbf{F}_{PTO}(\xi, \dot{\xi}, t) \quad (5.47)$$

Part III

Methodology

Metocean and Ice Data

For the choice of the investigation site in section 3.2, meteorological data needs to be gathered for the significant wave heights, the peak periods, the sea ice thickness and sea ice concentration. All local meteorological data used in this study was retrieved from the Norwegian Meteorological Institute database [50]. The water depth is estimated as 25 meters based on a global bathymetric dataset, ETOPO1 [51].

6.1. Extracting Time Series of Data

The main data set used from this database for this study is the "NORA3" wave dataset [52]. NORA3, which is an acronym for the 3-km Norwegian reanalysis hindcast is a high resolution dynamically downscaled data set developed by MET Norway. Dynamical downscaling is a tool used to reproduce the local climate by using a lower resolution climate model as its boundary conditions and physical principles in order to get a higher resolution model [52]. This can bring the model from a 30km grid size down to a 3km grid. The wave data is produced by running the wave model WAM cycle 4.7.0, daily ice concentrations from the Copernicus Marine Service and wave spectra from the ERA-5 dataset [52]. Data ranging from the early autumn of 2006 to the early autumn of 2021 were analysed using time series. Based on this data four seasons have been selected, representing cases with different ice conditions. These cases range from ice free conditions to severe ice conditions at this particular site. The years 2010 and 2011 are shown to have the largest sea ice thicknesses and sea ice concentrations of the dataset and are therefore categorised in this study as the moderate and severe ice condition cases. In addition, according to the Finnish Meteorological Institute (FMI), the years 2009 to 2011 are shown to have the largest maximum ice extents over the Baltic Sea in the past 30 years. Season 2006-2007 is described by the FMI as an "average winter" with a maximum ice extent of 140 000 km² [39]. Moreover, the annual maximum ice thickness for this season comes closest to the average annual maximum ice thickness of the dataset as seen in table 6.3. In order to clearly distinguish this season from the other seasons it has been given the "mild" label as this gives the mildest case of sea ice conditions. Season 2019-2020 was a fairly warm winter in the Baltic Sea where this site experiences no ice cover which could provide useful information in contrast to the other winters [39].

Year	Sea Ice Condition
2019 - 2020	Ice Free
2006 - 2007	Mild
2010 - 2011	Moderate
2009 - 2010	Severe

Table 6.1: Characterisation of local ice conditions based on ice thickness data and the Finnish Meteorological Institute [39]

Time series of wave and sea ice parameters were downloaded using the Python source code provided by Christakos' GitHub repository [53]. The code provided proves to be a useful tool for analysing and visualising MET Norway wave data sets. The process involves downloading the repository to your computer, installing and setting up the specified package dependencies which was done using a laptop with the Linux

operating software. This was done since some dependencies were not compatible with other operating software. In order to plot a time series and save the data to a *.csv file, the following line of code was used:

```
import MET_waves
#Coordinates lon=20 lat=60.50
MET_waves.plot_timeseries(start_time='2006-09-15T10:00', end_time='2007-08-31T23:00',
lon=20, lat=60.50, product='NORA3', variable='SIT', write_csv=True, ts_obs=None)
```

From the NORA3 database time series of the variables 'SIT', 'SIC', 'hs', 'tp', were retrieved which represent the **sea ice thickness**, **sea ice concentration**, **significant wave height** and **peak period** respectively. These time series range from the dates 2006-09-15 to 2007-08-31, 2009-09-15 to 2010-08-31, 2010-09-15 to 2011-08-31 and 2019-09-15 to 2020-08-31. The time interval of the extracted time series is 1 hour. An additional time series over a 15 year period was extracted and analysed which is used for the wave scatter diagram in the next section. From this 15 year time series, the highest peak period recorded was 12.28 seconds which is equal to 0.51 rad s^{-1} and the lowest peak period recorded was 1.83 seconds which is equal to 3.43 rad s^{-1} . The code starts of by finding the nearest grid point in the database to the specified coordinates, which in this case is long = 19.998, lat = 60.487. Then the extraction process from the database is initiated.

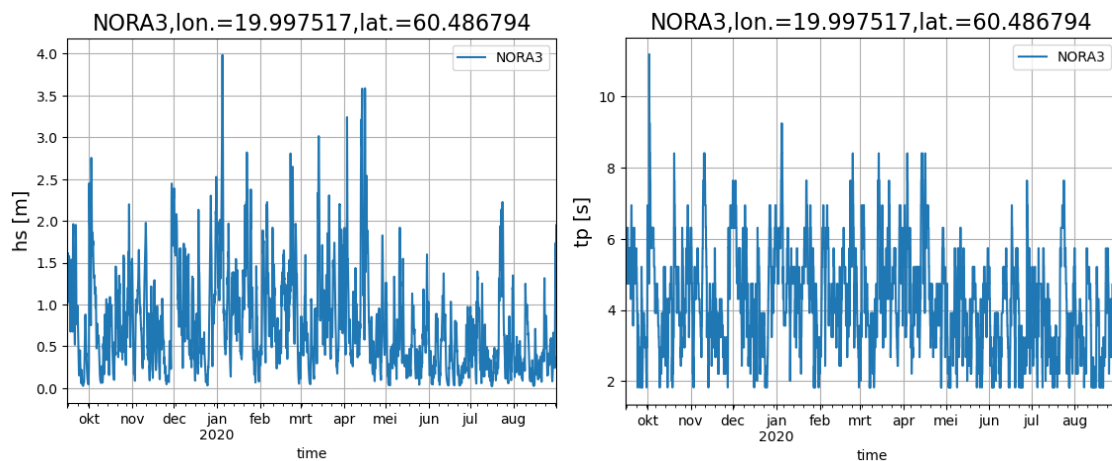


Figure 6.1: Season 2019-2020, Ice Free Conditions

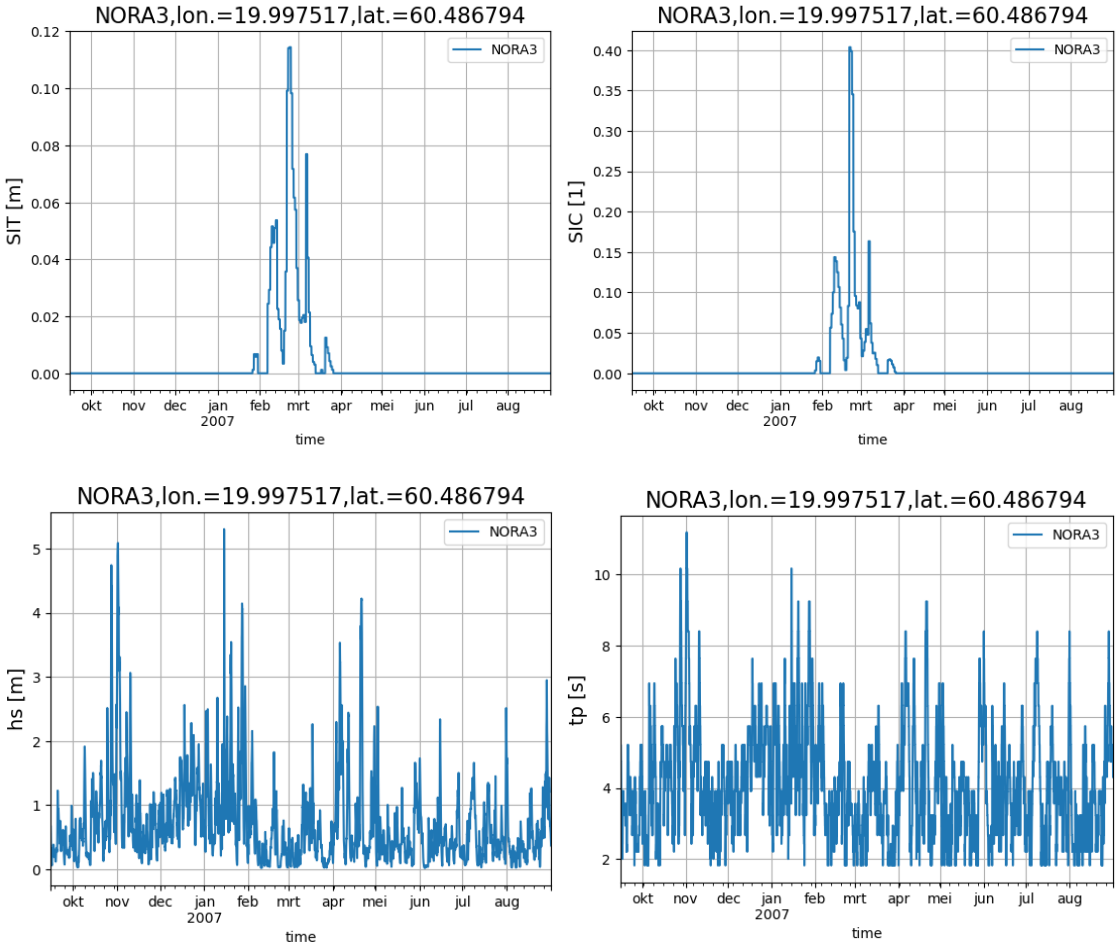


Figure 6.2: Season 2006-2007, Mild Ice Conditions

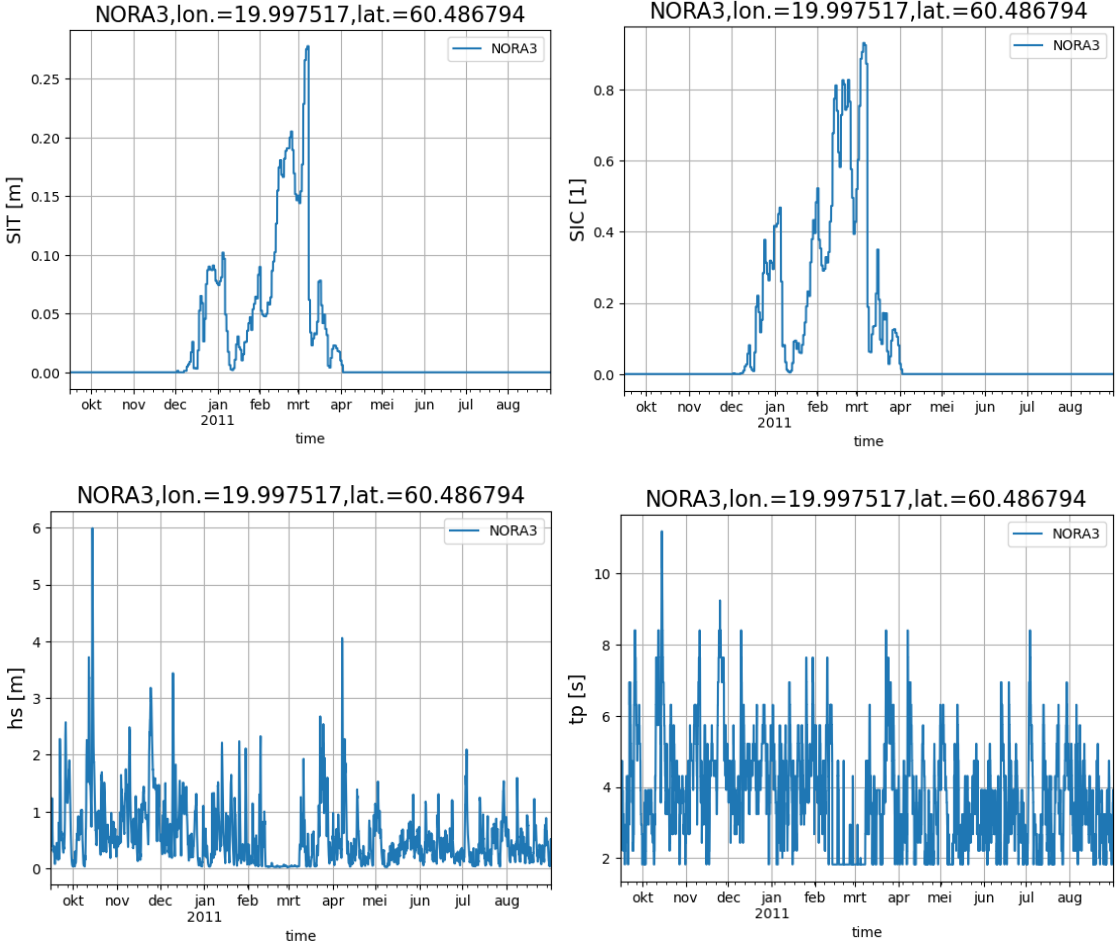


Figure 6.3: Season 2010-2011, Moderate Ice Conditions

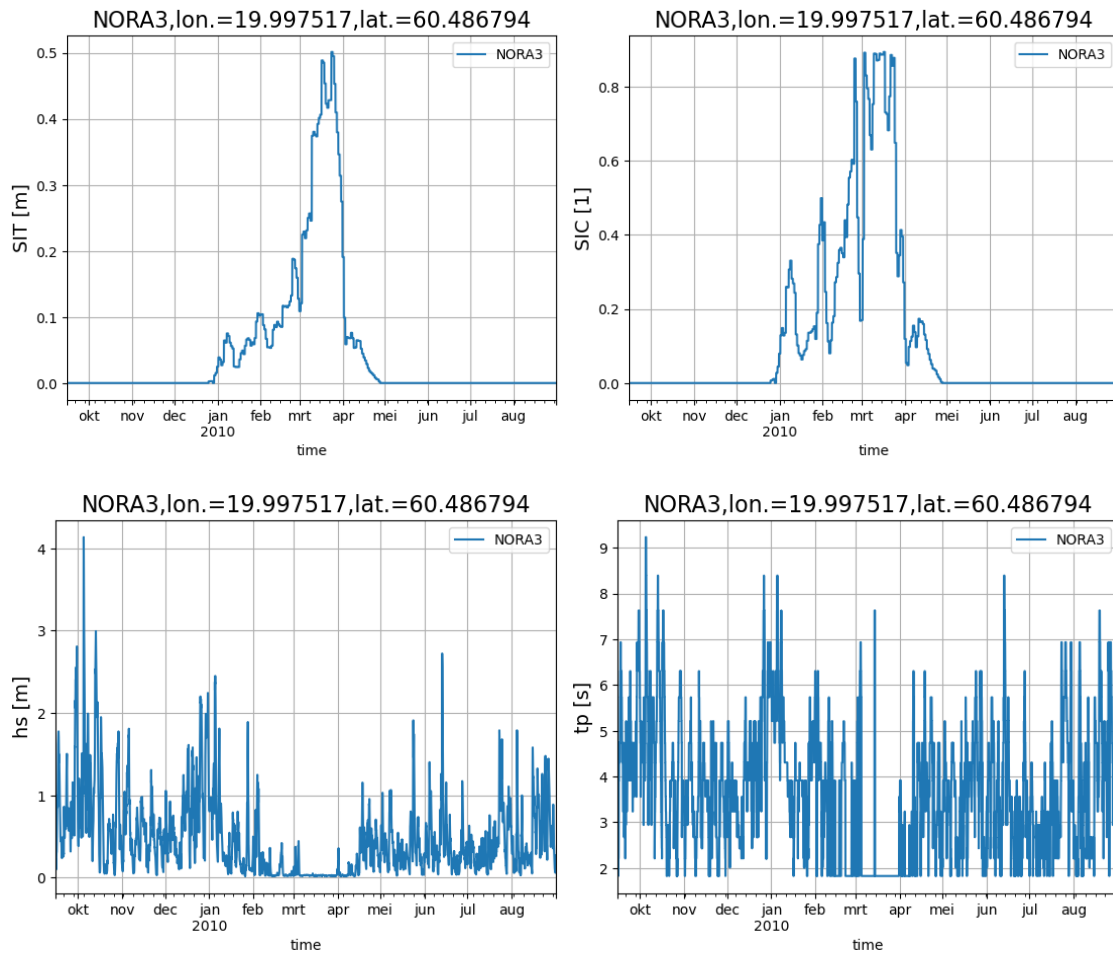


Figure 6.4: Season 2009-2010, **Severe Ice Conditions**

6.1.1. Discussion

From the plots depicted in Figures 6.2, 6.3 and 6.4, it becomes evident that an increase in both sea ice thickness and concentration corresponds to a decrease in significant wave height. The thicker the ice sheet, the more energy is required to break up the sheets. While sea ice concentration and thickness follow similar patterns, it can be argued that sea ice concentration contributes more to wave attenuation compared to ice thickness. As explained in section 4.2, wave propagation heavily relies on the effective wind fetch, with a smaller wind fetch leading to a less developed sea state. This phenomenon is clearly visible for the severe case depicted in Figure 6.4, where the significant wave height (h_s) plunges to zero around mid-February. As the sea ice concentration nears approximately 40% in early February, the effects of wave attenuation becomes very evident. The significant wave height progressively drops down to zero showing minimal to no fluctuations. A slight and temporary decrease in the sea ice concentration in early to mid-February is reflected in a temporary spike in the significant wave height. As the month of April arrives, a significant reduction in ice concentration is observed, and the waves start picking up again as ice sheets begin to break up.

6.2. Sea Ice Statistics

The Finnish Meteorological Institute provides some data on the maximum ice extent that is based on satellite imagery, icebreaker reports and coastal observation data [39]. Figure 6.5 illustrates the maximum ice extent in the Baltic Sea spanning from 1991 to 2020. Notably, the calculation of ice extent excludes areas with less than a 10% sea ice concentration. These statistics give an insight into ice growth trends over the years, showing the annual variation and lends further credence to the annual variation observed in local sea ice data. It is important to note that, when observing the season with the maximum recorded ice extent it coincides with the second-highest sea ice thickness in the local data.

- Season 2006-2007, maximum ice extent was 140 000 km² on February 23rd
- Season 2009-2010, maximum ice extent was 244 000 km² on February 17th
- Season 2010-2011, maximum ice extent was 309 000 km² on February 25th
- Season 2019-2020, maximum ice extent was 37 000 km²

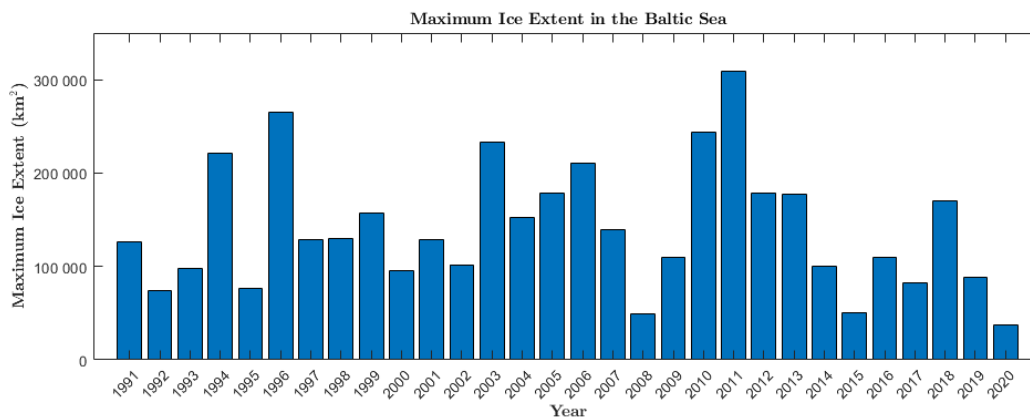


Figure 6.5: Maximum ice extent in the Baltic Sea [39]

Parameter	2006 - 2007	2009 - 2010	2010 - 2011	2019 - 2020	2006 - 2021
Maximum Ice Thickness (cm)	11.45	50.12	27.78	0	50.12
Mean (cm)	3.07	13.79	7.15	0	6.13
Standard Deviation (cm)	3.07	14.04	6.63	0	8.64

Table 6.2: Parameter of ice thickness distribution

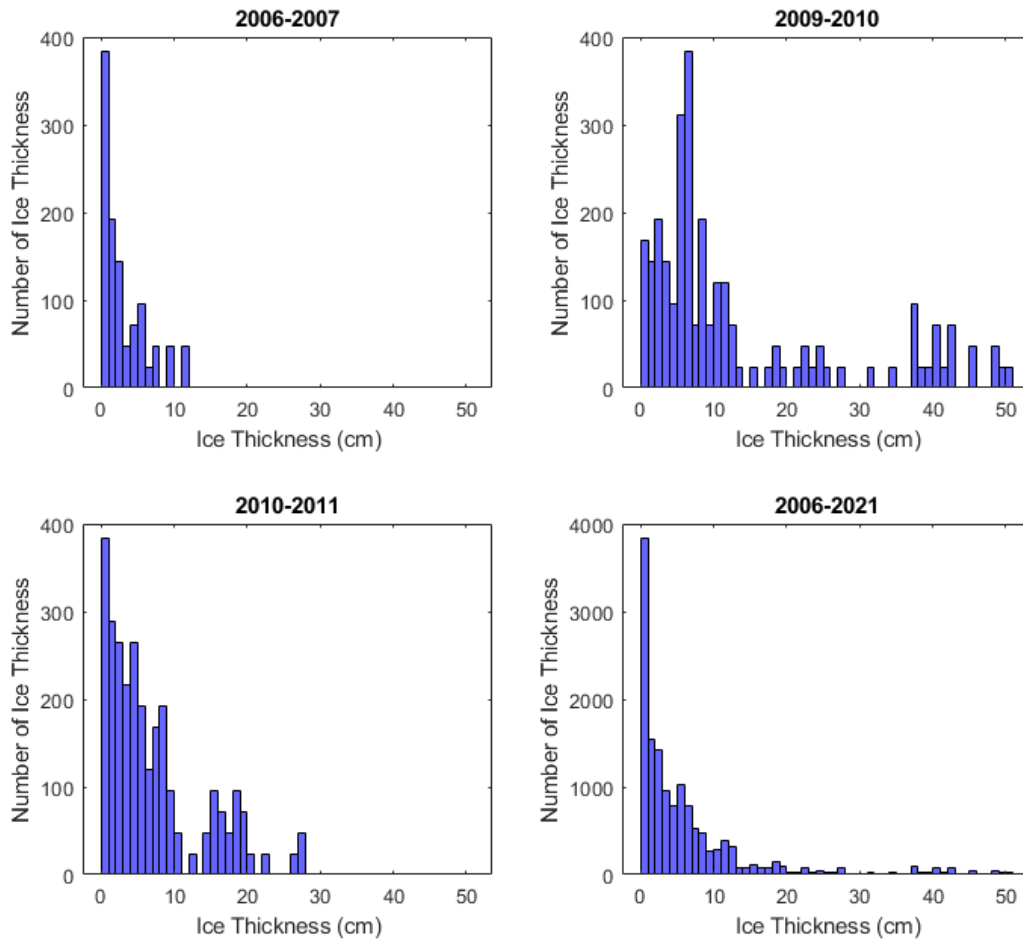


Figure 6.6: Ice thickness distribution

Figure 6.6 shows the the ice thickness distribution during selected seasons. The frequency on the vertical axis considers instances where the ice thickness registers a non-zero value. Remarkably, the year exhibiting the most significant variation in ice thickness coincides with the year showing the highest maximum ice thickness, as detailed in Table 6.2. Moreover, the ice thickness varies not only seasonally but also the year-to-year variability, with some years having little to no sea ice cover while others observe extensive ice coverage. Table 6.3 gives an overview of the maximum ice thickness, ice concentration and number of days with sea ice cover per year spanning from 2006 to 2021. A day with sea ice cover is counted when the sea ice concentration reaches 10% or more.

Season	2006- 2007	2007- 2008	2008- 2009	2009- 2010	2010- 2011	2011- 2012	2012- 2013	2013- 2014	2014- 2015	2015- 2016	2016- 2017	2017- 2018	2018- 2019	2019- 2020	2020- 2021
Max. Ice Thickness (cm)	11.45	0	4.76	50.12	27.78	8.36	13.19	6.01	0	5.74	0	14.13	1.28	0	0.40
Max. Ice Concentration (%)	40.35	0	17.83	89.41	93.05	37.10	73.03	19.31	0	25.91	0	68.75	4.24	0	1.30
Days with Sea Ice Cover	10	0	3	94	79	15	58	6	0	12	0	24	0	0	0

Table 6.3: Annual maximum ice thickness, ice concentration and number of days with sea ice cover at investigation site

To evaluate the survivability of offshore structures subjected to environmental forces, a systematic approach is adopted to estimate the thermally grown extreme ice thickness. Initially, the process involves determining the yearly maximum ice thicknesses as is seen in Table 6.3. Where after, these values are arranged in

ascending order based on their magnitude. Plotting these ordered values on a graph needs to be done by calculating their recurrence intervals, which is derived from their respective probability of exceedance. A logarithmic fit is then applied in a least squared sense to extrapolate extreme ice thicknesses corresponding to given return periods. In this study, an operational lifetime of 20 years is assumed and a 50-year return period is used as is recommended for WEC survivability outlined by Coe and Neary [54]. As depicted in Figure 6.7, the findings indicate a 50-year return value of about 60 cm for the site. It is important to note that the estimations for the extreme ice thicknesses are based on historical ice occurrences which does not take into account effects of climate change. This might lead to an overestimation of the ice thickness. Nevertheless, since there is no credible prediction model that exists for this particular site it is often the best estimate. For this estimation, the most recent data on the annual maximum ice thicknesses is used.

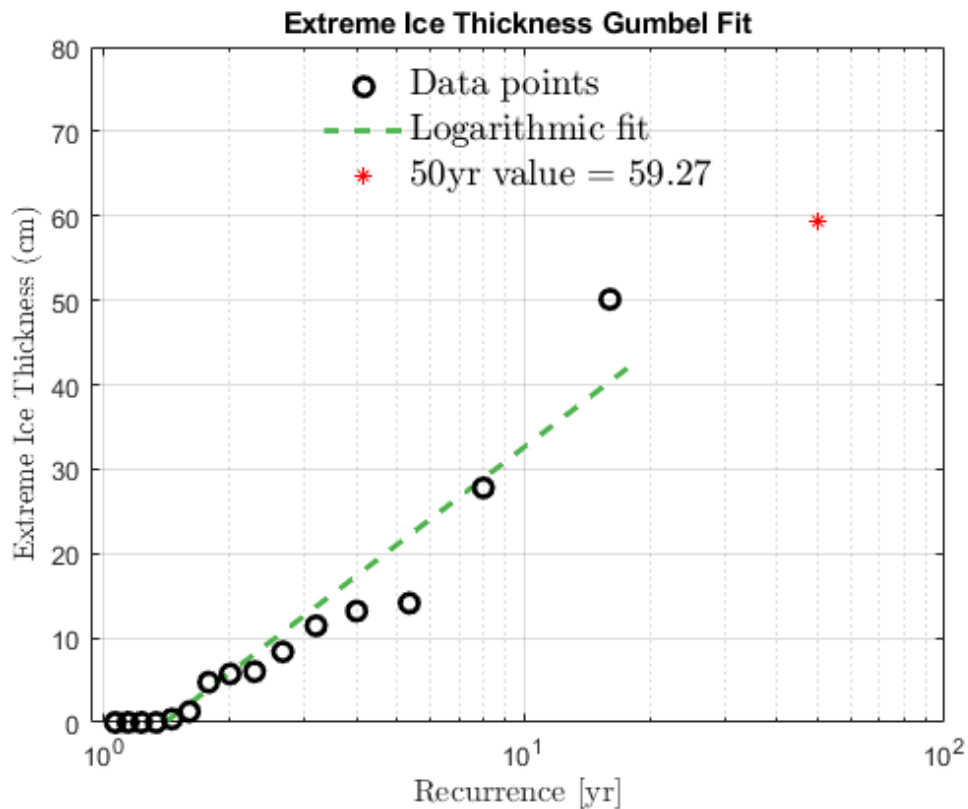


Figure 6.7: Gumbel fitted plot with the return period for extreme ice thicknesses

6.3. Wave Scatter Diagrams

In irregular waves, a sea state can be characterised by an ocean wave spectrum such as the JONSWAP or Pierson-Moskowitz spectrum as explained in section 2.1.2. These spectra can accurately represent a sea state recorded over a three hour period. Wave scatter diagrams can be characterised as long-term statistical representations of multiple sea states. It typically gives wave data for a given year(s) at a particular location. In this diagram, every bin represents one particular sea state for a given significant wave height H_s and peak period T_p and show the bivariate distributions of the H_s and T_p time series extracted in section 6.1. The first diagram shows the number of occurrences in each bin and the second diagram shows the chance of occurrence in each bin in percentages. Figures 6.10 to 6.17 show the scatter diagrams that were generated using python and the "binned statistic 2d" function from the Scipy package [55]. The code for this can be found in the appendix.

Aside from this, the wave power density curves in kilowatts per unit wave crest length are also displayed in the figures. These curves are calculated using equation 6.1 [16].

$$P = \frac{\rho g^2}{64\pi} T_e H_s^2 \tag{6.1}$$

T_e represents the energy period. Based on a standard JONSWAP spectrum with a peak enhancement factor of 3.3, the relationship between the energy period T_e and peak period T_p is shown to be $T_e = 0.9T_p$ [56]

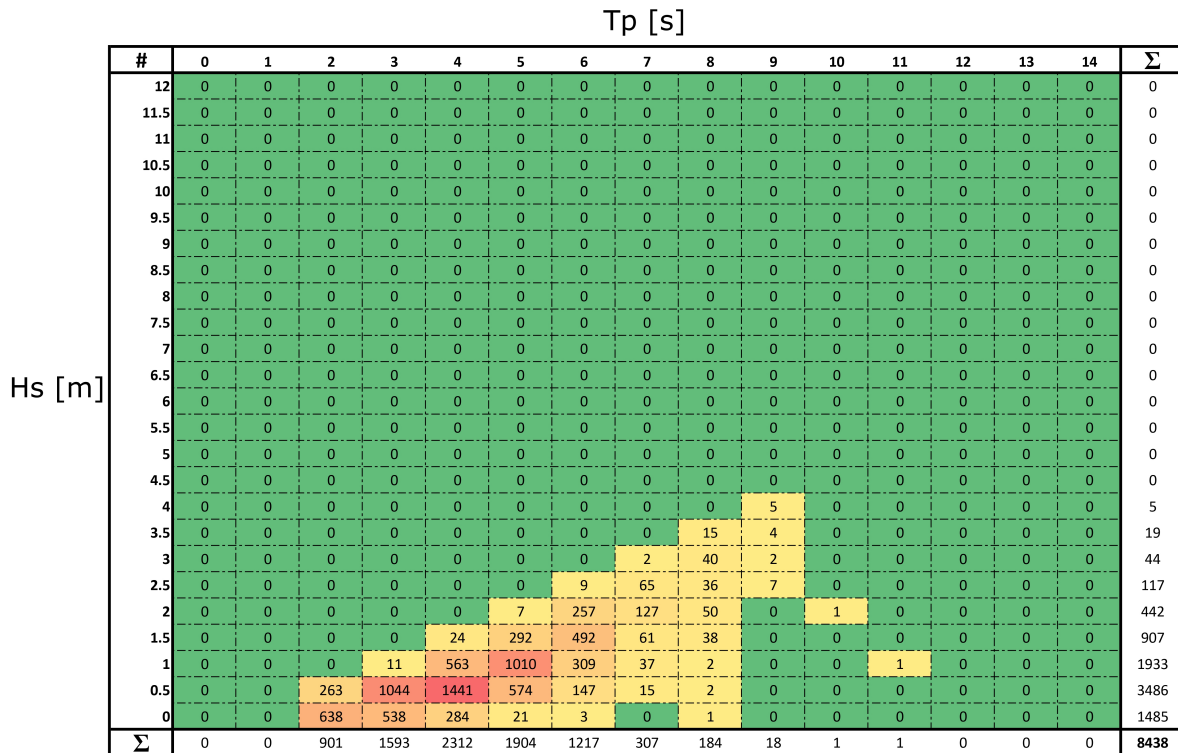


Figure 6.8: Wave scatter diagram of season 2019-2020, Ice Free, number of occurrences = 8438

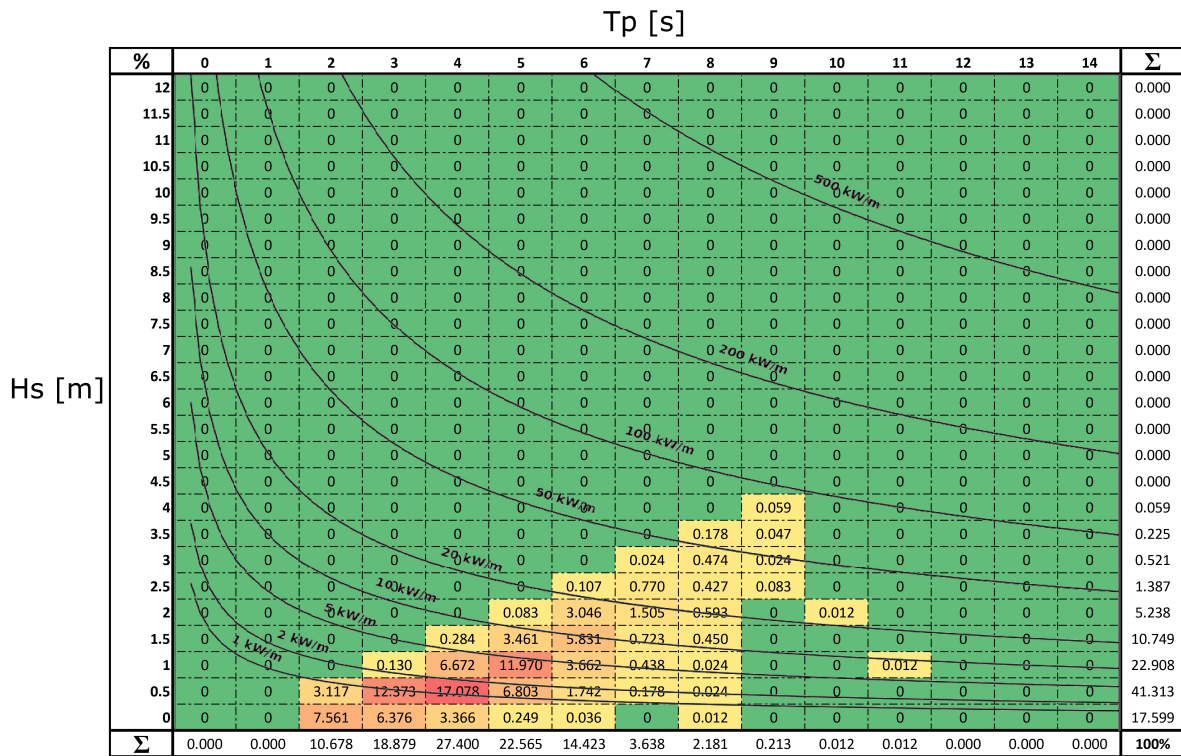


Figure 6.9: Wave scatter diagram of season 2019-2020, Ice Free, shown in percentages and the curves represent the wave power density obtained with eq. 6.1

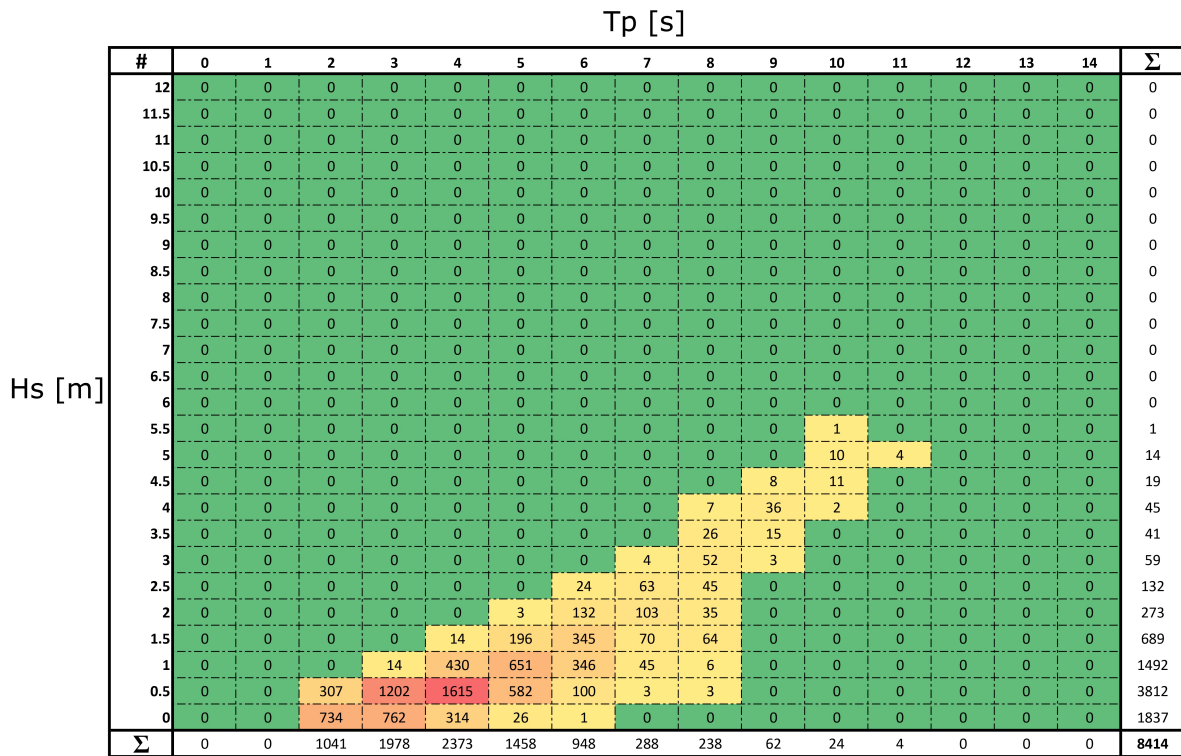


Figure 6.10: Wave scatter diagram of season 2006-2007, Mild Ice Conditions, number of occurrences = 8414

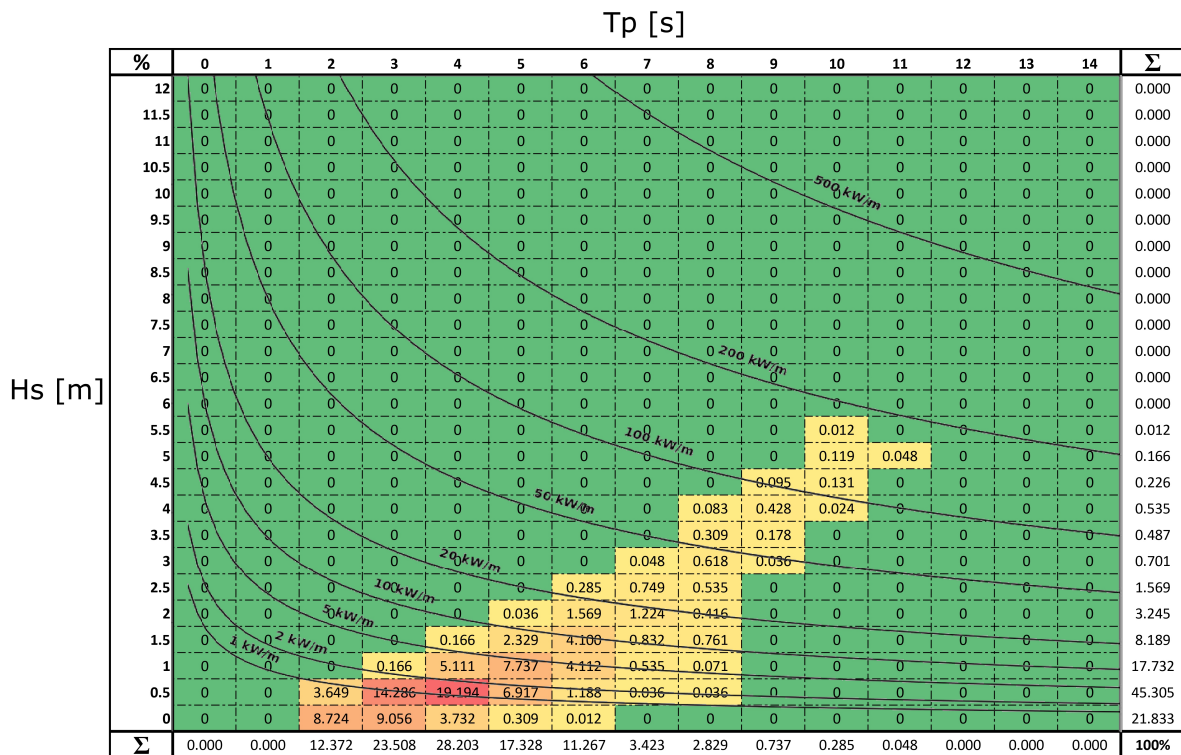


Figure 6.11: Wave scatter diagram of season 2006-2007, Mild Ice Conditions, shown in percentages and the curves represent the wave power density obtained with eq. 6.1

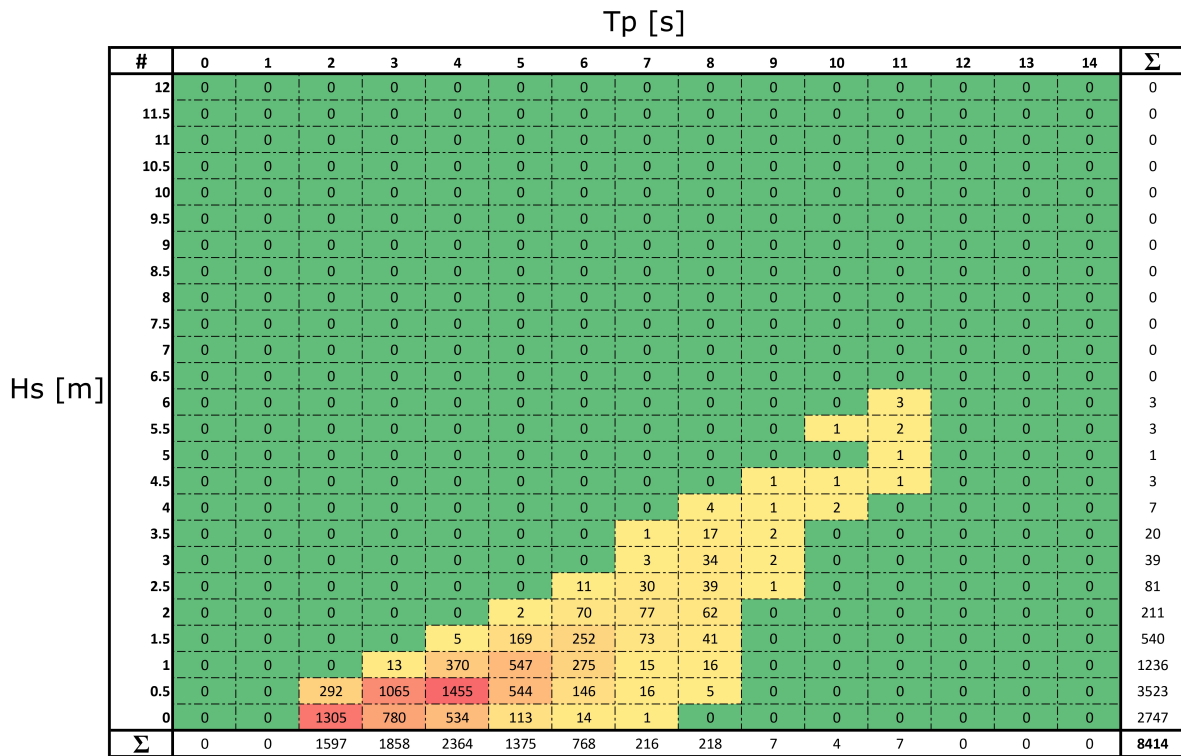


Figure 6.12: Wave scatter diagram of season 2010-2011, Moderate Ice Conditions, number of occurrences = 8414

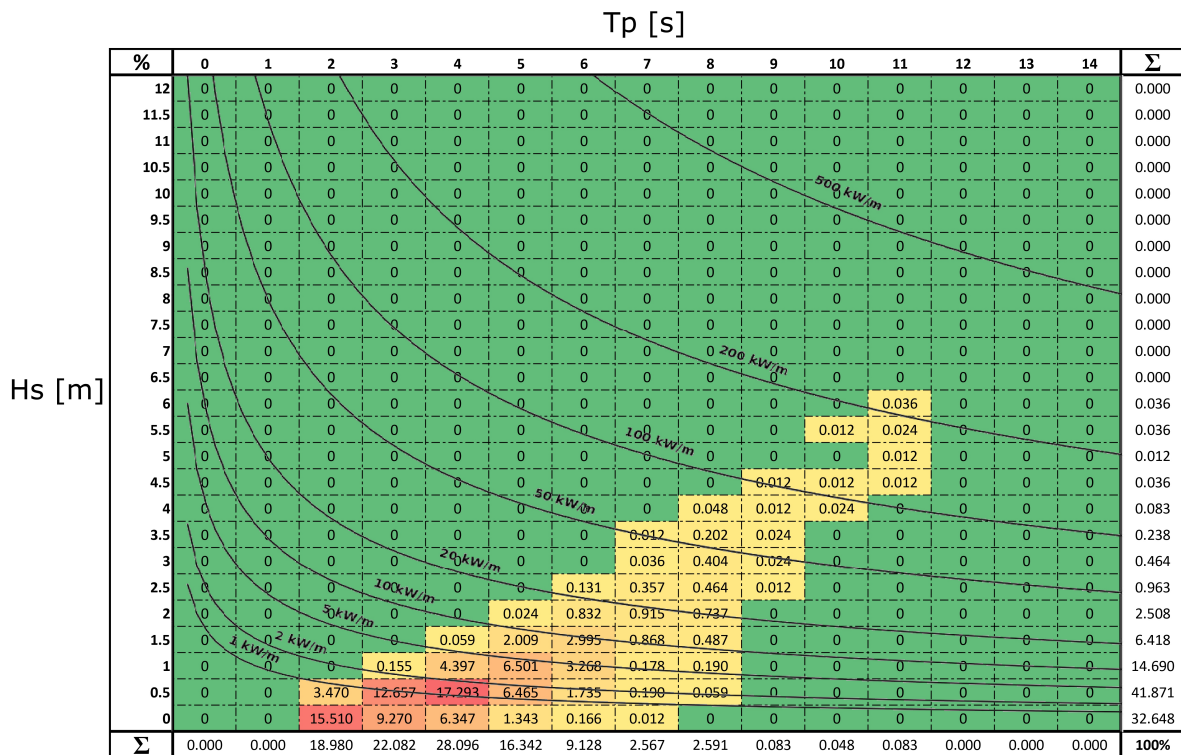


Figure 6.13: Wave scatter diagram of season 2010-2011, Moderate Ice Conditions shown in percentages and the curves represent the wave power density obtained with eq. 6.1

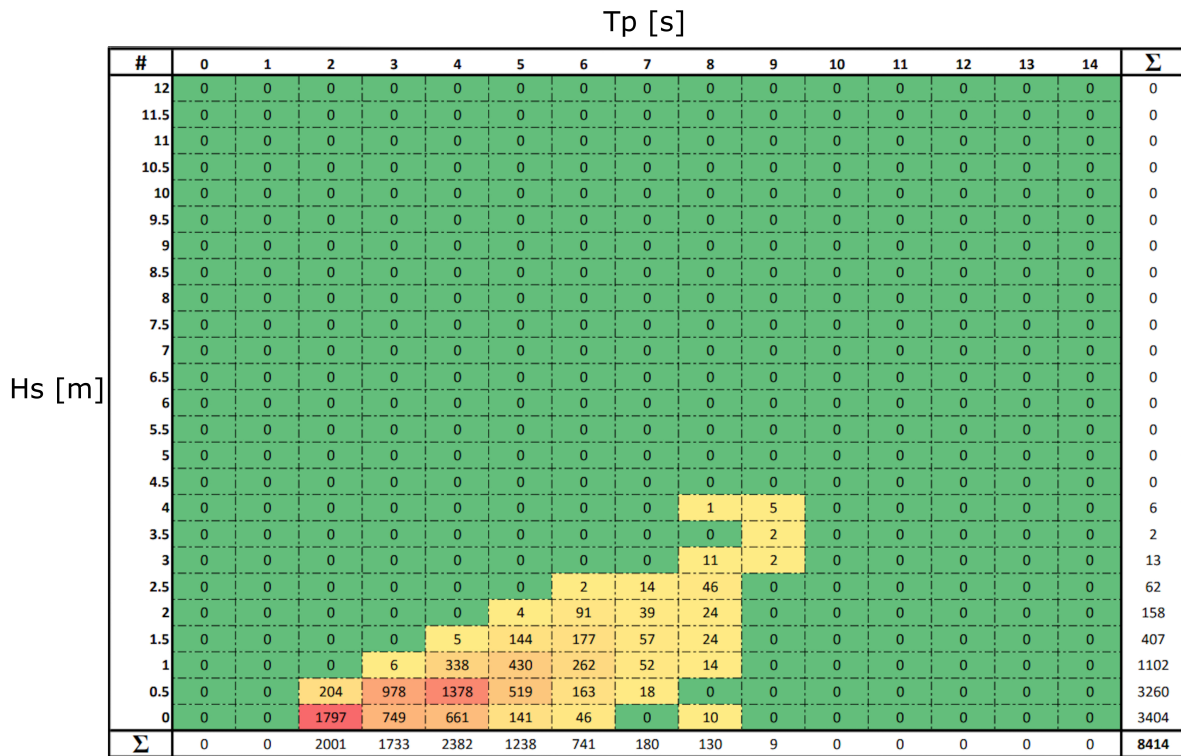


Figure 6.14: Wave scatter diagram of season 2009-2010, **Severe Ice Conditions**, number of occurrences = 8414

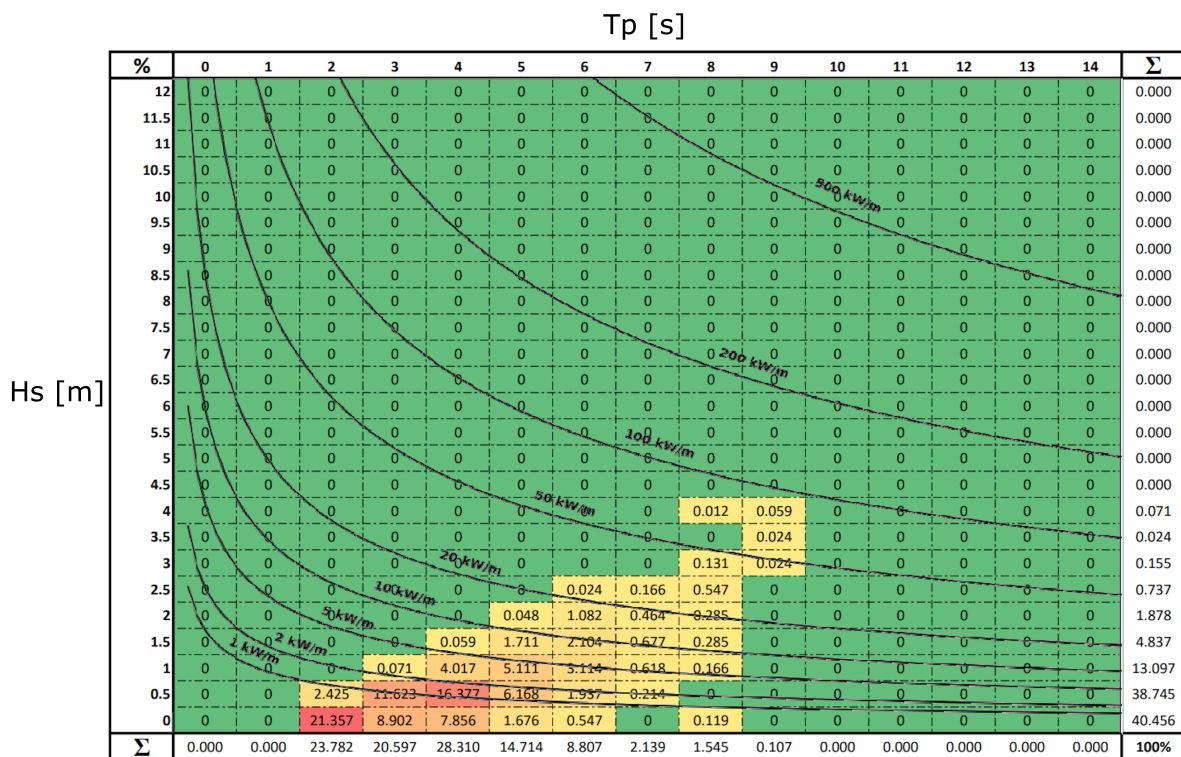


Figure 6.15: Wave scatter diagram of season 2009-2010, **Severe Ice Conditions**, shown in percentages and the curves represent the wave power density obtained with eq. 6.1

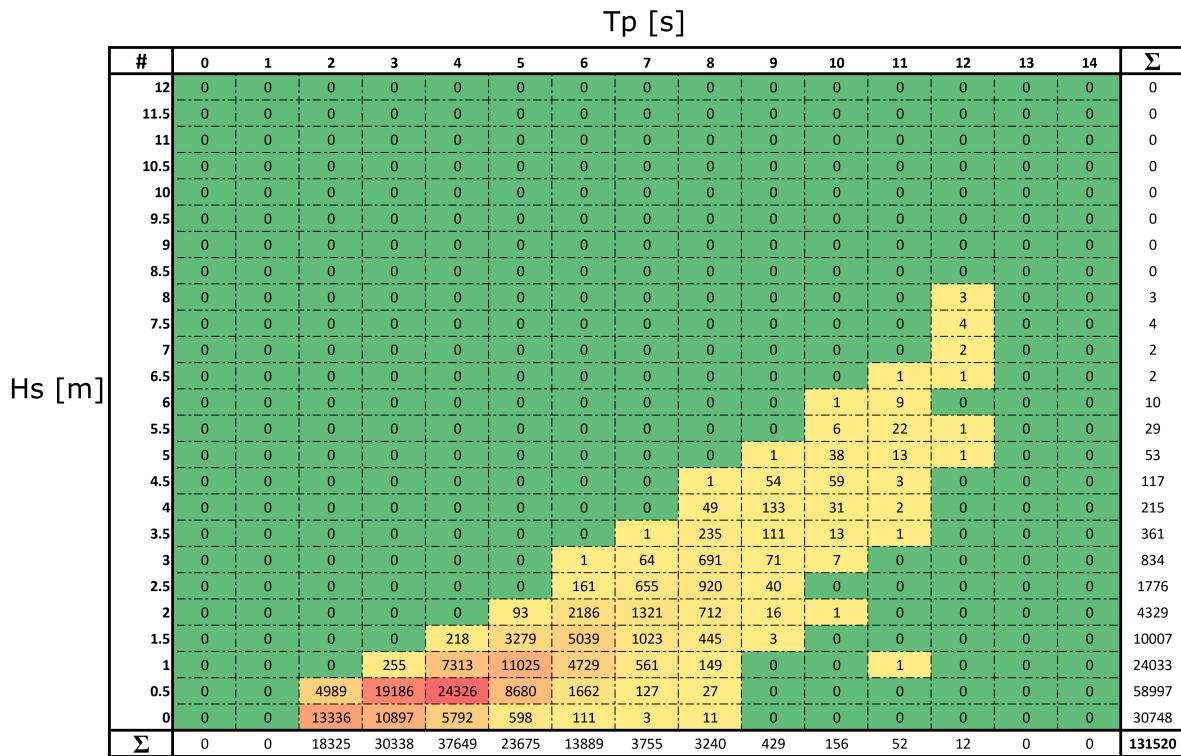


Figure 6.16: Wave scatter diagram September 2006 - September 2021, number of occurrences = 131520

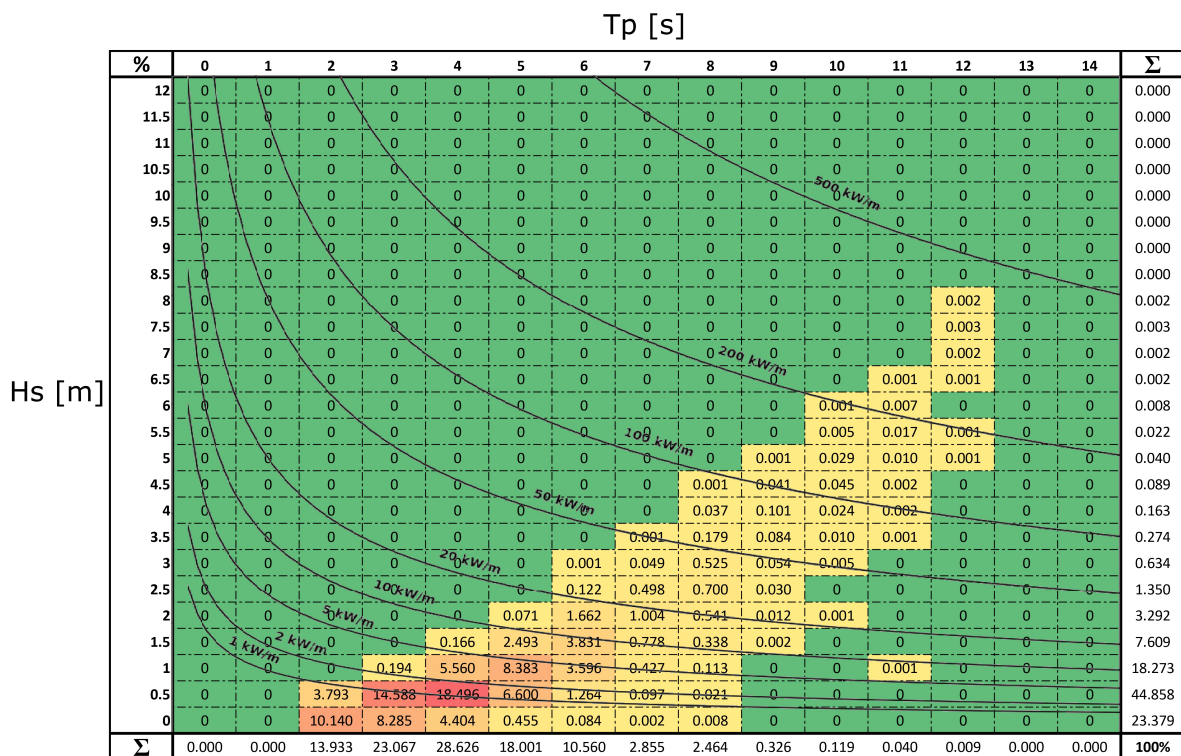


Figure 6.17: Wave scatter diagram September 2006 - September 2021, shown in percentages and the curves represent the wave power density obtained with eq. 6.1

6.4. Extreme Value Analysis

Extreme value analysis (EVA) is a statistical method commonly used in the offshore industry in order to assess and predict the occurrence of extreme sea states. These extreme events can be characterised by parameters such as extreme wave heights or wind speeds which has a direct impact on the safety, survivability and operability of offshore structures and systems. In offshore engineering, one of the major applications of EVA is to estimate the probabilities of extreme events with return periods beyond the range of available data. Return period refers to the average time between the occurrences of events of a certain magnitude. For instance, a 100-year return period event has a one in a hundred probability of being exceeded in one year. This probability changes for a particular time frame so that the chance of experiencing a 100-year extreme event in 50 years is about 39%. This can be calculated using the following formula [57]:

$$1 - (1 - p)^n \quad (6.2)$$

The p represents the annual probability of exceedance (e.g. 1/100 for a 100-year event) and n represents the return period in years. For the design of offshore structures selecting an appropriate return period is vital to ensure survivability. Even though a 100-year return period is commonly used as a design criterion in the offshore industry, Coe and Neary (2014) [54] suggest that for WEC survivability a 50-year return period can be used.

6.4.1. Extreme Wave Height (univariate EVA)

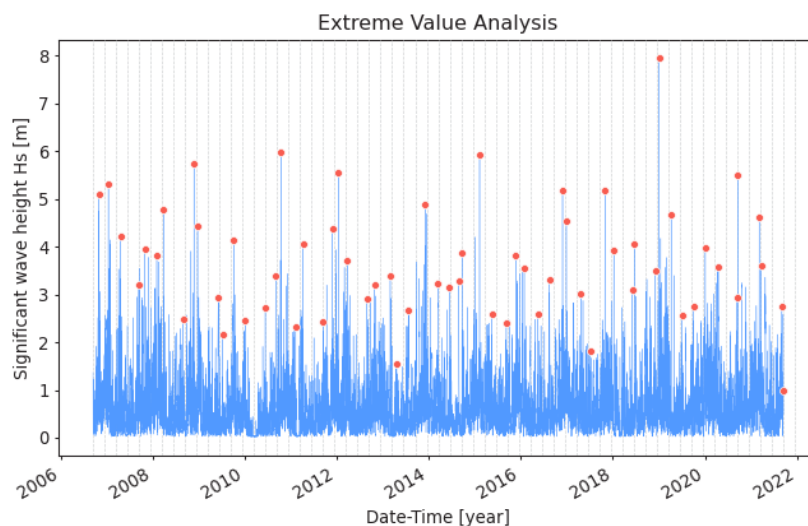


Figure 6.18: Extraction of extreme values over a 15 year period using the 'Block Maxima' method

To estimate the 50-year extreme wave height at a given site, a univariate EVA approach can be employed. This can be achieved by firstly extracting extreme wave heights using the 'Block Maxima' method used in this study or the 'Peaks Over Threshold' method [57]. The 'Peak over threshold' method, as the name implies, identifies the peaks from a time series above (or below) a certain threshold value. The 'Block Maxima' method divides the time series into equally sized blocks and finds the maximum (or minimum) value for each block as is seen in figure 6.18. The red dots represents the peaks within each block and is characterised as an extreme value in the data set. In this case each year is divided into four blocks meaning that for a 15 year period a total of 60 extreme values are selected. Selecting a too small block size can lead to estimation bias and extrapolation whereas selecting a too large block size can lead to large estimation variance. Therefore careful consideration is needed when selecting the right block size.

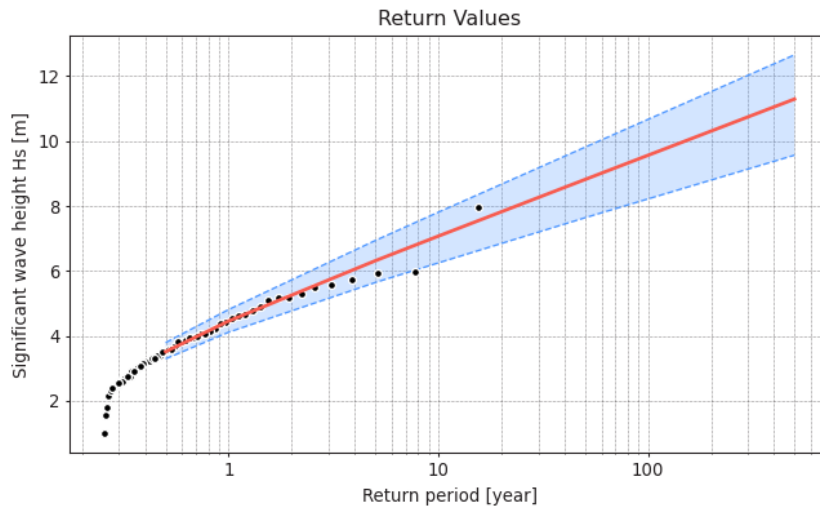


Figure 6.19: Return value plot of extreme wave heights at given return periods

After the extreme values have been selected for each block a distribution can be fitted that is believed to represent the extreme values well. In the case of EVA, the generalised extreme value (GEV) distribution is commonly used. The shape, location and scale parameters of the distribution can be determined using the method of maximum likelihood estimation (MLE). The MLE method finds the parameters that provide the best fit to the extreme values of the dataset which can later be visually checked using the QQ plot as seen in the appendix figure. Figure 6.19 shows the estimations of extreme wave heights at given return periods indicated by the red line. A width of the confidence interval of 95% is used which can be seen by the blue area indicating the lower and upper confidence interval bounds in the graph. The extreme values are seen scattered as black dots along the curve and should align with the estimated return values. The code used for the computations of the extreme wave heights were made using the open-source Python package 'Pyextremes' version 2.3.2 [57] and the data used is the extracted time series of H_s over a period of 15 years as explained in section 6.1.

<i>Return Period [yrs]</i>	<i>Hs [m]</i>	<i>lower ci [m]</i>	<i>upper ci [m]</i>
1	4.46	4.12	4.81
5	6.31	5.64	6.94
10	7.07	6.25	7.81
50	8.81	7.64	9.81
100	9.56	8.22	10.67
500	11.29	9.56	12.65

Table 6.4: Extreme significant wave heights based on different return periods and their confidence intervals (ci)

6.4.2. Environmental Contours (bivariate EVA)

Extreme sea states are not only characterised by their extreme significant wave heights but also by their peak periods. The joint distribution of both variables can be used to determine design load cases for a WEC using the environmental contour method. One way to model these joint distributions are by using the global hierarchical model [58]. This model takes one variable as independent and considers the other variables to be dependent on this variable. For this case, the significant wave height is taken as the independent variable and fitted using an exponential Weibull distribution while the peak period is fitted with a conditional log-normal distribution using dependence functions. The sea states with a return period of 50 years are characterised by the environmental contour line. Along this contour is where the extreme design load cases can be found. Plotting of the environmental contours can be done following the steps of the

inverse FORM technique as described in Berg [58]. These computations were done using the open-source python package viroconcom (version 2.2.0) of the software ViroCon [59].

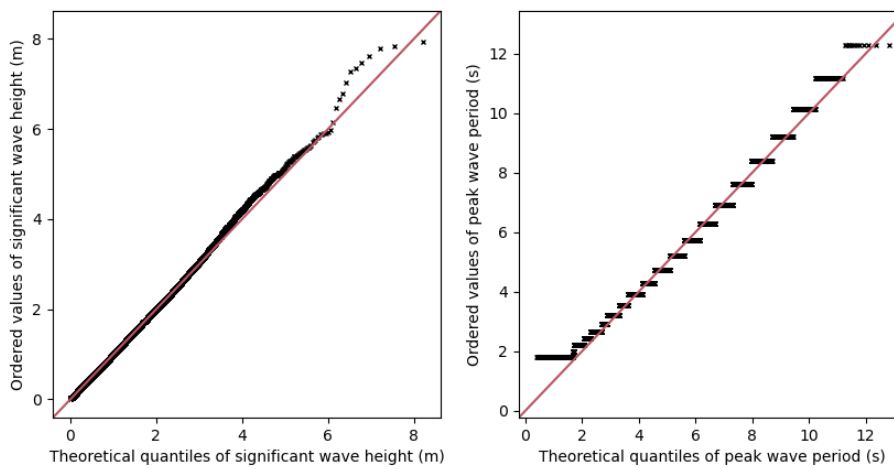


Figure 6.20: QQ plots of the significant wave height and the peak wave period

In order to assess whether a set of data follows a particular theoretical distribution a quantile-quantile (QQ) plot can be used. Figure 6.20 shows the QQ plot of the significant wave height and the peak wave period. Visual examination reveals that the data follows the theoretical quantiles fairly well especially for lower quantiles.

Weibull parameters	α_{H_s}	β_{H_s}	δ_{H_s}
	0.4000	0.84355	1.9244
Lognormal mean μ	a	b	c
	0.89633	12.8589	1.0
Lognormal std. dev. σ	a	b	c
	0.0016	0.3637	1.2713

Table 6.5: H_s and T_p joint distribution parameters

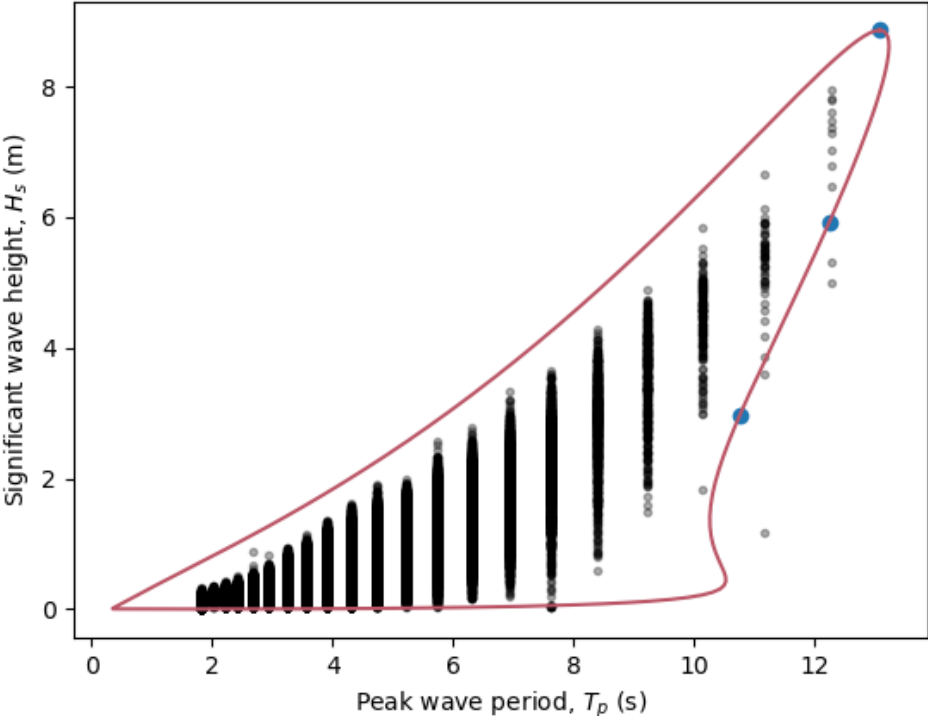


Figure 6.21: Environmental contour for a 50-year sea state

Significant wave height H_s (m)	2.95	5.91	8.86
Peak wave period T_p (s)	10.7	12.2	13.1

Table 6.6: Design sea states based on the 50 year contour

Numerical Modelling

7.1. Overview of WEC-Sim

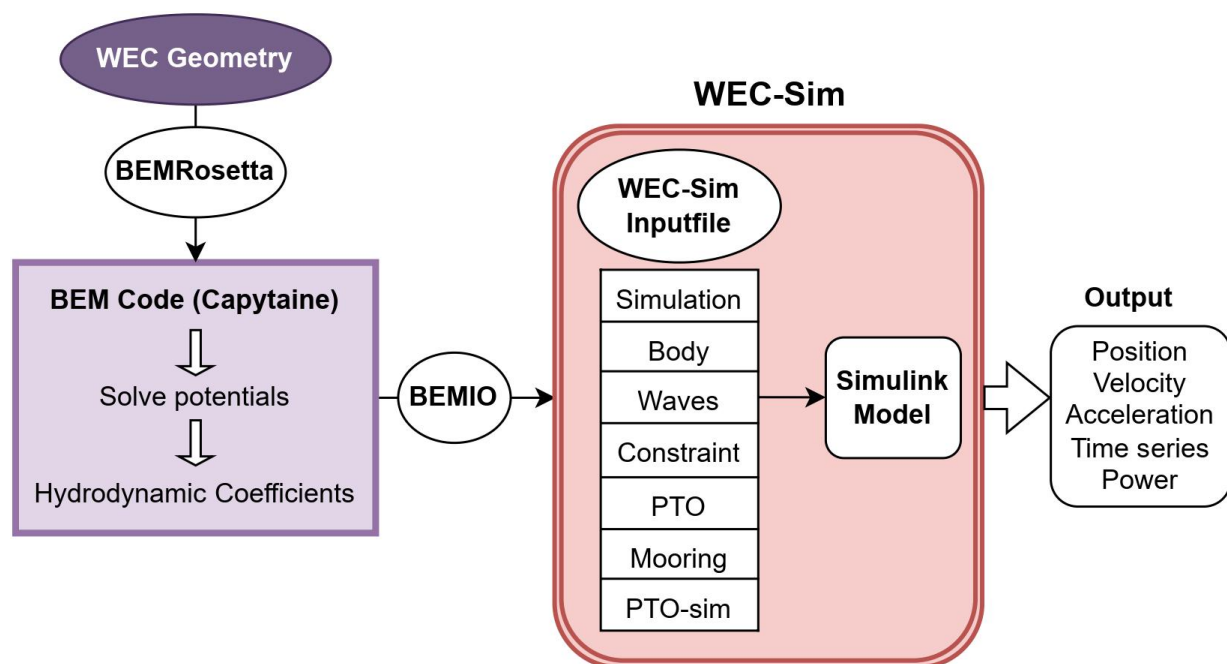


Figure 7.1: Flowchart of the numerical processes

Firstly, a CAD model needs to be created and exported as a mesh which is used as input into the BEM code. Several BEM solvers are available for this purpose, including WAMIT, Aqwa, NEMOH and Capytaine [60] [61]. For this study, Capytaine was chosen as the preferred BEM solver. Capytaine is an open source Python package that uses linear potential flow wave theory in order to analyze the interaction between waves and floating bodies. Capytaine is an open-source Python package that uses linear potential flow theory to evaluate interactions between waves and floating structures. It is important to note that the source code is built upon the foundation of NEMOH which was developed by Gérard Delhommeau, Aurélien Babarit, and their team at École Centrale de Nantes. Therefore, the theoretical framework in this thesis is based on documentation provided by both NEMOH and Capytaine. These BEM solvers solve radiation and diffraction problems in the frequency-domain and solve for the hydrodynamic coefficients. The relevant parameters obtained are; the added mass, radiation damping, wave excitation and hydrostatic stiffness. Before running WEC-Sim [49], Boundary Element Method Input/Output (BEMIO) functions are used to pre-process and structure the BEM hydrodynamic data into Hierarchical Data Format 5 (HDF5) files. These files contain internationalised hydrodynamic coefficients, simplifying the process of reading results from BEM solvers for WEC-Sim. WEC-Sim, which stands for Wave Energy Converter Simulator, can be initiated once this preprocessing is successfully completed. To run the simulation in WEC-Sim the following key

components are required:

- The geometry file (in *.stl format)
- The hydrodynamic data (in HDF5 format)
- A WEC-Sim input file
- A Simulink model of the WEC system

It is important to note that in WEC-Sim, the origin of the geometry file must be placed at the models centre of gravity. This is different from BEM solvers such as Capytaine and Nemoh, which require that the origin of the geometry file aligns with the water plane's position. The WEC-Sim input file is used to define the wave and simulation class, give information about the PTO, oscillating body, and any constraints that need to be considered. The Simulink model plays a major role in describing the interaction between bodies, the PTO system, and the constraints that have been defined, all of which are implemented using WEC-Sim library blocks.

7.2. Geometry

A 3D geometry of the WEC is created using the CAD modelling software Autodesk Fusion 360. The geometry is made to resemble the hexagonal slope shaped torus buoy used in project WESA[44], see section 3.1. Maintaining the same dimensions, the outer diameter of the body should be 6 meters wide, the height 1 meter and the slope to the vertical should be 30 degrees. As stated in section 7.1, it is essential for the origin of the geometry file to align with the water plane's position for the BEM solver. This alignment can be achieved through a straightforward calculation of the draft, which is determined using a simple calculation of the Archimedes' principle in still water. As seen in figure 7.2, force equilibrium is reached when the gravitational force F_g equals the buoyancy force F_b . The buoyancy can be calculated using the submersed volume denoted as ∇_{sub} , the gravitational constant g and the density of water ρ_w . When dealing with brackish waters, it is assumed that the density of water is 1005 kg m^{-3} which is the average water density in the Baltic Sea [62]. For force equilibrium in the absence of external forces equation 7.1 can be used.

$$\rho_w \nabla_{submersed} \mathbf{g} = (\mathbf{m}_{buoy} + \mathbf{m}_{translator}) \mathbf{g} \quad (7.1)$$

The immersed volume is calculated using equation 7.1. The total mass used in the systems equation of motion consists of both the mass of the buoy and the mass of the translator, which are 3 and 5 tons respectively. This mass is based on the WEC systems used in project WESA [36]. The draft can be calculated from the immersed volume through a process of removing segments from the top and measuring the total volume until it matches the immersed volume. After the draft is calculated, the origin can be aligned with the position of the water plane.

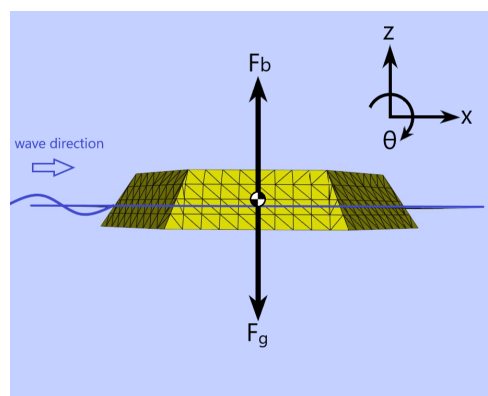


Figure 7.2: Illustration of forces acting on the floating body assuming still water

Once the geometry is created, the number of panels can be specified and the model can be exported to a mesh format (*.stl) file. This file is loaded into BEMRosetta [63], an open-source program that can

convert mesh files into readable input files for various BEM solvers. In addition, the program can be used to visualise the mesh, make comparisons and check for errors. Figure 7.3 shows a mesh of the WEC created. Using BEMRosetta, the boundary surface of the floating body is discretised into a set of triangular panels and the mesh consists of a list of vertices and a list of faces. All faces are defined as quadrangular with triangular faces sharing two identical vertices. BEMRosetta is used to convert the mesh file into a *.dat file which can be used as input for BEM solvers like Capytaine and Nemoh. The mesh resolution used for the study is 1308 panels which is proven to be adequate based on the grid convergence analysis performed in section 7.5.1.

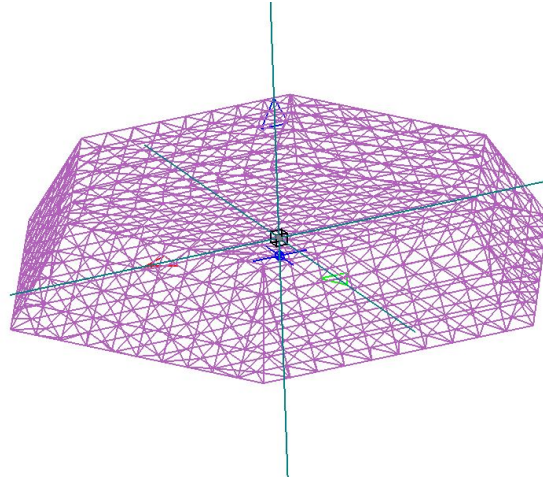


Figure 7.3: Geometry of WEC meshed in BEMRosetta

<i>Parameter</i>	<i>Value</i>	<i>Unit</i>
# Panels	1308	-
# Nodes	656	-
Volume	18.57	m ³
Immersed volume	7.96	m ³
Wetted surface	30.76	m ²
Mass Buoy	3000	kg
Draft	0.37	m

Table 7.1: Parameters of mesh geometry

In order to perform calculations using a rigid body, it's necessary to know how mass is distributed in three dimensions. The inertia tensor for this buoy at its center of gravity, expressed in units of kg m², is provided below:

$$\begin{bmatrix} 4806 & 0 & 0 \\ 0 & 4806 & 0 \\ 0 & 0 & 9120 \end{bmatrix}$$

7.3. Boundary Element Method and Capytaine

Unfortunately, it is not possible to solve the boundary value problem analytically, only for very simple geometries. Instead numerical methods are used to solve these problems using the Green's function. According to the Green's theorem, the velocity potential ϕ at any point on the body wetted surface can be represented by distributions of singularities; sources or dipoles. Essentially, a source is a point from which fluid is thought to flow radially outwards whereas a sink is thought to flow inwards. A dipole is seen as the combination of a source-sink pair. This establishes the fundamental basis of the boundary element method for fluid-structure interactions. By applying this theorem, a three-dimensional linear potential flow problem can be transformed into a two-dimensional linear flow problem using the Boundary Integral Equation (BIE) at the body's surface. This integral equation must then be solved for the unknown source strength or dipole moment. To do so, the Green's function $G(\vec{x}, \vec{x}_s)$ is introduced and the radiated or diffracted velocity potential can be calculated by [64]:

$$\hat{\phi}(\vec{x}) = \frac{1}{4\pi} \int_{S_b} G(\vec{x}, \vec{x}_s) \sigma(\vec{x}_s) dS \quad (7.2)$$

where,

- \vec{x} is the source location on the body surface
- $\hat{\phi}$ is the complex amplitude of the velocity potential at \vec{x}
- $G(\vec{x}, \vec{x}_s)$ is the Greens function representing the flow at that location due to a source of unit strength at \vec{x}_s
- $\sigma(\vec{x}_s)$ represents the source strength at \vec{x}_s
- S_b is the mean wetted hull surface

The Green function satisfies both the linearised free surface and the impermeable seabed boundary conditions except for the impermeable hull condition. Substituting this boundary condition from equation 5.9 into equation 7.2 leads to equation 7.3 which is used in order to solve the source strengths σ .

$$-\frac{1}{2}\sigma(\vec{x}_s) + \frac{1}{4\pi} \int_{S_b} \frac{\partial G(\vec{x}, \vec{x}_s)}{\partial n_{\vec{x}}} \sigma(\vec{x}_s) dS = \hat{V}_n(\vec{x}) \quad (7.3)$$

Once the source strengths $\{\sigma\}$ have been calculated the next step is to determine the velocity potentials $\{\Phi\}$. In order to use the Green's function numerically and apply it to a mesh, these equations are discretised using a collocation method. The hull surface contains panels denoted with k . The centre of a panel in the mesh is known as the collocation point. In order to visualise this, a mesh of 312 panels was created showing these points and the normal vectors for each panel in Figure 7.4. In equations 7.4 and 7.5 the collocation point is given as \vec{x}_j for a panel with a surface S_k . The degree of freedom is given by j and the Kronecker delta function denoted by δ_{jk} equals 1 for $j = k$ and 0 otherwise.

$$S_{BEM,jk} = \frac{1}{4\pi} \int_{S_k} \partial G(\vec{x}_j, \vec{x}_s) dS \quad (7.4)$$

$$K_{BEM,jk} = -\frac{\delta_{jk}}{2} + \int_{S_k} \frac{\partial G(\vec{x}_j, \vec{x}_s)}{\partial n_{\vec{x}_j}} dS \quad (7.5)$$

Equations 7.4 and 7.5 form a matrix \mathbf{S}_{BEM} and \mathbf{K}_{BEM} , also known as the influence matrices, for each rigid-body degree of freedom j and represent the interaction between two faces of the mesh [60]. It relates the potentials $\{\Phi\}$, the normal velocities $\{u\}$ and the source distributions $\{\sigma\}$ through the following equations:

$$\begin{aligned} \{\Phi\} &= \mathbf{S}_{BEM} \{\sigma\} \\ \{u\} &= \mathbf{K}_{BEM} \{\sigma\} \end{aligned} \quad (7.6)$$

7.4. Running WEC-Sim

As soon as the pre-processing is done, which consists of creating the WEC geometry and computing the hydrodynamic coefficients using the BEM solver, the hydrodata file can be created. This requires the user to run BEMIO which is a built in function of WEC Sim [49]. The next step is to build the actual WEC-Sim Simulink model using the corresponding WEC-Sim Library. In this case the model consists of a rigid body block which represents the buoy itself, a non-hydrodynamic body block which represents the translator inside the generator, a constraint and a PTO block. The constraint block is used to connect bodies to one another. In this case a fixed constraint is used and constrains all motion between the translator and the buoy in order to simplify the model for the simulations. The PTO block represents the power take-off system and consists of a damper and a stiffness. The stiffness is set to zero and the damping is tuned to maximise the power capture.

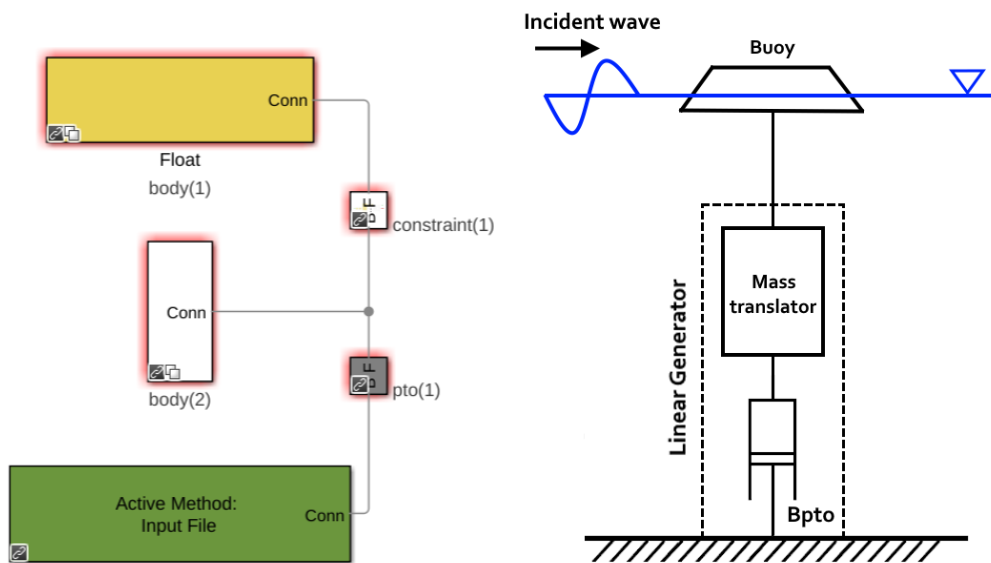


Figure 7.6: Block diagram of the simulink model (Left) and a schematic representation of the WEC system (Right)

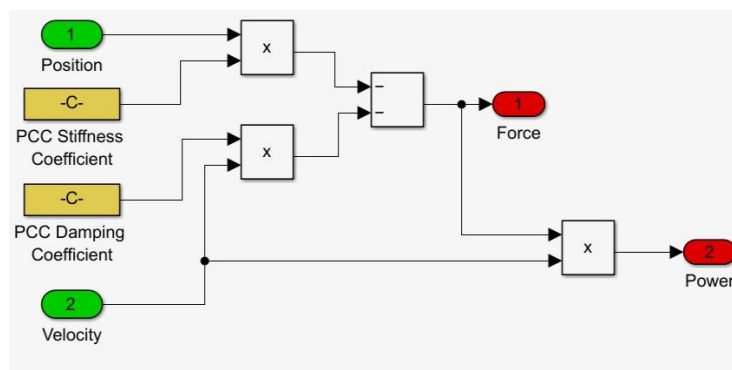


Figure 7.7: Internal mechanics of the PTO

The PTO force is the force the PTO applies to the body and is calculated for every time step as a function of the position and velocity of the buoy in motion. The total PTO force is obtained by multiplying the velocity with the PTO damping coefficient and the position with the PTO stiffness coefficient and adding these two terms. Furthermore, the instantaneous power of the PTO is obtained by multiplying this force by the velocity.

7.4.1. Multiple Condition Run

Calculating the mean power for a particular sea state can be done fairly easily in WEC-Sim. Based on a 30 minute simulation of the power output, the mean power is obtained. Figure 7.8 shows the mean power output using the WEC in this study for the most occurring sea state in this region which is $H_s = 0.5m$ and $T_p = 4s$ and occurs 18.5% of the time (as seen in figure 6.17).

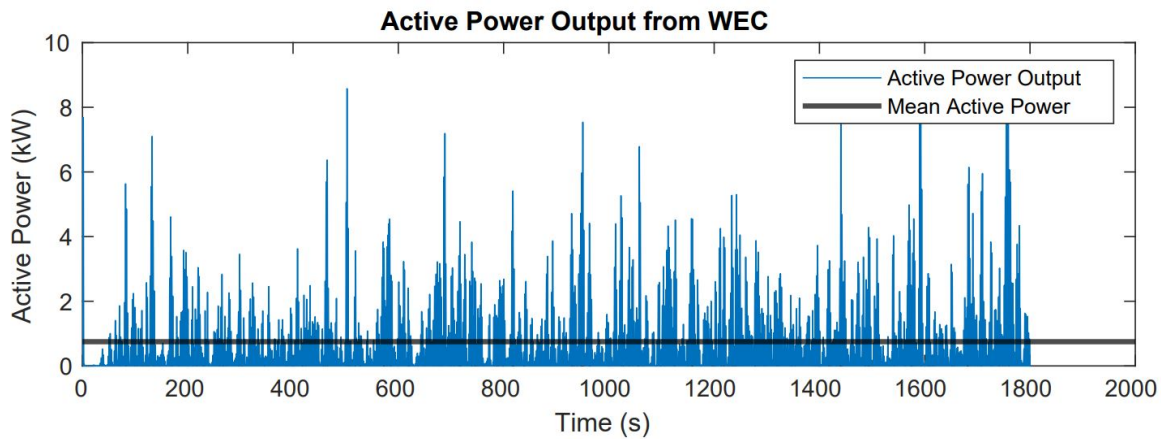


Figure 7.8: Active power output in kW for the most common occurring sea state $H_s = 0.5m$ and $T_p = 4s$ giving a mean active power of 0.75 kW. It uses a simulation time of 30 minutes.

However, to generate a power matrix, this process must be repeated for multiple sea states, which can become a tedious task when performed consecutively. WEC-Sim has the ability to perform batch runs which enables different cases to be run in succession. This is initiated by entering "wecSimMCR" into the MATLAB Command Window and can be used to simulate the behaviour of the WEC for different sea states wave heights and wave periods. First the "wecSimInputFile.m" is created which includes all the relevant parameters, such as the type of wave spectrum, the PTO parameters and the WEC hydrodynamic properties. The code and parameters used in this simulation can be seen in appendix C. Secondly, a "userDefinedFunctionsMCR.m" script is made that defines the outputs of the batch runs. After the batch runs, the PTO power for each of these simulated sea states are stored in "output.ptos.powerInternalMechanics" data file, which is the data used to generate the power matrix.

7.5. Verification

To verify the model a grid convergence study is performed in section 7.5.1 and the hydrodynamic coefficients obtained in Capytaine are compared to that of NEMOH in section 7.5.2.

7.5.1. Convergence Analysis & Computational Effort

Computations were done on a Lenovo windows PC using an Intel(R) Core(TM) i5-7400 CPU @ 3.00GHz processor and 8.00 GB RAM memory. The simulation times using different mesh sizes were recorded and included in table 7.2. Grid convergence analysis was tested in Capytaine by refining the mesh resolution for the added mass coefficients, the radiation damping coefficients and RAOs in heave motion, as can be seen in figures 7.9, 7.10 and 7.11. The number of frequencies used for these simulations is 108 with a minimum frequency of 0.05 and a maximum of 5.45 rad s⁻¹. These figures only show frequencies up to 4.0 rad s⁻¹, which makes deviations between the meshes easier to see. For higher frequencies, the lower mesh resolutions start deviating much more.

<i>Mesh resolution</i>	<i>Run Time [sec]</i>
106	140.14
570	148.00
1138	164.28
1308	172.60
2004	225.95

Table 7.2: Computational effort for different mesh resolutions

As is evident from figures 7.9, 7.10 and 7.11 the different mesh sizes quickly converge towards the highest panel resolution of 2004. This proves that the panel resolution of 1308 used in section 7.2 is sufficient enough to provide a high accuracy of the results.

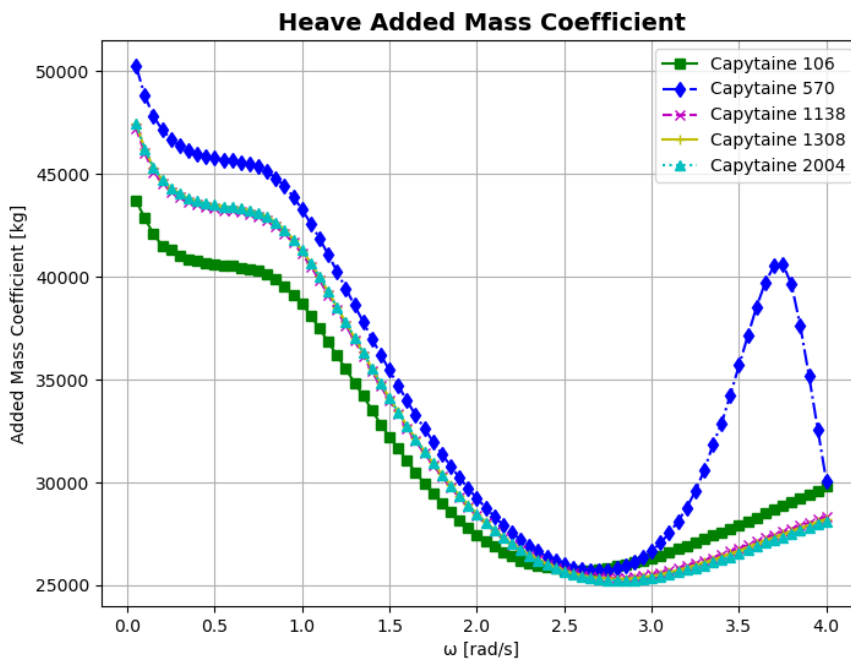


Figure 7.9: Convergence analysis for added mass coefficient in heave

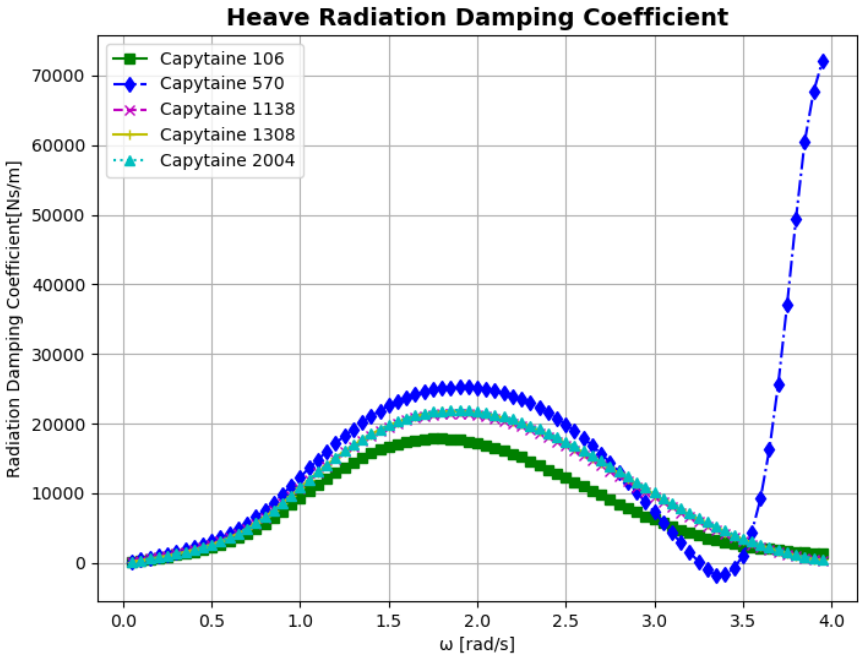


Figure 7.10: Convergence analysis for radiation damping coefficient in heave

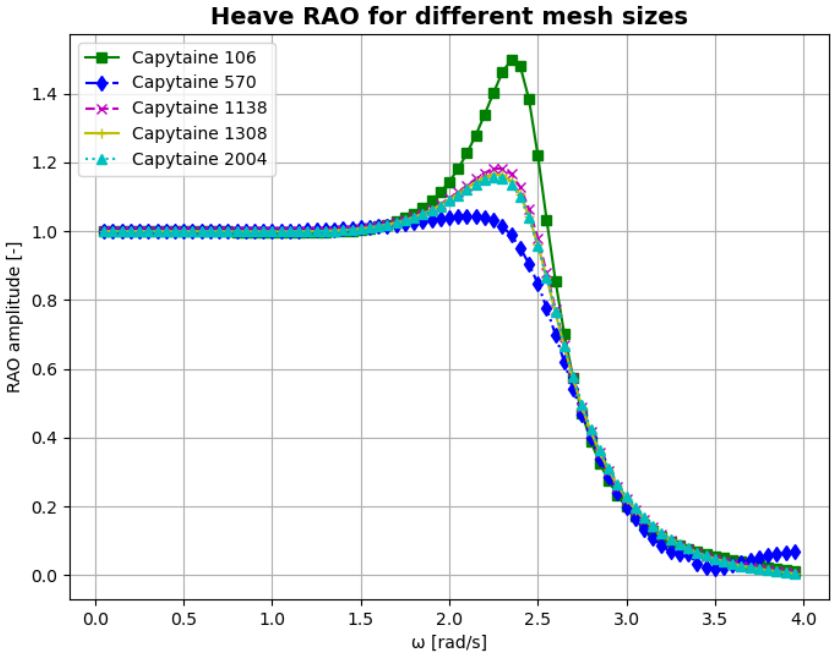
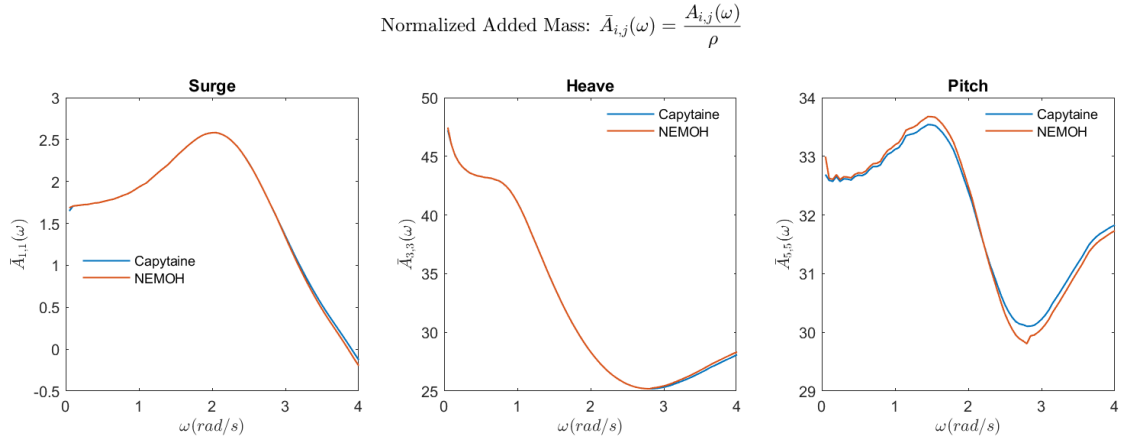


Figure 7.11: Convergence analysis for RAOs in heave

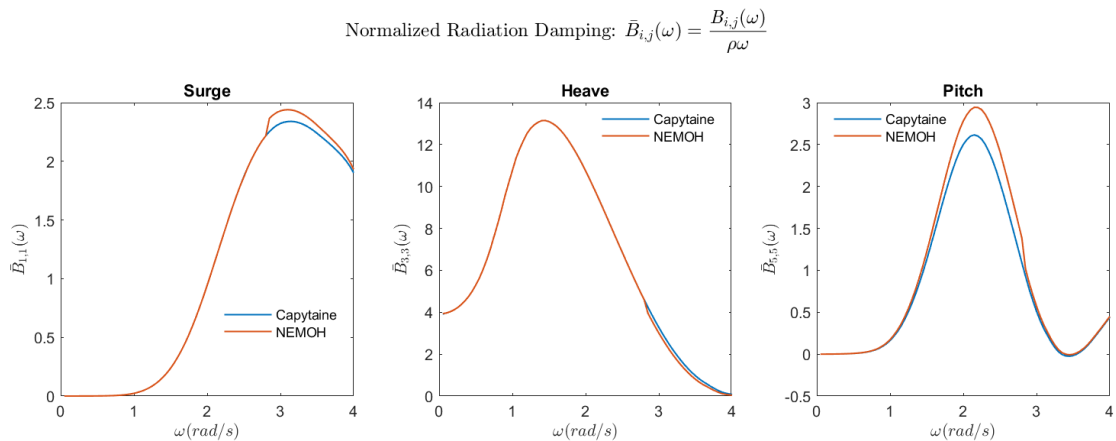
7.5.2. Comparison of BEM Solvers

The hydrodynamic coefficients obtained from Capytaine can be validated against another BEM solver. Since Capytaine's code is built upon the foundations of Nemoh, it would be interesting to compare the two BEM solvers with each other. The same mesh of 1308 panels and 656 nodes was simulated using both Capytaine and Nemoh and plotted added mass, radiation damping, excitation force and RAOs for surge, heave and pitch motion. The range of frequencies used were 0 to 4 rad s⁻¹. This is more than enough since the highest frequency recorded in this region is 3.43 rad s⁻¹. Even though some deviations can be seen for the two examples, they seem to agree fairly well especially in their response amplitude operators.



Notes:

- $\bar{A}_{i,j}(\omega)$ should tend towards a constant, A_{∞} , within the specified ω range.
- Only $\bar{A}_{i,j}(\omega)$ for the surge, heave, and pitch DOFs are plotted here. If another DOF is significant to the system, that $\bar{A}_{i,j}(\omega)$ should also be plotted and verified before proceeding.



Notes:

- $\bar{B}_{i,j}(\omega)$ should tend towards zero within the specified ω range.
- Only $\bar{B}_{i,j}(\omega)$ for the surge, heave, and pitch DOFs are plotted here. If another DOF is significant to the system that $\bar{B}_{i,j}(\omega)$ should also be plotted and verified before proceeding.

Figure 7.12: Added mass and radiation damping coefficient comparison for Nemoh and Capytaine

$$\text{Normalized Excitation Force Magnitude: } \bar{X}_i(\omega, \theta) = \frac{X_i(\omega, \theta)}{\rho g}$$

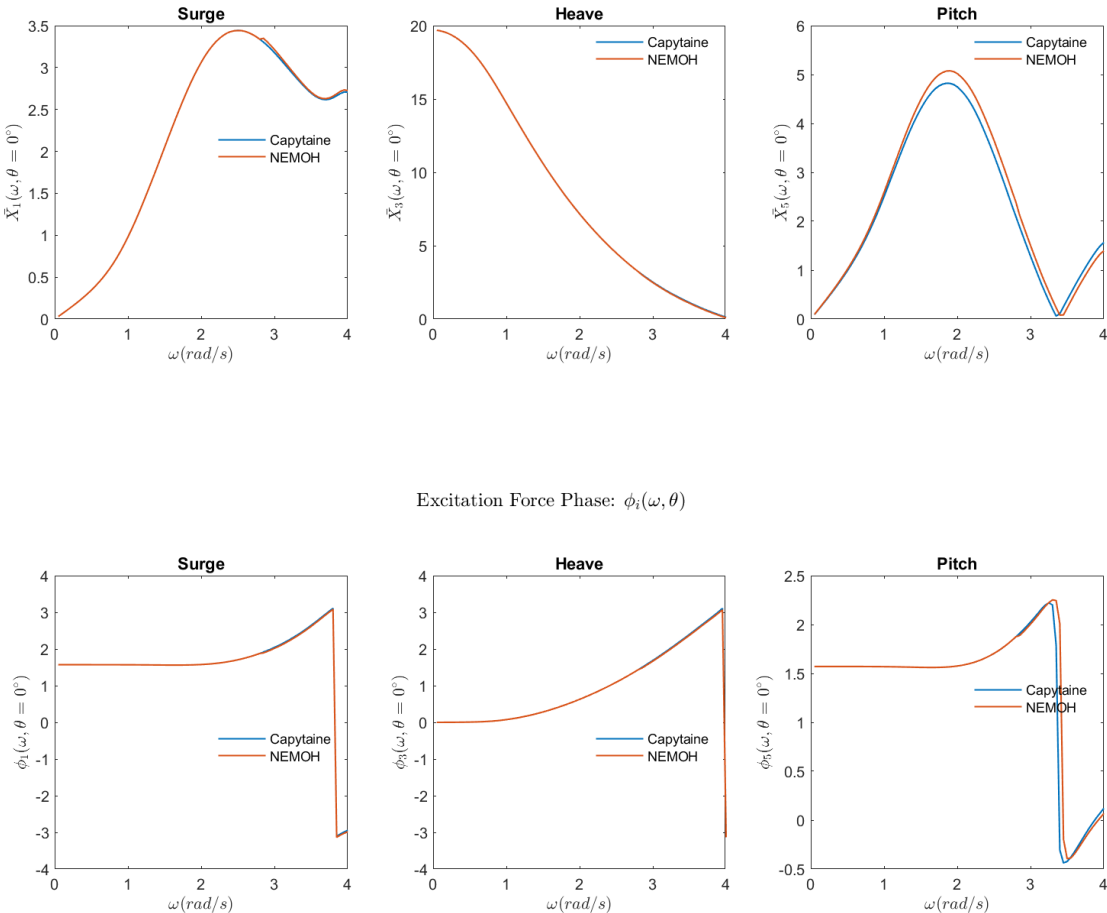


Figure 7.13: Excitation magnitude and phase comparison for Nemoh and Capytaine

$$\text{Normalized Excitation Force Magnitude: } \bar{X}_i(\omega, \theta) = \frac{X_i(\omega, \theta)}{\rho g}$$

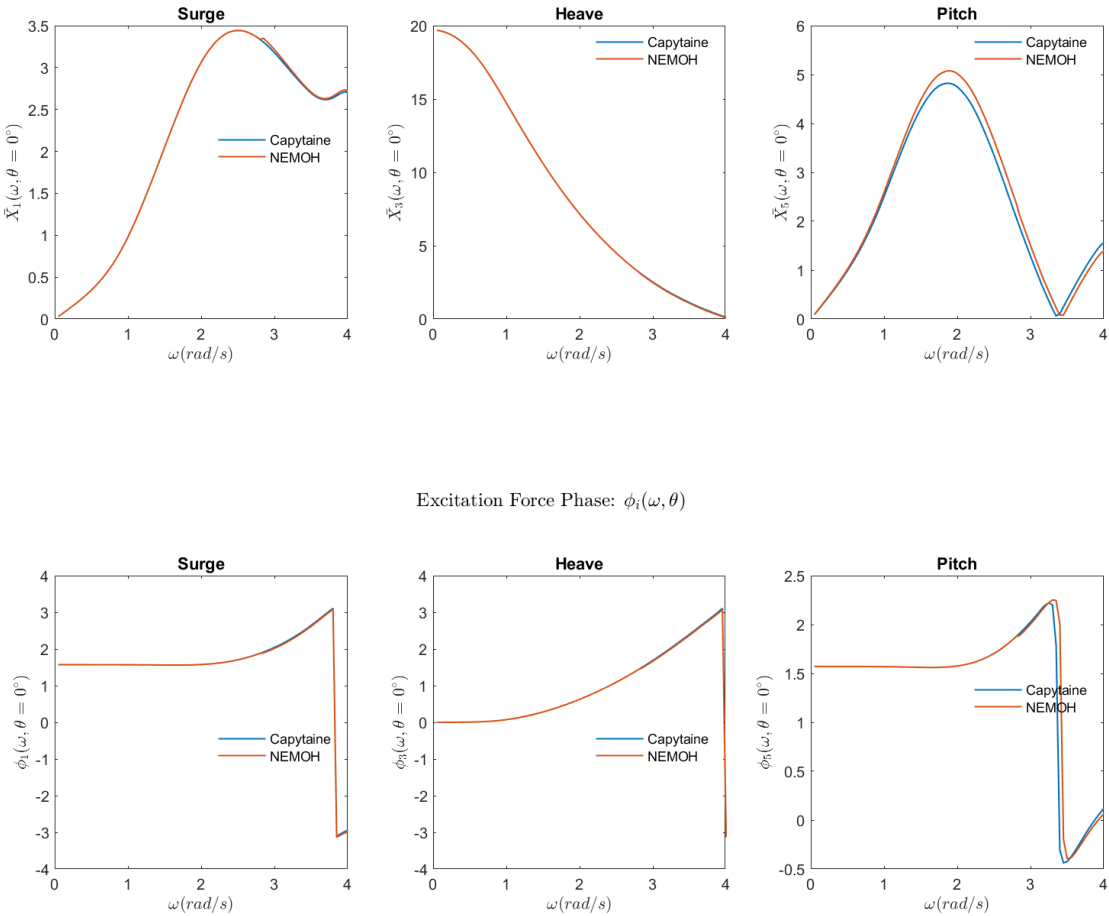
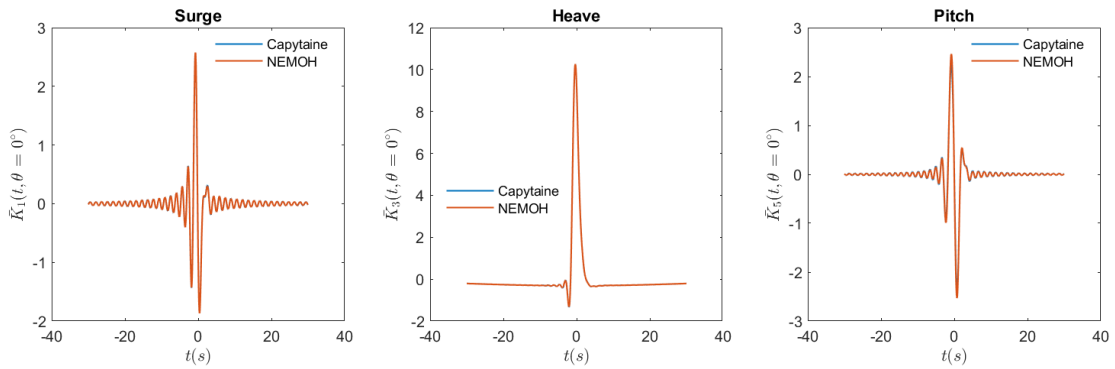


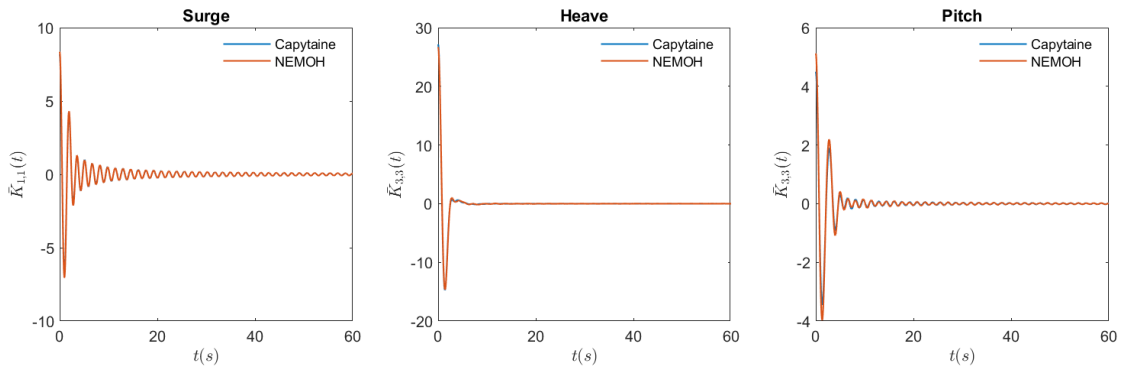
Figure 7.14: Excitation force magnitude and phase comparison for Nemoh and Capytaine

$$\text{Normalized Excitation Impulse Response Functions: } \bar{K}_i(t) = \frac{1}{2\pi} \int_{-\infty}^{\infty} \frac{X_i(\omega, \theta) e^{i\omega t}}{\rho g} d\omega$$



- Notes:
- The IRF should tend towards zero within the specified timeframe. If it does not, attempt to correct this by adjusting the ω and t range and/or step size used in the IRF calculation.
 - Only the IRFs for the first wave heading, surge, heave, and pitch DOFs are plotted here. If another wave heading or DOF is significant to the system, that IRF should also be plotted and verified before proceeding.

$$\text{Normalized Radiation Impulse Response Functions: } \bar{K}_{i,j}(t) = \frac{2}{\pi} \int_0^{\infty} \frac{B_{i,j}(\omega)}{\rho} \cos(\omega t) d\omega$$



- Notes:
- The IRF should tend towards zero within the specified timeframe. If it does not, attempt to correct this by adjusting the ω and t range and/or step size used in the IRF calculation.
 - Only the IRFs for the surge, heave, and pitch DOFs are plotted here. If another DOF is significant to the system, that IRF should also be plotted and verified before proceeding.

Figure 7.15: Excitation force and radiation damping impulse response functions comparison for Nemoh and Capytaine

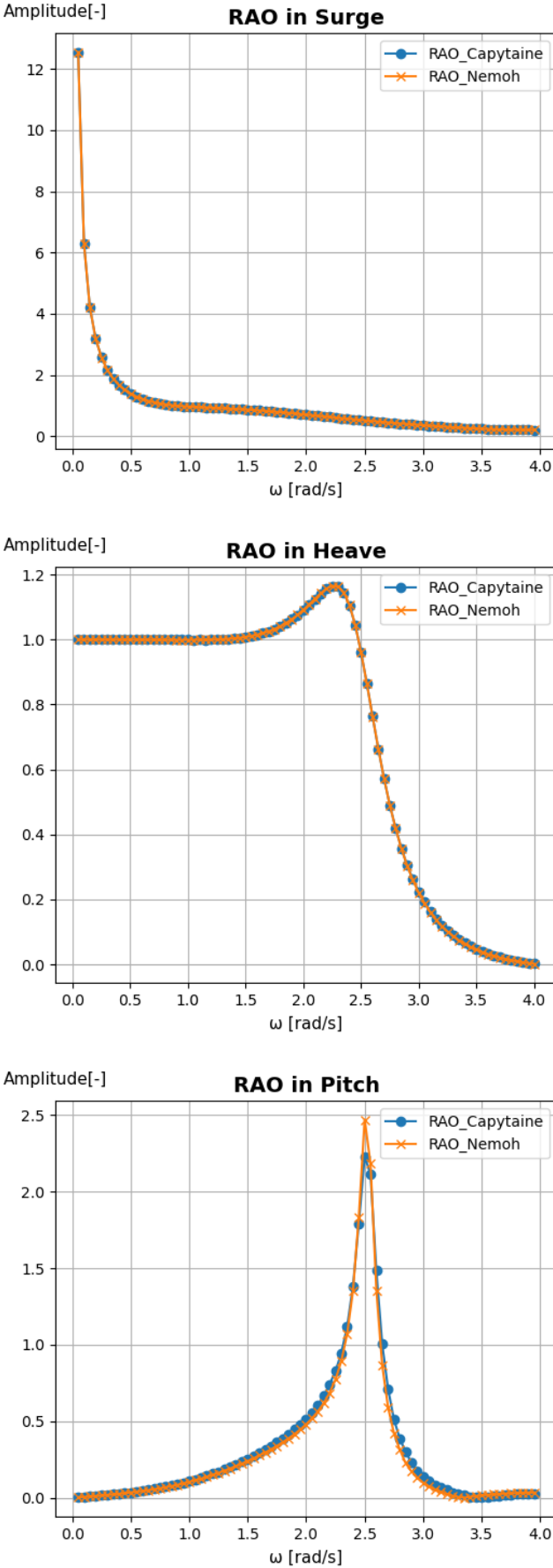
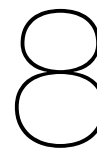


Figure 7.16: Response amplitude operator comparison for Nemoh and Capytaine

Part IV

Results



Results and Discussion

This chapter discusses the results from the numerical modelling and the calculated design ice actions. The first section is dedicated to the first research question on WEC survivability. The subsequent sections focus on energy production, seasonal variability and the economics. The power matrices for varying Power Take-Off (PTO) damping and varying translator sizes are given and the seasonal variability of power output is analysed. Using an economical model the levelised cost of energy (LCOE) is also calculated.

8.1. WEC Survivability

The Baltic Sea poses a difficult challenge to the survivability of offshore structures, particularly with storms, extreme wave conditions and the presence of seasonal ice. According to [65], survivability is defined as "a measure of the ability of a subsystem or device to experience an event ('survival event') outside the expected design conditions, and not sustain damage or loss of functionality beyond an acceptable level, allowing a return to an acceptable level of operation after the event has passed." In this section, an analysis into a point absorber WEC navigating its dynamic wave climate and seasonal ice cover is performed. Starting off, the force on the WEC in extreme sea states is simulated and analysed using the design load cases from section 6.4.2. Thereafter, the design ice actions is calculated using the equations from section 4.4. The environmental design load cases found in section 6.4.2 need to be analysed. Three simulations are run in WEC-Sim using irregular waves based on the JONSWAP spectrum. A wave ramp time is set at 100 seconds to reduce strong transient oscillations due to shock wave loads. The simulation time is set to 400 seconds with a timestep of 0.1 seconds. To account for non-linearity's, viscous damping is added to the system. An assumption is made for the quadratic drag coefficient of 0.7 based on data from the WaveBob point absorber in literature [66].

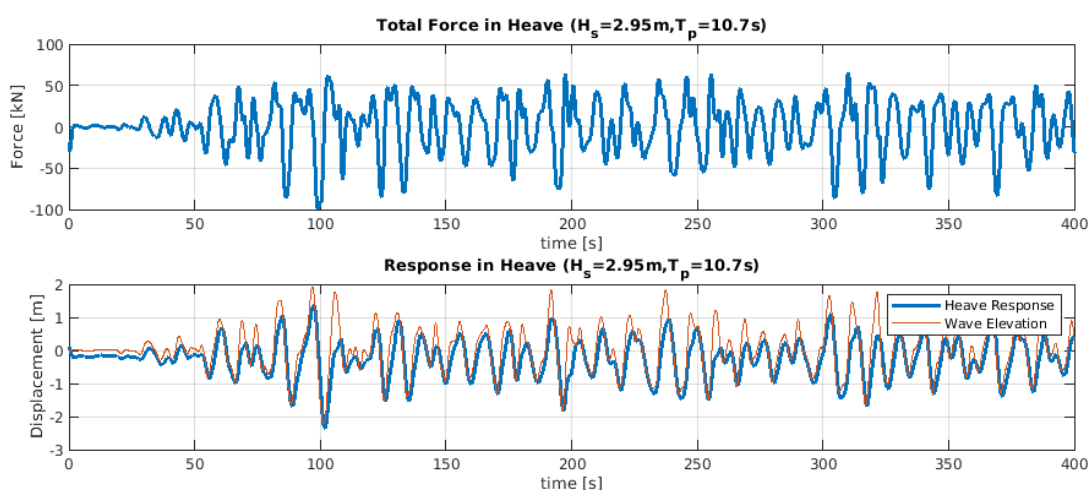


Figure 8.1: Simulated force and response in irregular waves from design load case 1

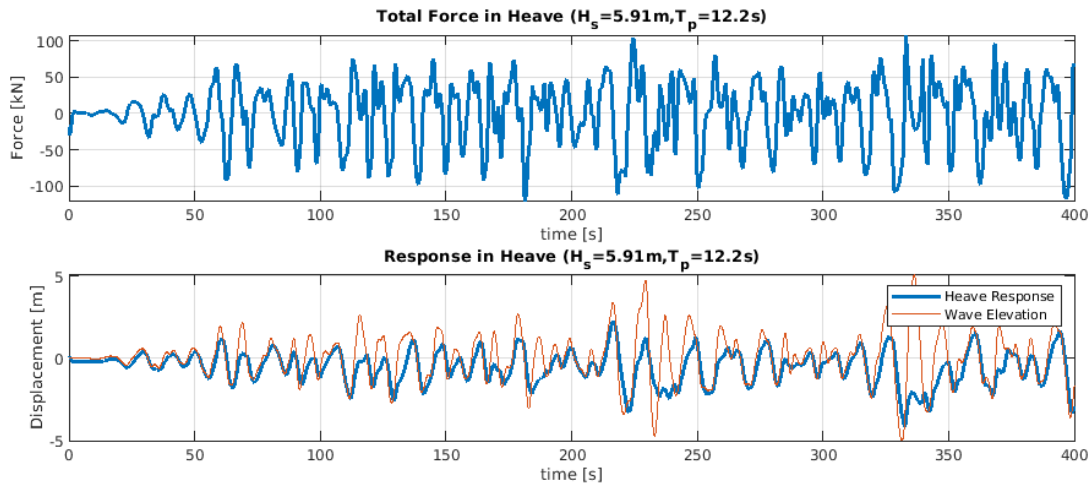


Figure 8.2: Simulated force and response in irregular waves from design load case 2

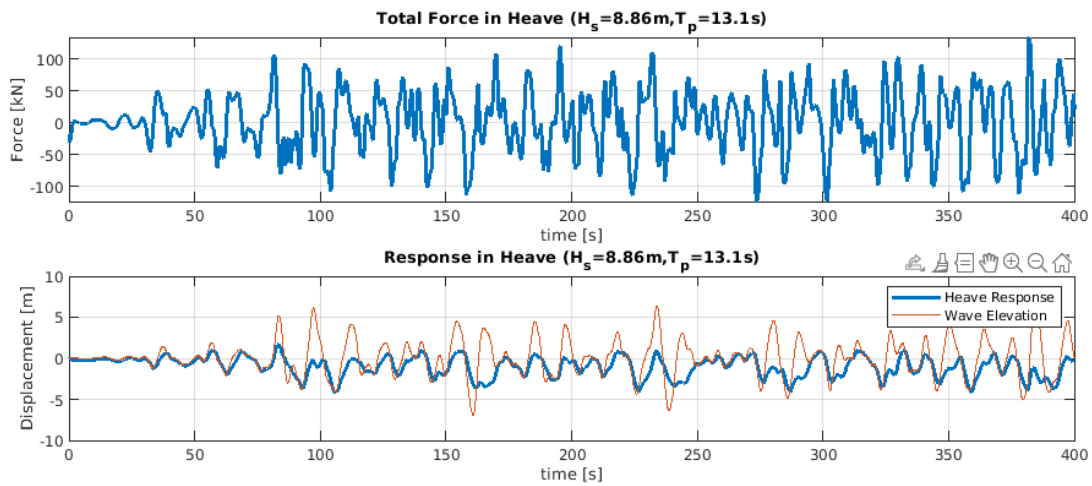


Figure 8.3: Simulated force and response in irregular waves from design load case 3

Table 8.1 summarises the results from the simulations. As can be observed, the heave force reaches a maximum value of 133 kN and the maximum displacement is 4.16 m.

Design Load Case	Hs (m)	Tp (s)	Maximum Force (kN)	Maximum Response (m)
1.	2.95	10.7	98.68	2.36
2.	5.91	12.2	119.95	4.12
3.	8.86	13.1	133.60	4.16

Table 8.1: Maximum heave force and response from the simulated design load cases

Given the parameters used in the case study from section 3.1 and the geometry of the WEC given in section 7.2, it is possible to estimate the design ice actions on the slope shaped buoy. Table 8.2 shows the parameters used for the ice bending calculations. The numbers used here are taken from the ISO19906 arctic design standard [38] with a focus on the Baltic Sea region and the structure geometry of the WEC. This makes it possible to plot the horizontal and vertical ice actions as a function of the extreme ice thickness as can be seen in figure 8.4.

Parameter	Symbol	Value	Unit
Density of ice	ρ_i	907	kg/m ³
Ice-to-ice friction coefficient	μ_i	0.08	-
Ice to structure coefficient	μ	0.06	-
Rubble height	h_r	2.5	m
Slope angle	α	60	°
Ice rubble angle	θ	50	°
Porosity of ice rubble	e	0.35	-
Cohesion of ice rubble	c	1.6×10^3	Pa
Friction angle of ice rubble	ϕ	40°	-
Waterline width	w	5.51	m
Top width	w_T	4.67	m
Modulus elasticity of ice	E	5×10^9	Pa
Water density	ρ_w	1005	kg/m ³
Flexural strength	σ_f	0.57×10^6	Pa
Poisson's ratio	ν	0.3	-

Table 8.2: Parameters used in ice bending calculations [38][46]

Figure 8.4 shows an exponential increase in the vertical and the horizontal ice action forces for an increasing ice thickness. As previously estimated in section 6.2, the extreme ice thickness with a 50 year return period is about 60 centimetres. This would result in an estimated horizontal force of 615kN and a vertical force of 315kN. Due to the mass and the volume of the hexagonal buoy, the maximum buoyancy force when fully submerged is 183kN. This means that the force needed to push the WEC under the ice is 134kN, which can occur with an extreme ice thickness of at least 38 centimetres or more. It is important to note that the calculations for the design ice load takes into account rubble pile up on the slope of the structure but not on top. One could expect an increase in the total ice load and therefore this might result in an underestimation and explains why many offshore structures have a vertical section at the top of the slope that turns the ice block back down again.

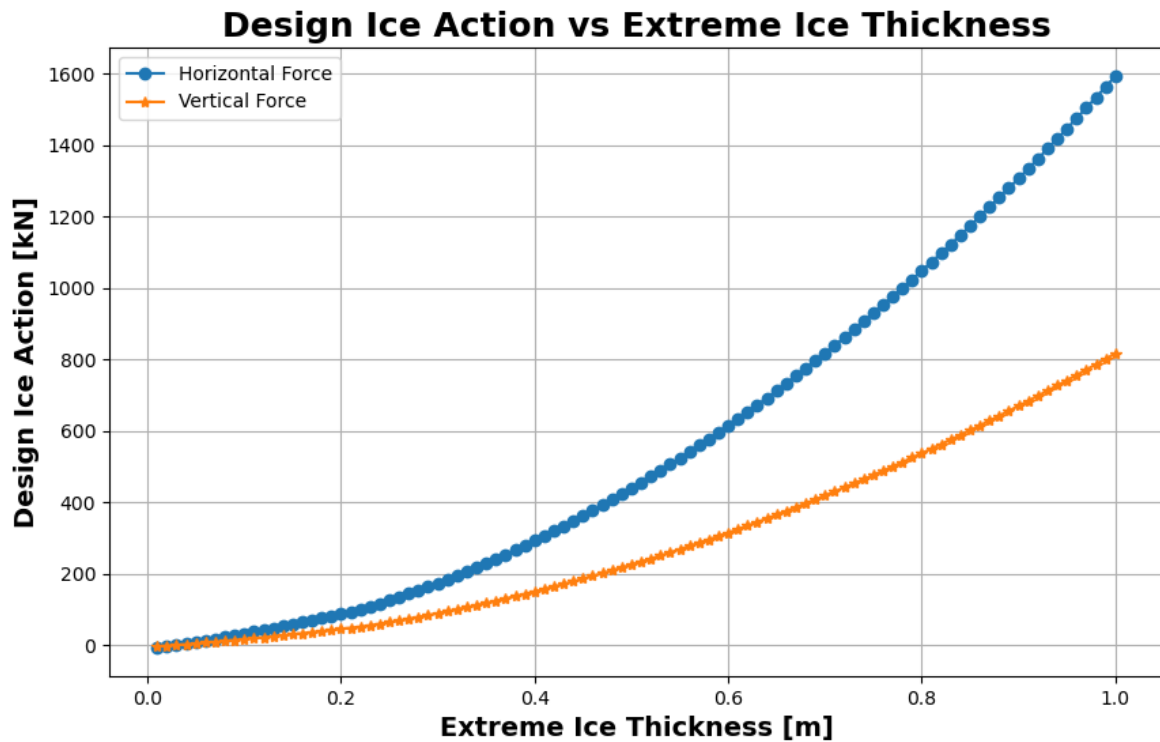


Figure 8.4: Design ice action forces plotted against extreme ice thickness

8.1.1. Discussion

The primary scope of this research is on assessing the impact of sea ice on the overall power production of the WEC, rather than an extensive examination of how extreme level ice load affects the behaviour of the WEC. This is why a rather simplistic calculation for the design ice actions are made instead of simulated using a numerical model. These calculations are based on simple first-order beam theory. While this provides a reasonable estimation for two-dimensional problems it would also be possible to use more complex plate theory for three-dimensional problems. The method for bending failure used in ISO19906 [38] assumes that the length of the crack is equal to the width of the structure. In three-dimensional problems however, radial crack patterns can often be seen where the length of the crack is greater than the width of the structure.

Another aspect to consider is the time-varying nature of the ice interaction process. Dynamic ice interaction processes can lead to ice-induced vibrations that have significant impact on the force and the behaviour of the structure. Paying attention to the specific frequencies of ice interaction processes could be crucial for design, as the structure may need to avoid unfavourable natural frequencies that coincide with the ice-interaction. On top of this, even smaller ice actions can lead to fatigue failure. The combined effects of cyclic waves and ice actions throughout its lifespan can profoundly affect the structural integrity and should therefore be taken into account.

As discussed in section 4.5, other ice features such as ice ridges would subject the buoy to harsh treatment. Although exactly how the buoy would behave in such a scenario remains speculative. Prior to an interaction with an ice ridge it is assumed that the buoy will already have been submerged through interactions with thinner ice sheets and continues to slide around/under it. One method of avoiding an ice ridge would be to actively submerge the buoy prior to the ice interaction. This would require the buoy to be mounted with a mechanical device that can adjust the length of the buoy line using sensors that can detect ice interference or by manually operating the system remotely. The other option would be by the means of passive submersion. This would require the design of a sturdier buoy with a thicker hull that can passively submerge under the ice throughout the interaction process. The latter presents a cheaper and simpler solution as there would be no need for extra parts [36, 38].

8.2. Mean Annual Energy Production

The mean annual energy production serves as a crucial metric for evaluating the overall performance and the economic viability of a WEC. This process involves assembling short term wave statistics into a long term wave scatter diagram as it provides a detailed representation of the variation of sea states over this extended period with its frequency and intensity. Simultaneously, a series of power output simulations are conducted based on the WEC parameters and a particular sea state represented by a JONSWAP spectrum. Based on these simulations a power matrix can be generated from the mean power values. The last step is to combine the power matrix with the data from the wave scatter diagram to calculate the mean annual energy production which involves multiplying the power output of each sea state by its probability of occurrence.

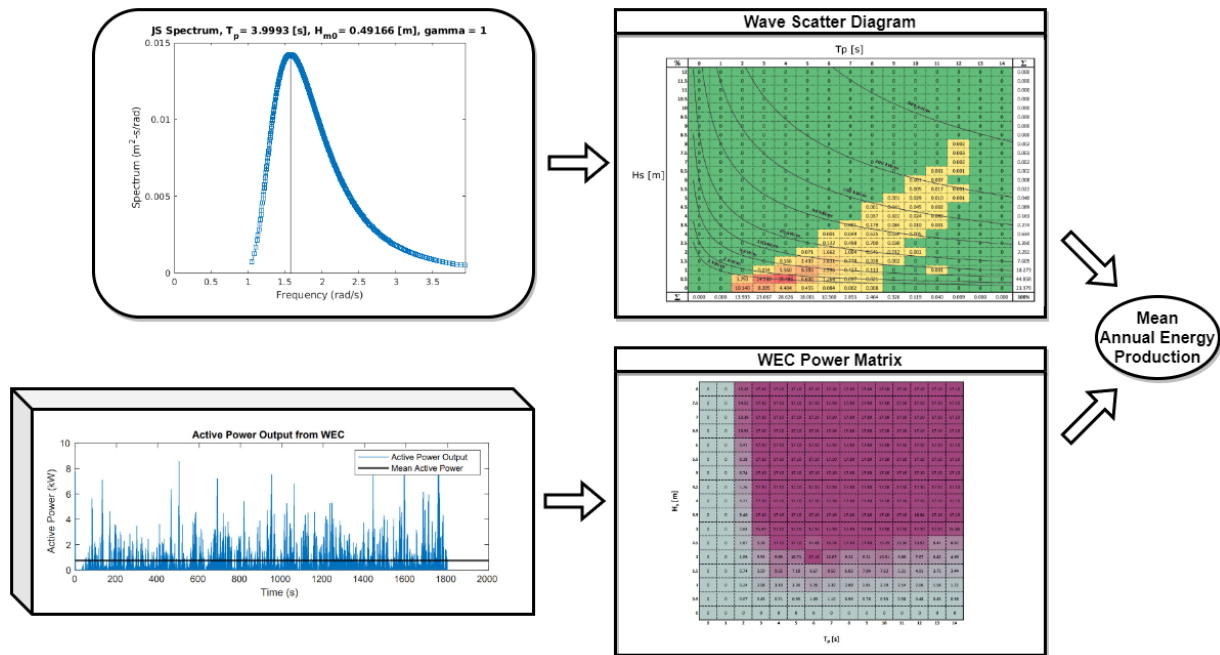


Figure 8.5: Flowchart for the mean annual energy production

8.3. Optimising power production

Optimising power production has been done by tuning the damping of the PTO in stages of 20 kN s m^{-1} starting from 40 kN s m^{-1} and ending at 160 kN s m^{-1} . The PTO damping resulting in the highest capacity factor can be systematically found using this method of trial and error. The other method used for optimising the power production is by changing the total mass of the system. As a result, its natural frequency would also be affected. By increasing the systems total mass, it's expected that its natural frequency in heave will decrease and move closer towards the most common peak frequency of 1.57 rad s^{-1} . As displayed in figure 8.6, three system configurations have been made by changing the translator of the linear generator. These modifications not only affects the systems total mass but also, the draft of the buoy, the centre of gravity, the centre of floatation, the natural frequency and the WECs power rating. These parameters are listed in table 8.3 below.

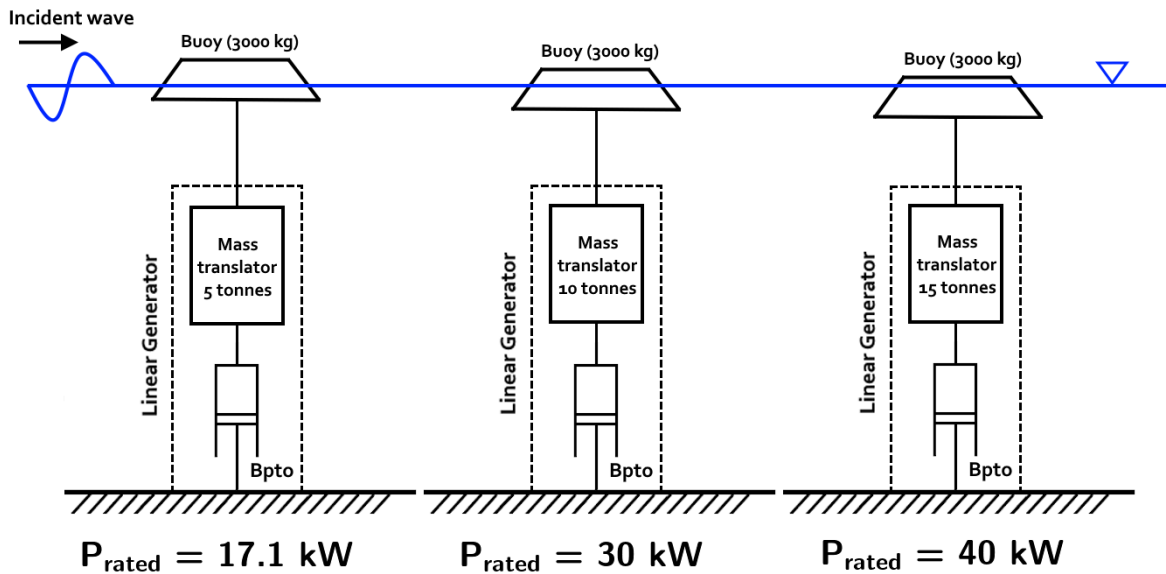


Figure 8.6: Three WEC configurations with changed translators

The power ratings used for these three configurations changes with heavier translator masses. The first configuration is assumed to have a 17.1kW rated power as this one is based on the point absorber used in project WESA and manufactured by Seabased AB [36]. A rated power of 30kW was chosen for the second configuration. This is based on the point absorber manufactured by Seabased AB that was deployed off the coast of Ghana that used a three phase nine-sided linear generator and featured a translator with a mass of 9.8 tonnes [67]. The third configurations power rating is extrapolated based on the translator mass and power ratings of the other two WECs. For this reason, a power rating of 40kW has been assumed for the third configuration in this study.

Parameter	1st configuration	2nd configuration	3rd configuration	Unit
Mass Translator	5000	10000	15000	kg
Total Displacement	8000	13000	18000	kg
Draft	0.37	0.64	0.96	m
Center of Gravity	[0 , 0 , 0.89]	[0 , 0 , -0.18]	[0 , 0 , -0.50]	m
Center of Floatation	[0 , 0 , -0.19]	[0 , 0 , -0.34]	[0 , 0 , -0.52]	m
Heave Natural Frequency	2.25	2.00	1.70	rad/s
Power Rating	17.1	30	40	kW

Table 8.3: List of parameters for the three WEC configurations

8.3.1. Response Amplitude Operators (RAOs) and Hydrostatic Stiffness

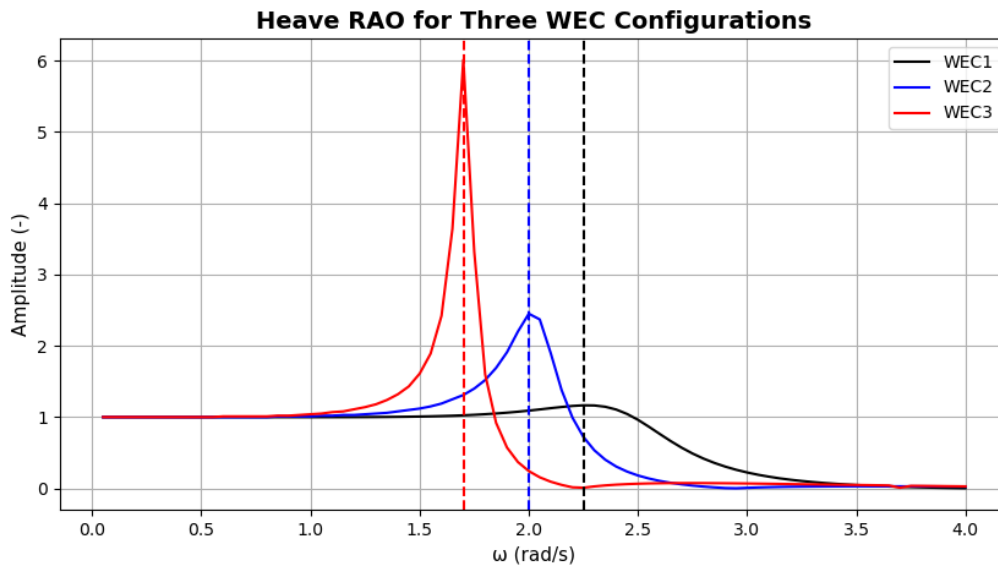


Figure 8.7: Heave RAOs for the three WEC configurations, the vertical lines depict their natural frequencies

The RAOs are computed using the hydrodynamic coefficients obtained from the boundary element method solver. As is observed in Figure 8.7, the RAOs show that the natural frequency for heave motion shifts towards lower frequencies for an increased total mass of the system. At lower frequencies, where the wavelength is large relative to the horizontal length of the structure, the vertical motions are dominated by the systems stiffness. On the other hand, around the systems natural frequency, the vertical motions are dominated by the systems damping. Therefore, the RAOs will change when tuning the PTO parameters, as an increase in the PTO damping will lead to less amplification and a flattening of the curves. The hydrostatic stiffness parameters for the three WEC configurations are shown below and is highest for the first configuration this is to be expected as this is a function of the waterplane area. A greater mass means a greater draft and the waterplane area decreases towards the top for this slope shaped buoy.

Hydrostatic Parameter	WEC 1	WEC 2	WEC 3	Unit
C33	1.98e5	1.73e5	1.46e5	N/m
C44	2.90e5	2.18e5	1.66e5	Nm/rad
C55	2.90e5	2.18e5	1.66e5	Nm/rad

Table 8.4: Non-zero hydrostatic stiffness parameters for the three WEC configurations

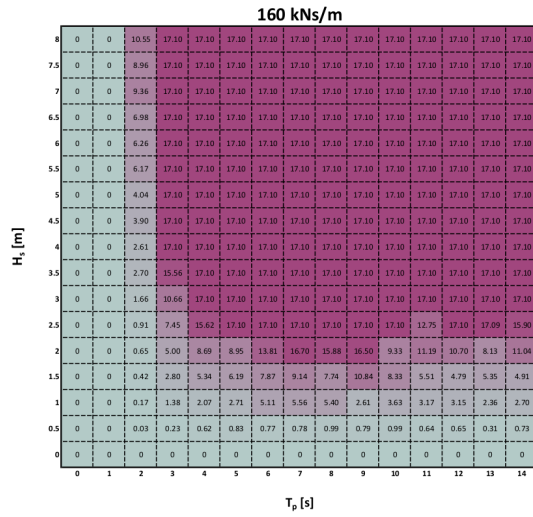
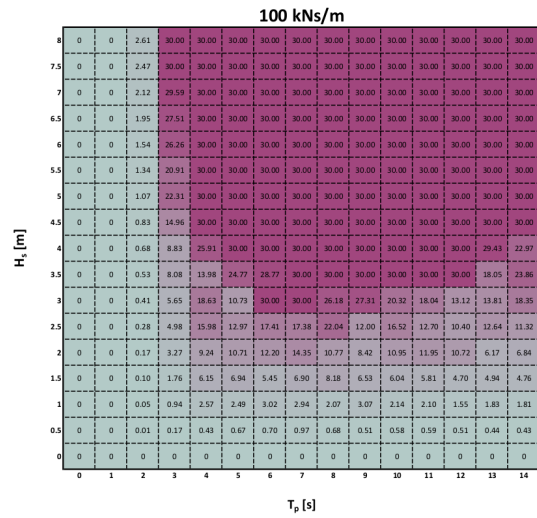
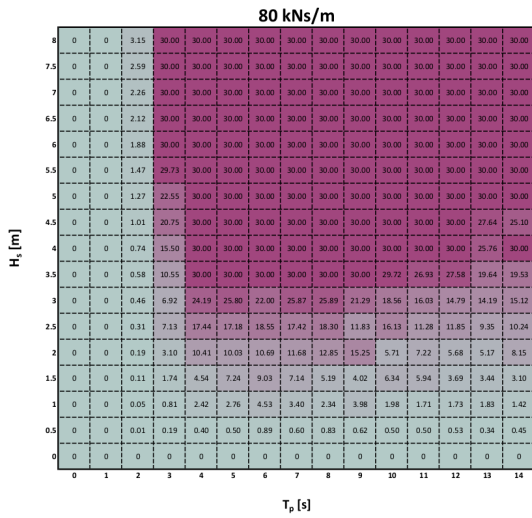
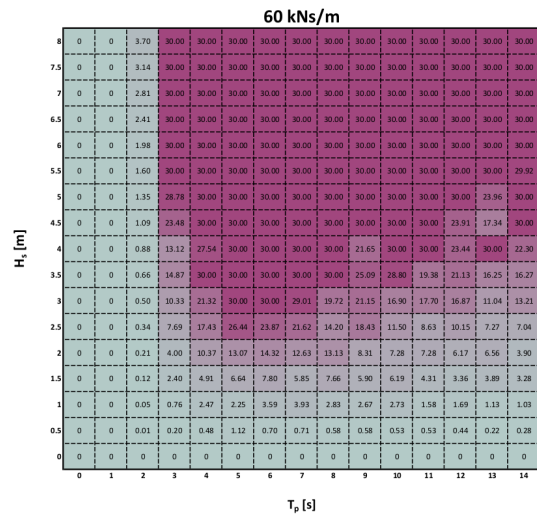
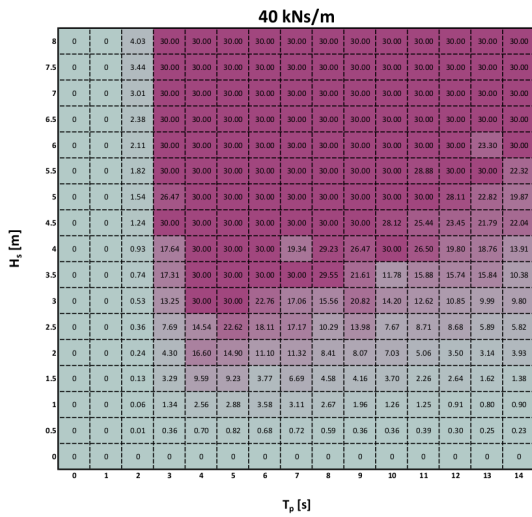


Figure 8.8: Power matrices for different PTO dampings (1st configuration: 17.1kW)

2nd WEC Configuration: 30kW



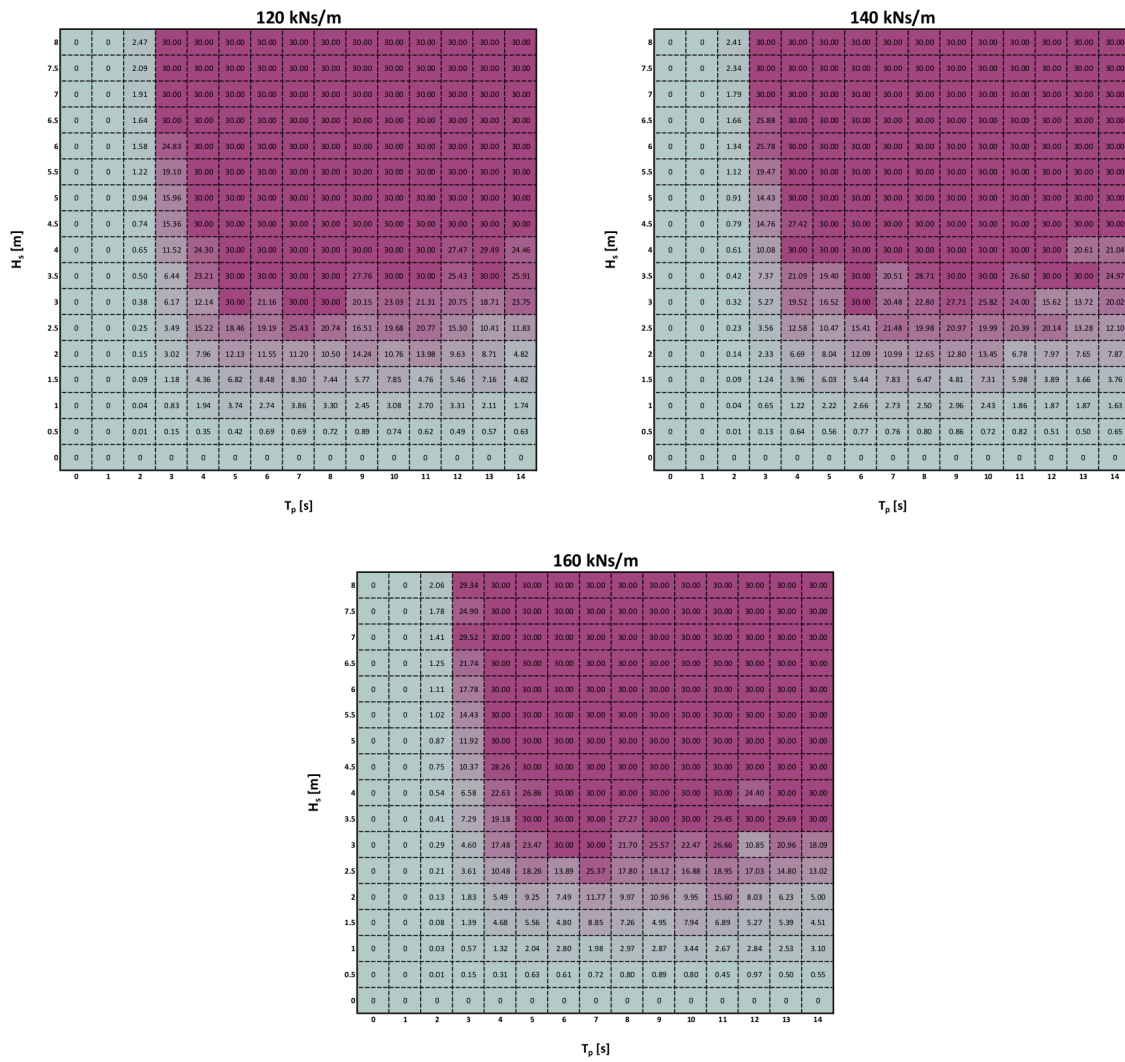
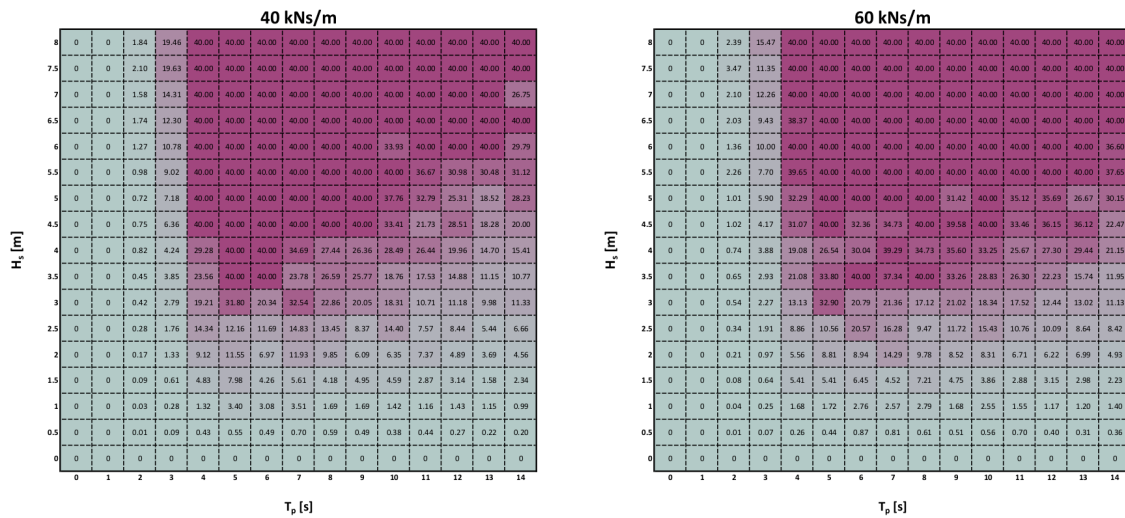


Figure 8.9: Power matrices for different PTO dampings (2nd configuration: 30kW)

3rd WEC Configuration: 40kW



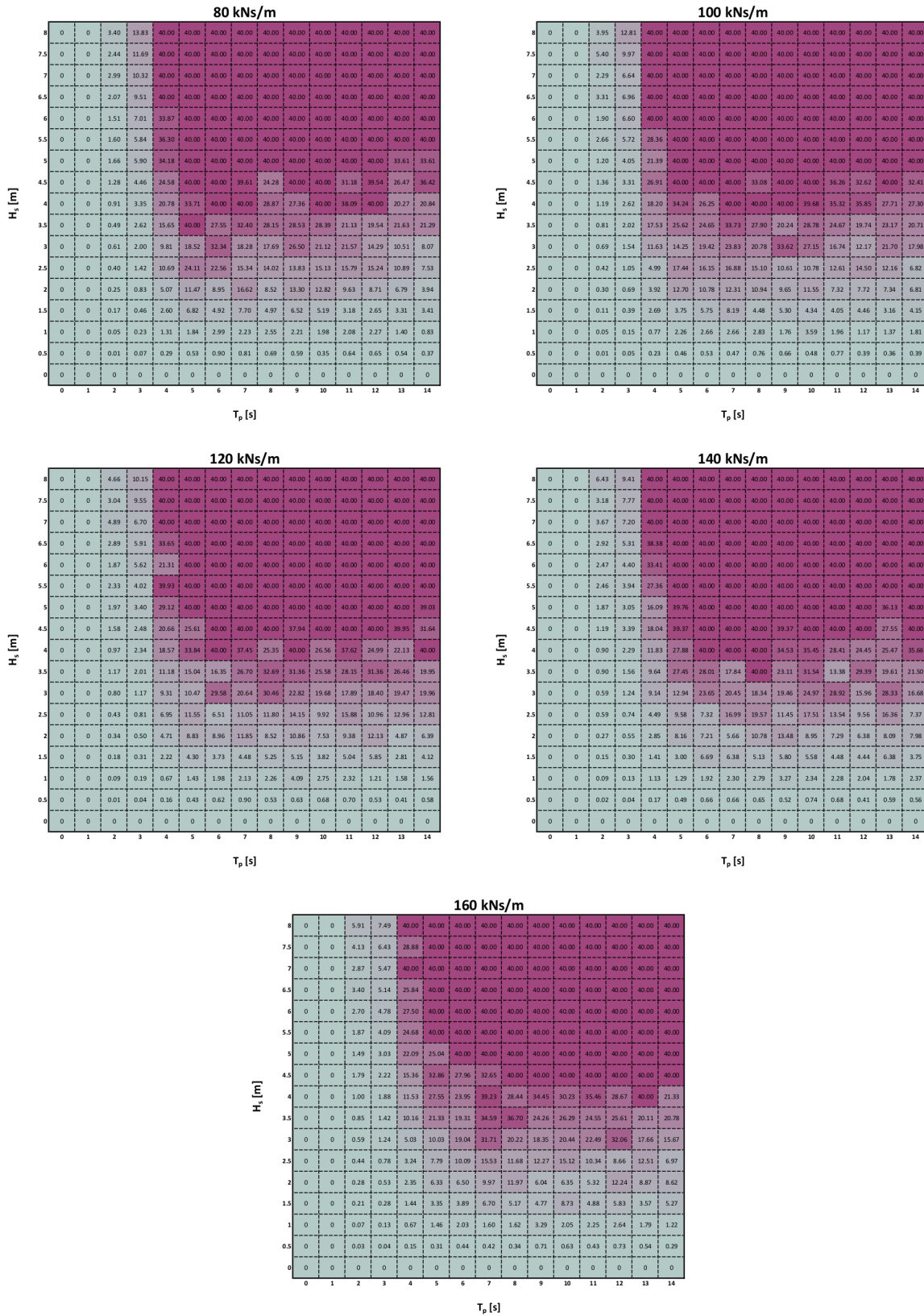


Figure 8.10: Power matrices for different PTO dampings (3rd configuration: 40kW)

8.3.3. Power Take-Off(PTO) Tuning

In contrast to situations involving regular waves, finding the optimal damping coefficient (B_{pto}) for a specific wave spectrum isn't straightforward. Instead, it's achieved indirectly by adjusting the level of power take-off (PTO) damping, denoted as B_{pto} [68]. The highest value of **AEP** corresponds to the ideal B_{pto} . The power matrices are capped to their power rating as this is the maximum power that that particular WEC is capable of generating. From the power matrix and the 15 year wave scatter diagram (Figure 6.17), the annual energy production **AEP** and their corresponding capacity factors **CF** have been calculated. The configurations and the PTO damping resulting in the highest energy yield and capacity factor is selected. This turned out to be the first WEC configuration and a PTO damping of 80 kN s m^{-1} . The comparisons can be seen in Figure 8.11.

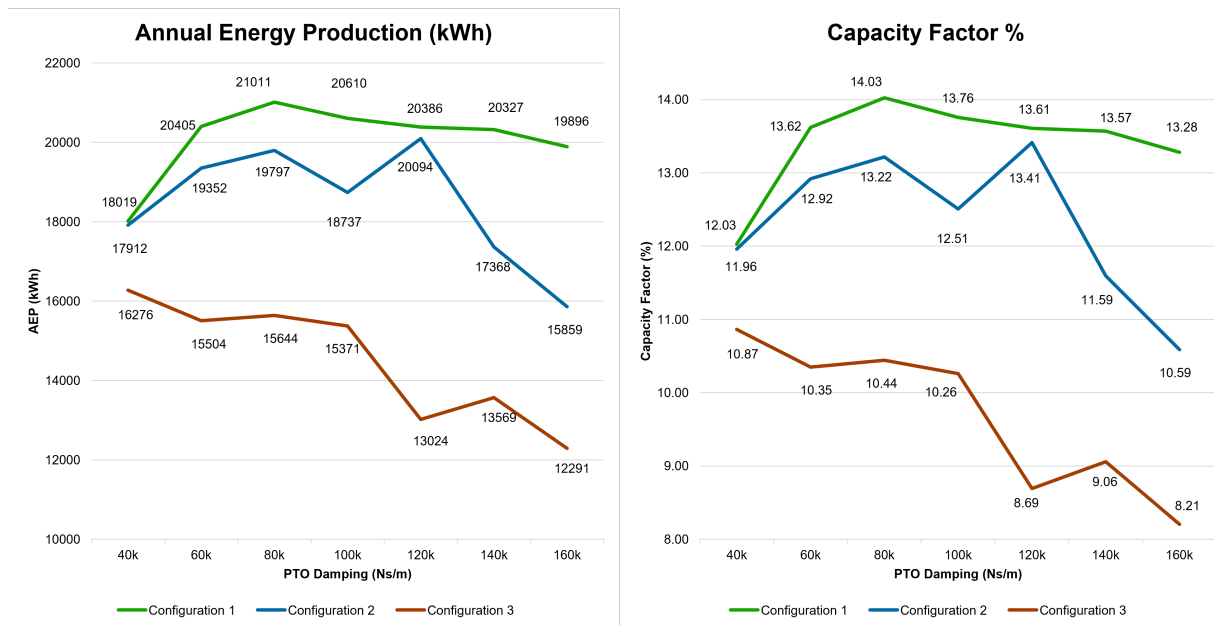


Figure 8.11: Mean annual energy production to its PTO damping and mass configurations

The capacity factor **CF** represents the ratio of mean absorbed power to the nominal capacity of the device and can be calculated using equation 8.1. This value seems to range between 12.03%-14.03% for the first WEC configuration and between 8.21%-10.87% for the third configuration. As can be seen from the power matrices, generally more power can be extracted at sea states with lower H_s and T_p using the first WEC configuration whereas for the other configurations the power output is more favourable at rougher sea states with a high H_s and T_p .

$$CF = \frac{AEP}{P_{rated} \cdot 8760} \quad (8.1)$$

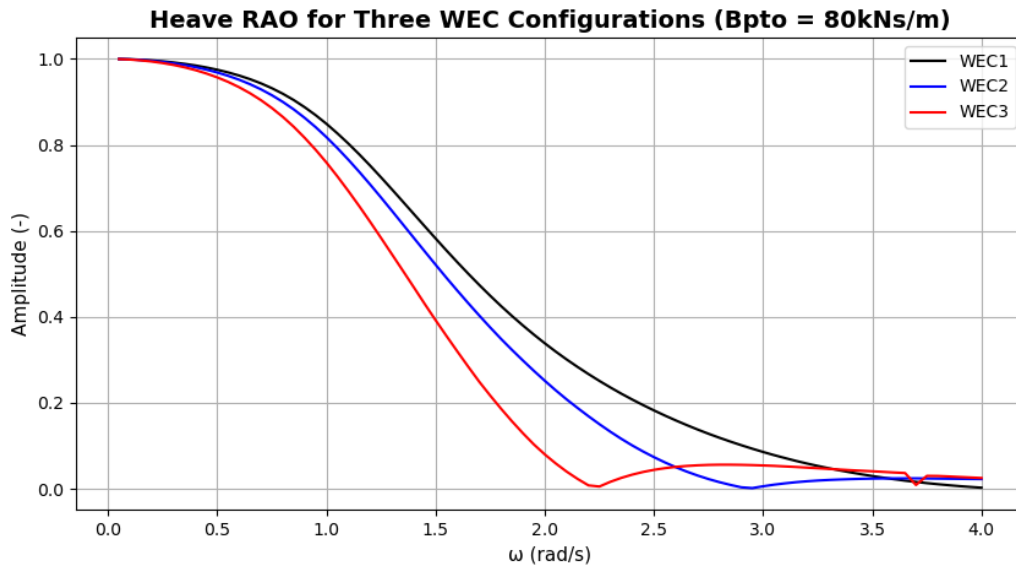


Figure 8.12: Heave RAOs for the three WEC configurations tuned to a PTO damping of 80 kN s m^{-1}

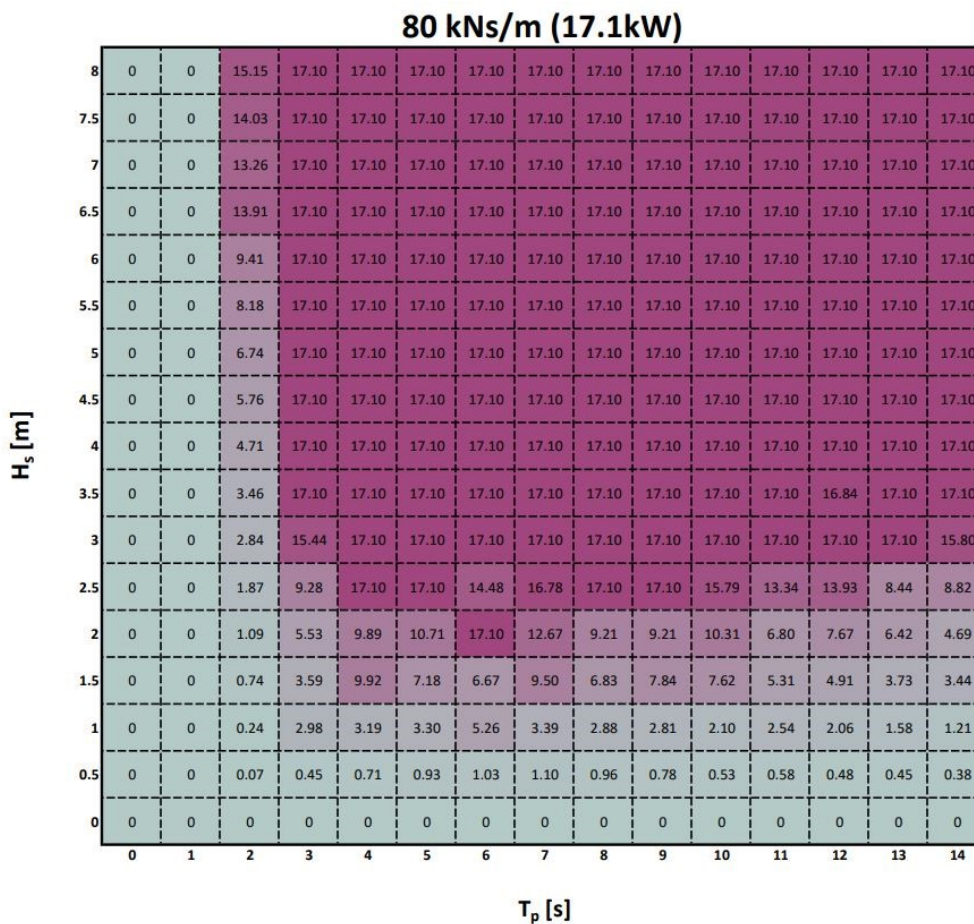


Figure 8.13: Power Matrix at optimal damping of 80 kN s m^{-1}

8.3.4. Discussion

One might wonder why the configuration where the systems natural frequency is closest to the natural frequency of the most occurring sea state as shown in figure 8.7 does not generate the most power for the WEC. Even when accounting for a higher nominal WEC capacity this is still not the case. One explanation for this is that the energy distribution across different wave frequencies in the sea state spectrum varies, and optimal power capture might not align solely with the most occurring sea state. For instance, a WEC with a broader frequency response can capture energy from a wider range of sea states, maximising its overall capture efficiency. Another factor to take into account is the PTO damping which affects the energy transfer from the oscillating WEC to the linear generator. The RAOs in figure 8.7 only show the undamped response of the three configurations while figure 8.12 shows the RAOs includes the PTO damping into the equation. Finding the right balance in PTO damping is crucial when trying to maximise energy capture while maintaining a responsive system. When the PTO damping is too high, then too much energy is dissipated, reducing the overall efficiency of the system. This would lead to a dampening of the peak in the response amplitude and a less responsive system. On the other hand, if the PTO damping is too low, the system may not effectively capture and convert the available wave energy. This would explain the variation that can be seen in Figure 8.11.

8.4. Seasonal Variability

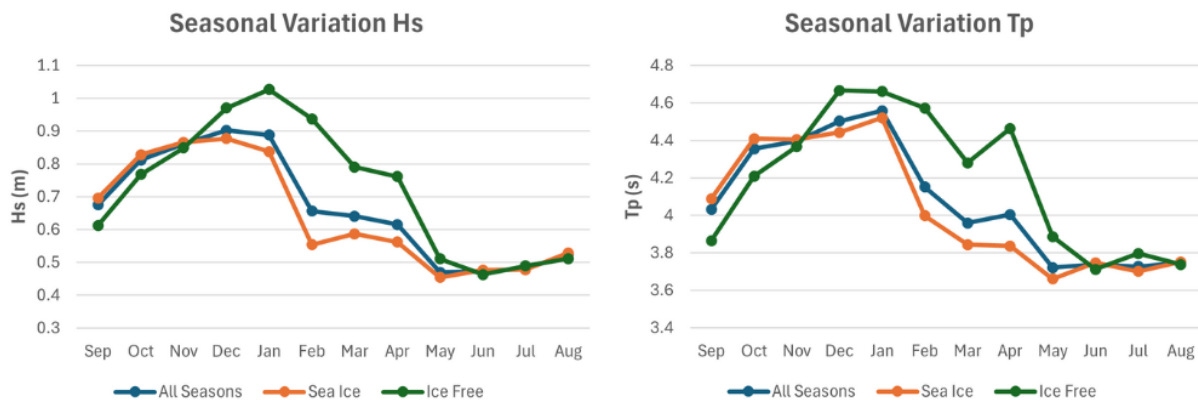


Figure 8.14: Average of the mean monthly significant wave height and peak period at site for seasons with sea ice presence and ice free seasons

The Baltic Sea is located in a region with warmer westerlies and colder polar easterlies which forms a belt of low pressures. As a result, a large seasonal variation can be seen in the wind field, as well as the wave climate. Higher wind speeds and a larger wave activity are observed during wintertime while lower wind speeds and lower wave heights are observed during the summer months [69]. This phenomenon is also depicted in Figure 8.14, where the highest recorded wave activity occurs during the months of December and January. Taking into account the presence of sea ice in this region however, affects these waves even more. Locally, the ice tends to grow starting from January and thawing around the months March to April. A clear deviation can be seen between the seasons subjected to ice cover compared to ice free seasons with the month of February experiencing a 40% decrease in the mean significant wave height due to ice cover. In addition, the waves become shorter with the mean peak period decreasing by about 13%. However, when looking at early autumn and the summer months the patterns agree fairly well with each other as it falls outside the months with ice cover. This in turn affects the available wave power that can be extracted for the WEC.

The four case seasons selected in chapter 6 can be divided and analysed on a monthly basis. To investigate the seasonal variability of power production, scatter diagrams are made for every month and multiplied by the optimal power matrix found in 8.3.3. As depicted in Figure 8.14, the waves show a decrease in height with an increasing sea ice presence. The monthly mean power production follows a similar pattern to the significant wave heights as a steady increase can be seen from early autumn up until the winter months (Figure 8.15). There is however, a noticeable dip in the year of 2009. This decline in mean power production for November 2009 can be explained by the presence of shorter and smaller waves during this period. Specifically, the 95th percentile of significant wave height (Hs) data points was below 1.25 meters in November, whereas it was below 2.25 meters in the previous month of October. Season 2019-2020 (Figure 8.16) reveals an interesting insight into the relationship between the presence of sea ice and the energy production. As there is no sea ice, power production remains steadily around the 4kW range throughout winter and spring and underscores the significance it has on power output.

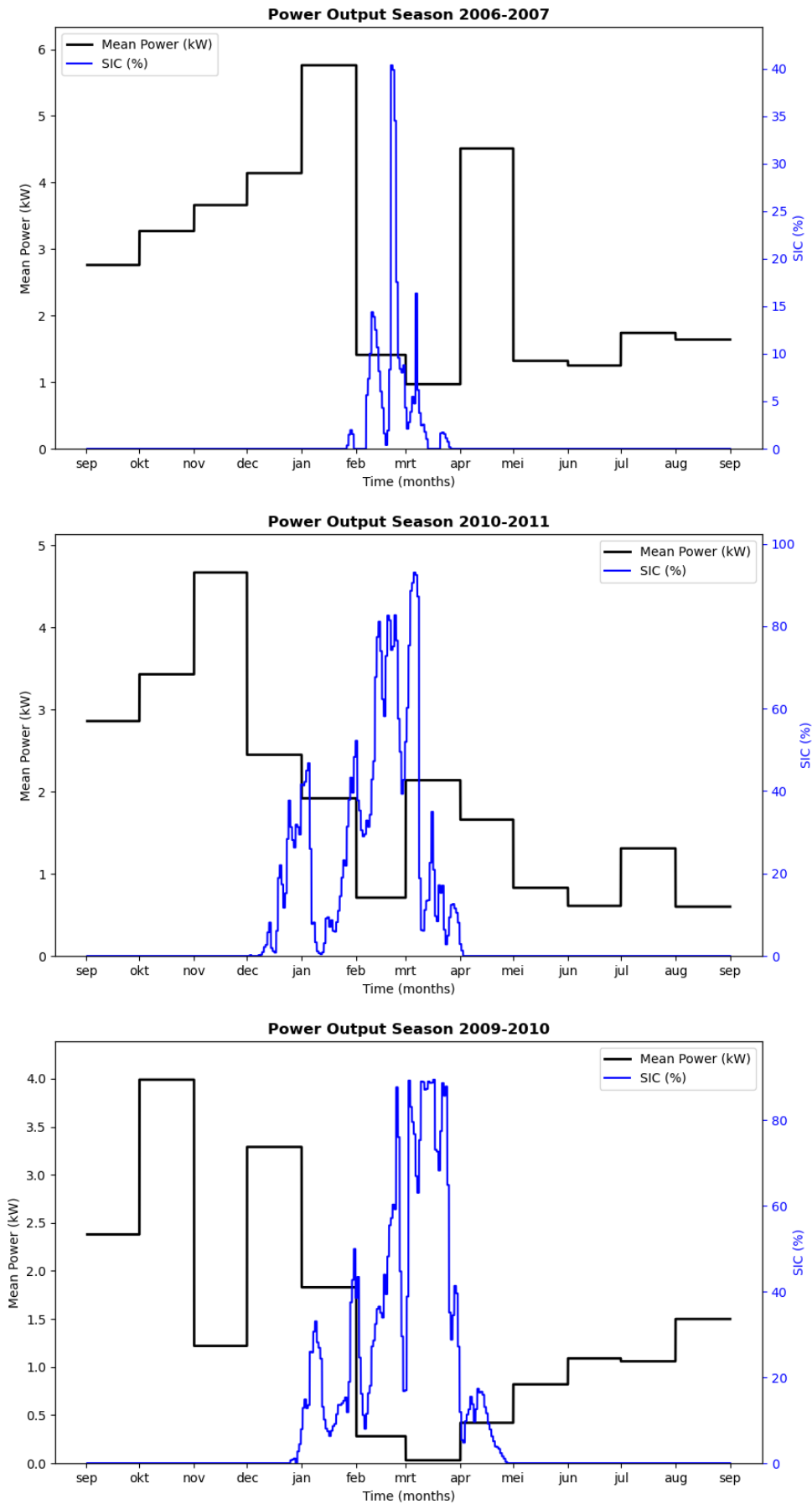


Figure 8.15: Monthly Mean Power Output for Seasons with Sea Ice, black line = Mean Power and blue line = Sea Ice Concentration (top to bottom: **Mild, Moderate, Severe Ice Conditions**)

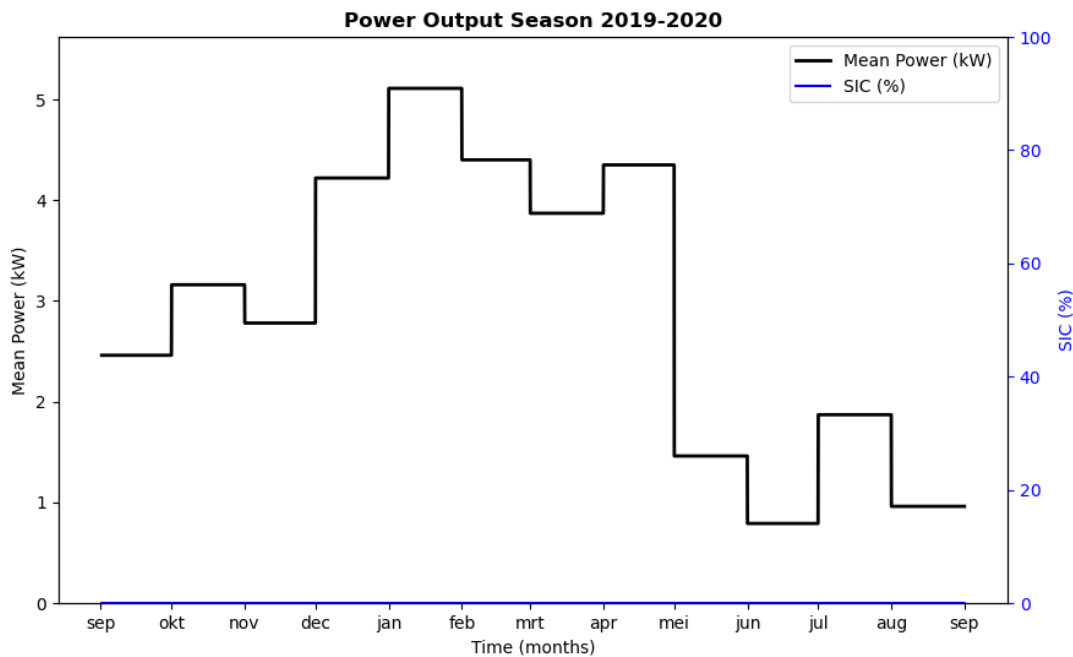


Figure 8.16: Monthly Mean Power Output Ice Free Season

Years	Ice Conditions	Mean Power (kW)	AEP (kWh)	CF (%)
2019-20	Ice Free	2.99	26225	17.51
2006-07	Mild	2.62	22920	15.30
2010-11	Moderate	1.91	16772	11.20
2009-10	Severe	1.53	13439	8.97
2006-21	Mixed	2.40	21011	14.03

Table 8.5: Overall energy production and the capacity factors for the specified cases

As a result, the overall power production for these seasons are listed in Table 8.5. The WECs capacity factor goes from 17.51 % for a very mild and ice free winter season and decreases to 8.97 % for the most severe winter season in this dataset. The long term wave statistics of 2006-2021 lead to a capacity factor of 14.03 % which comes close to the mild case winter season of 2006-2007 of 15.30 %.

8.5. Economics

In assessing the feasibility of wave energy converters it is necessary to take into consideration the financial and economic aspects in regards to the technology. According to Astariz et. al.[70], the main costs of a wave farm can be broken down into four costs namely; pre-operating costs, construction costs and decommissioning costs which form the **CapEx** and the operational expenditure which is known as the **OpEx**. The pre-operating costs considers all costs relating to preliminary studies, environmental impact assessment and procedures relating to permits and licensing prior to construction. The initial cost refers to the cost of the WEC devices as well as the other structures such as the necessary electric cables, substation, mooring system together with the total cost of installation. Depending on the parameters for the project, the costs may vary based on the type of converter, the location of deployment, the type of mooring, among other factors. In order to determine the cost of the electrical components it is necessary to select the type of power output. Alternating current power cables are easier to transform than direct current however it also leads to greater losses over larger distances. High voltage direct current is considered to

be the most effective at transporting energy but it is still very costly. Therefore, the best option for a wave plant is to use alternating current at distances less than 5 km to shoreline. Additionally, the layout of the wave farm as well as the construction of a substation will also need to be considered. The operation and maintenance cost (**OpEx**) must also be included in an economic analysis. This is a complicated process since experience is lacking and estimations must be based on experience from the oil and gas industry. The access to offshore WECs tends to be more difficult in comparison to wind farms as wave plants are generally deployed in more powerful wave climates as well as the device itself not remaining stationary. The levelised cost of energy (**LCOE**) for this point absorber is calculated using the financial **CapEx**, **OpEx** and the discount rate values based on cost estimations of similar wave energy projects from the literature and the annual energy production which comes as a result from the simulations. The **AEP** and the **LCOE** are calculated using the equations 2.5 and 2.6 from chapter 2.1.

8.5.1. CapEx & OpEx

The **CapEx** of the WEC itself, primarily consists of the price of the linear generator (foundation, casing, translator, and stator) and the construction costs. These costs can be estimated based on their masses and the material price per kg. It is assumed that steel costs 2.1 €/kg, concrete costs 125 €/m³ and copper costs 3 €/m [27]. The buoy made of steel is estimated to cost €6300 (2.1 €/kg·3000 kg) and the concrete foundation to cost €2600 (125€/m³·20.8m³). The costs of the linear generator is based on an economical model presented by Giassi et al.[27]. Construction cost involves labour costs and costs for the extra materials required. Table 8.6 shows a cost breakdown for the construction phase of the WEC. By adding the costs from Table 8.6, the total cost to manufacture one WEC comes down to €78,420.

Costs WEC	€
Buoy	6,300
Foundation	2,600
Casing	5,300
Translator	21,120
Stator	8,100
Construction	35,000

Table 8.6: Cost breakdown for a point absorber WEC with a direct-driven linear generator

In the economics of a wave energy park, the costs for the electrical systems need to be included. This includes the cost of the marine substations (costing around €10,000 for vessel hire and installation), which connect a cluster of WECs and the cost of the electrical cables; such as the power cable to shore, a communication cable and the inter-array cables. The cost of power cable installation is estimated to be around €72.5 per meter [27]. As the focus of this analysis is on a single absorb WEC and not a wave park, the associated electrical system costs are not considered. The offshore deployment of this type of WEC involves several essential steps [41]. Initially, the generator is assembled, factory and leakage tests are performed, and connections are made to deployment equipment. Following preparation, the WEC is transported to the port and to the deployment spot which includes a daily cost of approximately €10,000 for vessel hire[27]. Upon arrival, the WEC is pressurised, lifted and positioned on the seabed. The final step, involves using remotely operated vehicles (ROVs) or hiring divers to connect the necessary cables and to untie slings and shackles [41]. The daily cost for the hiring of divers is estimated to be about €8,000 [27]. For simplicity, the costs associated with decommissioning of the WEC are assumed to equal the costs of installation. To assess the economic viability, a sensitivity analysis is performed to examine the impact of varying the **CapEx** and **OpEx** on the Levelised Cost of Energy (**LCOE**). A range of values are given to the **CapEx** and **OpEx** representing the worst case to the most favourable scenario. Table 8.7 shows these scenarios expressed as percentages of the original **CapEx** that can be used to assess the sensitivity of the **LCOE** to fluctuations. As there is limited data available, it's common practice to estimate the annual operating expenditures (**OpEx**) as a percentage of the (**CapEx**). Here, the **OpEx** has been determined to be 8% of the **CapEx** [71]. This accounts for the costs relating to the maintenance and repair of the buoy and to components of the generator throughout its lifetime.

8.5.2. Levelised Cost of Energy (LCOE)

Scenario	CapEx per WEC	OpEx	LCOE (r=5%)	LCOE (r=10%)	LCOE (r=15%)
Worst +20%	€ 137,304.00	€ 10,984.32	1047 €/MWh	1290 €/MWh	1567 €/MWh
Worse +10%	€ 125,862.00	€ 10,068.96	960 €/MWh	1183 €/MWh	1436 €/MWh
Normal	€ 114,420.00	€ 9,153.60	873 €/MWh	1075 €/MWh	1306 €/MWh
Better -10%	€ 102,978.00	€ 8,238.24	785 €/MWh	968 €/MWh	1175 €/MWh
Best -20%	€ 91,536.00	€ 7,322.88	698 €/MWh	860 €/MWh	1045 €/MWh

Table 8.7: Sensitivity Analysis: Levelised Cost of Energy (LCOE) for different discount rates and cost scenarios ranging from worst to best

For the calculation of the **LCOE**, the **AEP** is a major parameter that influences its behaviour and using **AEP** based on data less than 10 years can lead to highly flawed estimations [72]. Therefore, this study uses the **AEP** based on data ranging from the years 2006-2021 for a reliable estimation. Another parameter considered in the sensitivity analysis is the discount rate r . As suggested by Lavidas and Blok [73], the discount rates for wave energy projects can be used to represent a social discount rate ($r:5\%$), a conventional to high risk investment rate ($r:10\%$) and a non-favourable extremely high risk investment rate ($r:15\%$). Given these discount rates a range of **LCOE** values are calculated going from 698 €/MWh to 1567 €/MWh.

Part V

Conclusion

Conclusion & Recommendations

This chapter summarises the work done and the results obtained. Using the results gathered, the research questions and sub-questions posed in section 3.3 are answered. In addition, recommendations for future research are given.

9.1. Conclusion

Research Question 1

How do ice floes and level ice affect the WEC and what are the implications for WEC survivability and energy production during these periods?

- *How do extreme level ice load cases affect the WEC, and what are the survival characteristics of the device under these conditions?*

The investigation into the impact of ice floes and level ice on WEC behaviour revealed significant effects on both survivability and energy production. Findings show that ice cover causes a dampening effect on waves, reducing the transferred momentum from air to the ocean surface. Additionally, ice-free areas experience a reduced effective wind fetch due to neighbouring ice-covered areas, further affecting wave energy capture. To assess survivability under ice conditions, literature revealed that a point absorber with an upward-facing slope of 60 degrees could withstand level ice thicknesses of up to 15 cm, reducing ice forces during the interaction process. A similar model was used in this study, on which the global ice forces on the WEC were calculated using the equations based on linear elastic beam theory in chapter 4, considering an ice thickness estimated from a 15-year dataset fitted to a Gumbel distribution with a 50-year return period. This revealed a horizontal design action of 615kN and a vertical design action of 315kN. Survival characteristics of the WEC under ice conditions include its ability to dive under the ice sheet, allowing it to withstand extreme ice loads. Extreme value analysis was used to assess survivability in waves, with the understanding that extreme wave forces and extreme ice loads do not occur simultaneously, eliminating the need for summation of both environmental forces. Using the environmental contour method, three design load cases were selected representing different extreme sea states and simulations were run in WEC-Sim. A maximum force of 134kN on the buoy is observed with a maximum response of 4.16m. In conclusion, these findings highlight the importance of designing WECs with a thicker hull to withstand ice interactions and the use of mitigation strategies such as active or passive submersion to maintain survivability in the presence of sea ice. Addressing these challenges, remains of importance for WEC survivability and is needed to ensure efficient energy production.

Research Question 2

What is the seasonal pattern of days with ice coverage, and how does this impact the overall energy output and the economic viability of a WEC investment, taking into consideration the lost energy production due to lack of waves?

The seasonal pattern of days of ice cover has been identified in Figures 8.15 and 8.16 with the dates of earliest sea ice freezing occurring on the 18th of December(2010) and the latest ice break-up occurring on the 16th of April(2010). The investigation has shown the effects of sea ice cover on the WEC's monthly power output across four distinct scenarios characterised by varying ice conditions; severe, moderate, mild and ice-free. The ice-free scenario serves as a valuable benchmark for comparing outcomes across different seasons. The overall power production showed a decrease of almost 50% for the season with severe ice conditions compared to the ice free season. As a result, this decrease strongly impacts the levelised cost of energy (**LCOE**), potentially leading to a 95% increase if derived solely from that single season. This highlights the significant influence of sea ice on both power production and economic viability.

- *What are the radiation damping, added mass, and stiffness coefficients of the WEC?*

The hydrodynamic coefficients are calculated using the boundary element method in the frequency domain for surge, heave and pitch motions of the WEC. These are computed using 'Capytaine' a Python package based on linear potential flow theory. These coefficients can be found in section 7.5.2. The hydrostatic stiffness coefficients can be found in section 8.3.1.

- *What are the RAOs (Response Amplitude Operators) of the WEC, and how do they impact the WEC's power output under various environmental conditions?*

The RAOs in surge, heave and pitch motion are computed using the obtained hydrodynamic coefficients and are shown in Figure 7.16. A high RAO value at a particular frequency range indicate that the WEC is better at extracting energy from those waves resulting in increased power output. Therefore, it is preferable to have the peak(s) close to the peak frequency of the waves. Currently, the WEC's natural frequency is higher than those of the waves resulting in operational range to be at the tail end of the most common wave spectrum. Three WEC configurations have been analysed by changing the translator mass and its power rating which in turn affects the RAOs and the natural frequency of the system. Despite a shift in the natural frequency, the results show that overall power production is greatest using the first WEC configuration (translator mass of 5 tonnes and power rating of 17.1kW). After tuning to the optimal PTO damping the heave RAOs are shown in Figure 8.12. A higher PTO damping results in more energy capture but a less responsive system, therefore a right balance of 80 kN s m^{-1} has been found in order to maximise the efficiency.

9.2. Recommendations

To get a better understanding of how the structure behaves during the ice interaction process, it could be modelled by employing a numerical ice model that captures the dynamic interaction between ice and structure, particularly for level ice conditions. Over the course of its operational lifetime, recurring ice actions could lead to fatigue failure which poses another problem. Additionally, it would be interesting to simulate how different ice features such as first year ice ridges would impact this structure, especially in regards to the connection line from the buoy to the generator. This could form further discussions around the mitigation measures. In addition, a detailed cost-benefit analysis could be done to determine the most cost-efficient mitigation measure (e.g. active vs passive submersion).

In terms of maximising energy production, it could be interesting to see what would happen using different control strategies such as reactive, latching and declutching control. Additionally, a similar case study could be performed for a different region exposed to seasonal ice coverage. Different research sites could be used to validate the findings of this thesis and allows for a broader discussion on this topic.

References

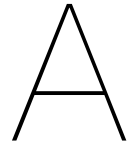
- [1] *2030 climate & energy framework*. https://ec.europa.eu/clima/eu-action/climate-strategies-targets/2030-climate-energy-framework_en. 2022. URL: https://ec.europa.eu/clima/eu-action/climate-strategies-targets/2030-climate-energy-framework_en.
- [2] *Offshore renewable energy*. https://energy.ec.europa.eu/topics/renewable-energy/offshore-renewable-energy_en. URL: https://energy.ec.europa.eu/topics/renewable-energy/offshore-renewable-energy_en.
- [3] Spyros Foteinis. “Wave energy converters in low energy seas: Current state and opportunities”. In: *Renewable and Sustainable Energy Reviews* 162 (July 2022), p. 112448. DOI: 10.1016/J.RSER.2022.112448.
- [4] Andreas Poullikkas. “Technology prospects of wave power systems”. In: *Electronic Journal of Energy & Environment* (Jan. 2014).
- [5] Dezhi Ning et al. *Modelling and Optimisation of Wave Energy Converters*. Taylor & Francis, 2022. URL: <https://library.oapen.org/handle/20.500.12657/57588>.
- [6] *Waveroller - AW-Energy*. <https://aw-energy.com/waveroller/>. URL: <https://aw-energy.com/waveroller/>.
- [7] Leo H. Holthuijsen. *Waves in oceanic and coastal waters*. Vol. 9780521860284. Cambridge University Press, Jan. 2007, pp. 1–387. DOI: 10.1017/CB09780511618536. URL: <https://www.cambridge.org/core/books/waves-in-oceanic-and-coastal-waters/F6BF070B00266943B0ABAFAEAE6F54465>.
- [8] Trevor Whittaker et al. “Nearshore oscillating wave surge converters and the development of Oyster”. In: *Philosophical Transactions of the Royal Society A: Mathematical, Physical and Engineering Sciences* 370 (1959 Jan. 2012), pp. 345–364. DOI: 10.1098/RSTA.2011.0152. URL: <https://royalsocietypublishing.org/doi/10.1098/rsta.2011.0152>.
- [9] Olga Kovaleva et al. “Hot-spots of large wave energy resources in relatively sheltered sections of the Baltic Sea coast”. In: *Renewable and Sustainable Energy Reviews* 74 (July 2017), pp. 424–437. DOI: 10.1016/J.RSER.2017.02.033.
- [10] Na Zhang et al. “Effects of sea ice on wave energy flux distribution in the Bohai Sea”. In: *Renewable Energy* 162 (Dec. 2020), pp. 2330–2343. DOI: 10.1016/J.RENENE.2020.10.036.
- [11] R.H. Stewart. *Introduction to Physical Oceanography*. University Press of Florida, 2009. URL: <https://books.google.se/books?id=3dXTRAAACAAJ>.
- [12] António F.de O. Falcão. “Wave energy utilization: A review of the technologies”. In: *Renewable and Sustainable Energy Reviews* 14 (3 Apr. 2010), pp. 899–918. DOI: 10.1016/J.RSER.2009.11.003.
- [13] Anthony Lewis et al. *Ocean Energy — IPCC*. Tech. rep. Intergovernmental Panel on Climate Change, 2012. URL: <https://www.ipcc.ch/report/renewable-energy-sources-and-climate-change-mitigation/ocean-energy/>.
- [14] *Electricity consumption – Electricity Information: Overview – Analysis - IEA*. <https://www.iea.org/reports/electricity-information-overview/electricity-consumption>. URL: <https://www.iea.org/reports/electricity-information-overview/electricity-consumption>.
- [15] B. Drew et al. “A review of wave energy converter technology”. In: *Proceedings of the Institution of Mechanical Engineers, Part A: Journal of Power and Energy* 223 (8 Dec. 2009), pp. 887–902. DOI: 10.1243/09576509JPE782.
- [16] Tunde Aderinto et al. “Ocean Wave energy converters: Status and challenges”. In: *Energies* 11 (5 2018). DOI: 10.3390/EN11051250.

- [17] International Renewable Energy Agency. *Ocean Energy: Technology Readiness, Patents, Deployment Status and Outlook*. Tech. rep. International Renewable Energy Agency, 2014. URL: www.irena.org/20https://www.irena.org/-/media/Files/IRENA/Agency/Publication/2014/IRENA_Ocean_Energy_report_2014.pdf.
- [18] António F.O. Falcão et al. “Oscillating-water-column wave energy converters and air turbines: A review”. In: *Renewable Energy* 85 (Jan. 2016), pp. 1391–1424. DOI: 10.1016/J.RENENE.2015.07.086.
- [19] *Mutriku Wave Power Plant | Tethys*. <https://tethys.pnnl.gov/project-sites/mutriku-wave-power-plant>. URL: <https://tethys.pnnl.gov/project-sites/mutriku-wave-power-plant>.
- [20] J. C.C. Portillo et al. “Backward bent-duct buoy or frontward bent-duct buoy? Review, assessment and optimisation”. In: *Renewable and Sustainable Energy Reviews* 112 (Sept. 2019), pp. 353–368. DOI: 10.1016/J.RSER.2019.05.026.
- [21] *OES. Oscillating Bodies*. <https://www.ocean-energy-systems.org/what-is-ocean-energy/waves/oscillating-bodies/>. URL: <https://www.ocean-energy-systems.org/what-is-ocean-energy/waves/oscillating-bodies/>.
- [22] Abigail Wachter et al. “Mathematical and numerical modeling of the AquaBuOY wave energy converter.” In: *Math. Ind. Case Study J.* 2 (Jan. 2010).
- [23] *Wave Star – Unlimited Clean Energy*. <https://wavestarenergy.com/>. URL: <https://wavestarenergy.com/>.
- [24] Erik Nilsson et al. “Assessment of Extreme and Metocean Conditions in the Swedish Exclusive Economic Zone for Wave Energy”. In: *Atmosphere* 11.3 (2020). DOI: 10.3390/atmos11030229. URL: <https://www.mdpi.com/2073-4433/11/3/229>.
- [25] *Pelamis Wave Power : EMEC: European Marine Energy Centre*. <https://www.emec.org.uk/about-us/wave-clients/pelamis-wave-power/>. URL: <https://www.emec.org.uk/about-us/wave-clients/pelamis-wave-power/>.
- [26] *Archimedes Waveswing - AWS Ocean Energy*. <https://awsocean.com/archimedes-waveswing/>. URL: <https://awsocean.com/archimedes-waveswing/>.
- [27] Marianna Giassi et al. “Economical layout optimization of wave energy parks clustered in electrical subsystems”. In: *Applied Ocean Research* 101 (2020), p. 102274. DOI: <https://doi.org/10.1016/j.apor.2020.102274>. URL: <https://www.sciencedirect.com/science/article/pii/S0141118720300869>.
- [28] Mirko Previsic et al. *International Levelised Cost of Energy for Ocean Energy Technologies*. Tech. rep. International Energy Agency, 2015. DOI: 10.13140/RG.2.2.34304.38407.
- [29] Nerijus Blažauskas et al. “Potential applications for small scale wave energy installations”. In: *Renewable and Sustainable Energy Reviews* 49 (Sept. 2015), pp. 297–305. DOI: 10.1016/J.RSER.2015.04.122.
- [30] Eeva Furman et al., eds. *The Baltic Sea Environment and Ecology*. English. SUOMEN YM-PÄRISTÖKESKUS, 2014. URL: [https://www.syke.fi/en-US/Publications/Brochures/The_Baltic_Sea_Environment_and_Ecology\(29197\)](https://www.syke.fi/en-US/Publications/Brochures/The_Baltic_Sea_Environment_and_Ecology(29197)).
- [31] Hanna Heino. *Utilisation of wave power in the Baltic Sea region*. Finland Futures Research Centre, 2013. URL: https://projects.centralbaltic.eu/images/files/result_pdf/WESA_result2_Utilization_of_Wave_Power.pdf%20https://projects.centralbaltic.eu/project/403-wesa.
- [32] Mats Walday et al. *The Baltic Sea — European Environment Agency*. https://www.eea.europa.eu/publications/report_2002_0524_154909/regional-seas-around-europe/BalticSea.pdf/view. URL: https://www.eea.europa.eu/publications/report_2002_0524_154909/regional-seas-around-europe/BalticSea.pdf/view.

- [33] Juri Elken et al. “Baltic Sea oceanography”. In: *Assessment of Climate Change for the Baltic Sea Basin. BALTEX Publication* (2008). URL: https://www.researchgate.net/publication/284270361_Baltic_Sea_oceanography.
- [34] *Hydrology -marinefinland.fi*. https://www.marinefinland.fi/en-US/Nature_and_how_it_changes/The_unique_Baltic_Sea/Hydrology. URL: https://www.marinefinland.fi/en-US/Nature_and_how_it_changes/The_unique_Baltic_Sea/Hydrology.
- [35] Anette Jönsson et al. “Variations in the Baltic Sea wave fields”. In: *Ocean Engineering* 30 (1 Jan. 2003), pp. 107–126. DOI: 10.1016/S0029-8018(01)00103-2.
- [36] Erland Strömstedt et al. “Project WESA (Wave Energy for a Sustainable Archipelago) - a Single Heaving Buoy Wave Energy Converter Operating and Surviving Ice Interaction in the Baltic Sea”. In: *In: Proceedings of the 10th European wave and tidal energy conference (EWTEC)* (2013).
- [37] Mats Granskog et al. “Sea ice in the Baltic Sea – A review”. In: *Estuarine, Coastal and Shelf Science* 70 (1-2 Oct. 2006), pp. 145–160. DOI: 10.1016/J.ECSS.2006.06.001.
- [38] International Organization for Standardization. *Petroleum and natural gas industries — Arctic offshore structures*. International Standard. Geneva, Switzerland: International Organization for Standardization, July 2018.
- [39] Finnish Meteorological Institute. *Sea ice statistics*. Accessed on July 12, 2023. 2022. URL: <https://en.ilmatieteenlaitos.fi/icestatistics>.
- [40] Erik Lejerskog et al. “Study of the operation characteristics of a point absorbing direct driven permanent magnet linear generator deployed in the Baltic Sea”. In: *IET Renewable Power Generation* 10.8 (2016), pp. 1204–1210. DOI: 10.1049/iet-rpg.2015.0413.
- [41] Maria Chatzigiannakou et al. “Offshore deployments of wave energy converters by Uppsala University, Sweden”. In: *Marine Systems & Ocean technology* 14 (June 2019), p. 3. DOI: 10.1007/s40868-019-00055-2.
- [42] Båtliv. *Film och bilder på islåget i Östersjön*. Accessed on June 11, 2023. Feb. 2011. URL: <https://www.batliv.se/2011/02/24/article3778/>.
- [43] Swedish Meteorological and Hydrological Institute. *Sea Ice*. Accessed on June 11, 2023. Mar. 2017. URL: <https://www.smhi.se/en/theme/sea-ice-1.11198>.
- [44] Andrej Savin et al. “Full-Scale Measurement of Reaction Force Caused by Level Ice Interaction on a Buoy Connected to a Wave Energy Converter”. In: *Journal of Cold Regions Engineering* 33 (June 2019). DOI: 10.1061/(ASCE)CR.1943-5495.0000175.
- [45] M. Karulina et al. “Full-scale flexural strength of sea ice and freshwater ice in Spitsbergen Fjords and North-West Barents Sea”. In: *Applied Ocean Research* 90 (2019), p. 101853. DOI: <https://doi.org/10.1016/j.apor.2019.101853>. URL: <https://www.sciencedirect.com/science/article/pii/S0141118718307004>.
- [46] Garry Timco et al. “A review of the engineering properties of sea ice”. In: *Cold Regions Science and Technology* 60 (Feb. 2010), pp. 107–129. DOI: 10.1016/j.coldregions.2009.10.003.
- [47] Ruth Branch et al. “Modeling Sea Ice Effects for Wave Energy Resource Assessments”. In: *Energies* 14.12 (June 2021), pp. 1–15. URL: <https://ideas.repec.org/a/gam/jeners/v14y2021i12p3482-d573622.html>.
- [48] Matt Folley. *Numerical modelling of wave energy converters*. Jan. 2016. DOI: 10.1016/c2014-0-04006-3. URL: <https://doi.org/10.1016/c2014-0-04006-3>.
- [49] Kelley Ruehl et al. *WEC-Sim v6.0*. Version v6.0. Oct. 2023. DOI: 10.5281/zenodo.10023797. URL: <https://doi.org/10.5281/zenodo.10023797>.
- [50] The Norwegian Meteorological Institute. *MET Norway*. <https://thredds.met.no/thredds/catalog.html>.

- [51] NOAA National Geophysical Data Center. *ETOPO1 1 Arc-Minute Global Relief Model*. NOAA National Centers for Environmental Information. Accessed 20-12-2023. 2009.
- [52] H. Haakenstad et al. “NORA3: A nonhydrostatic high-resolution hindcast of the North Sea, the Norwegian Sea, and the Barents Sea”. In: *Journal of Applied Meteorology and Climatology* (2021). DOI: 10.1175/JAMC-D-21-0029.1.
- [53] Konstantinos Christakos. *MET waves*. https://github.com/MET-OM/MET_waves/. 2021. URL: https://github.com/MET-OM/MET_waves/.
- [54] Ryan Coe et al. “Review of Methods for Modeling Wave Energy Converter Survival in Extreme Sea States”. In: (Apr. 2014).
- [55] SciPy Developers. *SciPy: Open Source Scientific Tools for Python*. <https://www.scipy.org/>. 2022.
- [56] Seongho Ahn. “Modeling mean relation between peak period and energy period of ocean surface wave systems”. In: *Ocean Engineering* 228 (2021), p. 108937. DOI: <https://doi.org/10.1016/j.oceaneng.2021.108937>. URL: <https://www.sciencedirect.com/science/article/pii/S0029801821003723>.
- [57] Georgii Bocharov. *pyextremes*. Version 2.3.2. Oct. 14, 2023. URL: <https://georgebv.github.io/pyextremes>.
- [58] Jessica Berg. *Extreme Ocean Wave Conditions for Northern California Wave Energy Conversion Device*. Report SAND2011-9304. Report for US Army Corps of Engineers. Sandia National Laboratories (SNL), 2011. URL: <https://doi.org/10.2172/1113856>.
- [59] A. F. Haselsteiner et al. “ViroCon: A software to compute multivariate extremes using the environmental contour method”. In: *SoftwareX* (2024). Accepted.
- [60] Matthieu Ancellin et al. “Capytaine: a Python-based linear potential flow solver”. In: *Journal of Open Source Software* 4.36 (Apr. 2019), p. 1341. DOI: 10.21105/joss.01341. URL: <https://doi.org/10.21105%2Fjoss.01341>.
- [61] Aurélien Babarit et al. “Theoretical and numerical aspects of the open source BEM solver NEMOH”. In: *Proceedings of the 11th European Wave and Tidal Energy Conference (EWTEC2015)*. Nantes, France, 2015.
- [62] Samrit Luoma et al. “Impacts of Future Climate Change and Baltic Sea Level Rise on Groundwater Recharge, Groundwater Levels, and Surface Leakage in the Hanko Aquifer in Southern Finland”. In: *Water* 6.12 (2014), pp. 3671–3700. DOI: 10.3390/w6123671. URL: <https://www.mdpi.com/2073-4441/6/12/3671>.
- [63] Iñaki Zabala et al. “BEMRosetta: An open-source hydrodynamic coefficients converter and viewer integrated with Nemoh and FOAMM”. In: Sept. 2021.
- [64] J.M.J. Journée et al. *Offshore Hydromechanics*. TU Delft, 2000. URL: <https://books.google.nl/books?id=eN66jwEACAAJ>.
- [65] *OES An International Evaluation and Guidance Framework for Ocean Energy Technology*. 2021. URL: <https://www.ocean-energy-systems.org/publications/oes-documents/guidelines/document/an-international-evaluation-and-guidance-framework-for-ocean-energy-technology/>.
- [66] Elie Al Shami et al. “Non-linear dynamic simulations of two-body wave energy converters via identification of viscous drag coefficients of different shapes of the submerged body based on numerical wave tank CFD simulation”. In: *Renewable Energy* 179 (2021), pp. 983–997. DOI: <https://doi.org/10.1016/j.renene.2021.07.068>. URL: <https://www.sciencedirect.com/science/article/pii/S0960148121010739>.
- [67] Maria Chatzigiannakou et al. “Offshore Deployments of Wave Energy Converters by Seabased Industry AB”. In: *Journal of Marine Science and Engineering* 5 (Mar. 2017), p. 15. DOI: 10.3390/jmse5020015.

- [68] James Prendergast et al. "A study on the effects of wave spectra on wave energy conversions". In: *IEEE Journal of Oceanic Engineering* 45.1 (Jan. 2020), pp. 271–283. DOI: [10.1109/joe.2018.2869636](https://doi.org/10.1109/joe.2018.2869636). URL: <https://doi.org/10.1109/joe.2018.2869636>.
- [69] Anette Jönsson et al. "Variations in the Baltic Sea wave fields". In: *Ocean Engineering* 30.1 (2003), pp. 107–126. DOI: [https://doi.org/10.1016/S0029-8018\(01\)00103-2](https://doi.org/10.1016/S0029-8018(01)00103-2). URL: <https://www.sciencedirect.com/science/article/pii/S0029801801001032>.
- [70] S. Astariz et al. "The economics of wave energy: A review". In: *Renewable and Sustainable Energy Reviews* 45 (2015), pp. 397–408. DOI: <https://doi.org/10.1016/j.rser.2015.01.061>. URL: <https://www.sciencedirect.com/science/article/pii/S1364032115000714>.
- [71] A. de Andres et al. "On the reversed LCOE calculation: Design constraints for wave energy commercialization". In: *International Journal of Marine Energy* 18 (2017), pp. 88–108. DOI: <https://doi.org/10.1016/j.ijome.2017.03.008>. URL: <https://www.sciencedirect.com/science/article/pii/S2214166917300334>.
- [72] G. Lavidas et al. "Shifting wave energy perceptions: the case for Wave Energy Converter (WEC) feasibility at milder resources". English. In: *Renewable Energy* 170 (2021), pp. 1143–1155. DOI: [10.1016/j.renene.2021.02.041](https://doi.org/10.1016/j.renene.2021.02.041).
- [73] G. Lavidas et al. "Levelised Cost of Electricity for wave energy converters and the perception of milder resource non-viability in the North Sea". English. In: *Proceedings of the 11th European Wave and Tidal Energy Conference*. 2021 European Wave and Tidal Energy Conference (EWTEC), EWTEC 2021 ; Conference date: 05-09-2021 Through 09-09-2021. EWTEC, 2021.



Ice Interaction Local Forces

A.1. Buoy-Ice interaction (project WESA)

Drifting ice fields can have considerable force on the wave energy converter. This could endanger the WEC, therefore it is necessary to find the best floating structure design that can survive ice action in the Baltic Sea. A design for a buoy is made taking into account that ice loads are mostly of dynamic nature. The buoy used in this analysis is based on the WECs used in project WESA and developed by Seabased AB and researchers at Uppsala University. As previously mentioned, two buoys were tested, the second buoy being an adaptation of the first buoy. For this research the second buoy is examined. The floating buoy is a 6 by 5 m hexagonal slope shaped torus (HSST) buoy made of steel with a weight of around 3 tonnes. The slope angle of the buoy is 60 degrees. The purpose of the slope is to get the maximum vertical downward force on the buoy from horizontal ice loads. Measurement equipment was installed in a tube that was built and integrated into the steel buoy for protection from the ice. The mode of failure was identified to be intermittent ice crushing at low ice velocities according to observations made from the station camera [44].



Station camera



Tower camera

Figure A.1: Observations from project WESA [44]

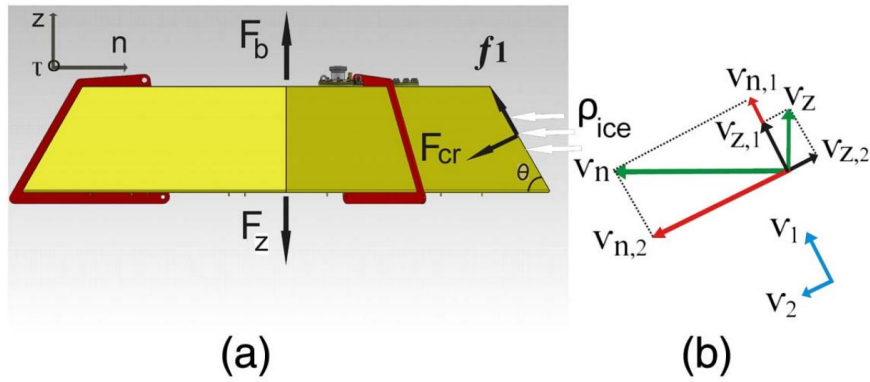


Figure A.2: Local contact forces on HSST buoy [44]

During buoy-ice interaction at least two sections of the hexagon shape come in contact with the level ice edge. If the ice action exceeds the bearing capacity of the ice some parts will begin to bow and flex. Due to the buoy's inclined design, some broken ice fragments slide across its surface and gather in front of and on top of the buoy. This could result in accumulation of ice rubble in front of the buoy. The buoy starts to move downwards, sinking beneath the ice from the vertical reaction forces [44]. From the figure A.2 it can be seen that the vertical reaction force, F_z , in downward direction can be calculated as:

$$F_z = F_{cr} \cos \theta + f_1 \sin \theta \tag{A.1}$$

- θ = slope angle of the structure
- F_{cr} = crushing force normal to the contact surface
- f_1 = friction force tangential to the contact surface

For a floating buoy the local contact forces can be calculated using the nodal velocity. To calculate the nodal velocity one can use a local coordinate system (τ, n, z) on the hull surface, that can be expanded into a tangential component, v_1 and a normal component, v_2 . The components can be seen in figure A.2(b). The local normal crushing force F_{cr} is given by the normal component v_2 to the hull surface and can be calculated using equation 4.5. The tangential components, v_1 and v_τ result in the vertical and horizontal friction forces, f_1 and f_τ . The tangential component v_1 can be calculated as:

$$v_1 = v_n \cos \theta + v_z \sin \theta \tag{A.2}$$

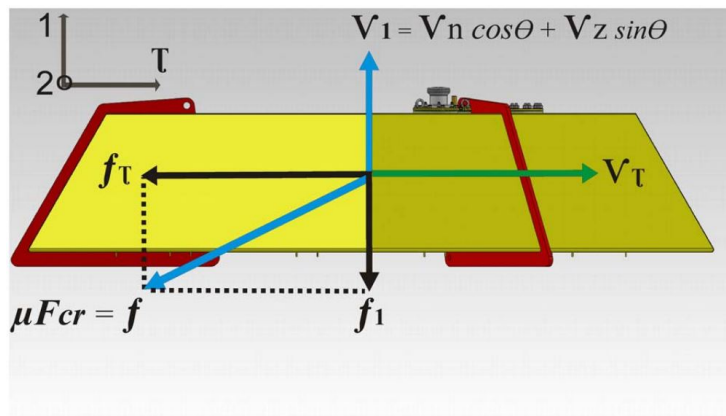


Figure A.3: Contact plane 1- τ [44]

It then follows that the vertical friction force f_1 becomes:

$$f_1 = -\mu F_{cr} \frac{v_1}{\sqrt{v_\tau^2 + v_1^2}} = -\mu F_{cr} \frac{v_n \cos \theta + v_z \sin \theta}{\sqrt{v_\tau^2 + (v_n \cos \theta + v_z \sin \theta)^2}} \quad (\text{A.3})$$

Lastly, the vertical reaction force on the WEC can be obtained by substituting equation A.3 equation A.1:

$$F_z = F_{cr} \left(\cos \theta - \mu \frac{v_n \cos \theta \sin \theta + v_z \sin^2 \theta}{\sqrt{v_\tau^2 + (v_n \cos \theta + v_z \sin \theta)^2}} \right) \quad (\text{A.4})$$

For the scope of this thesis, the main focus will be on a two-dimensional problem and neglect the change in relative vertical velocity for the ice actions. This simplifies equation for the vertical forcing accordingly:

$$F_z = F_{cr} \cos \theta - \mu F_{cr} \sin \theta \quad (\text{A.5})$$

Note that this simplified equation A.5 is similar to the vertical force equation 4.7 on the face of a sloping structure with the normal force N substituted by the local crushing force F_{cr} .

If the total downward vertical forcing exceeds the maximum buoyant force then as a result the buoy will go under the ice. The maximum buoyant force can be calculated using the mass of the displaced water. F_z represents the vertical reaction force due to ice interaction, F_b is the maximum buoyant force and F_g is the gravitational force.

$$F_z \geq F_b - F_g \quad (\text{A.6})$$



Capytaine and BEMIO

BuoyBEM.py: The Capytaine file (from WEC-Sim folder) used to compute and write the hydrodynamic and hydrostatic to a '.nc' file:

```
# setup environment
import os
os.environ["OMP_NUM_THREADS"] = "1"
import numpy as np
import sys

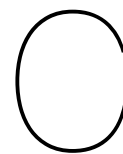
# Add directory with the call_capytaine.py file to the system path.
currentdir = os.path.dirname(os.getcwd())
sys.path.append(currentdir)
import call_capytaine as cc

# Define WEC parameters -----#
bem_file = ((os.getcwd() + os.path.sep + 'Buoy_BEM.dat'),) # mesh file
bem_cg = ((0,0,0.088549),) # center of gravity
bem_name = ('PointAbsorber',) # body name
bem_w = np.arange(0.05, 4.05, 0.05) # wave frequencies
bem_headings = np.linspace(0,np.pi/2,1) # wave heading
bem_depth = 25.0 # water depth
bem_ncFile = os.getcwd() + os.path.sep + 'Buoy_BEM.nc' # path for output .nc file
# -----#

# Run Capytaine
if __name__ == '__main__':
    cc.call_capy(meshFName = bem_file,
                 wCapy      = bem_w,
                 CoG        = bem_cg,
                 headings    = bem_headings,
                 ncFName     = bem_ncFile,
                 body_name   = bem_name,
                 depth       = bem_depth,
                 density      = 1005.0)
```

bemio.m: Boundary Element Method Input/Output (BEMIO) matlab file in WEC-Sim that writes the hydrodynamic and hydrostatic coefficients '.nc' file computed using Capytaine into a 'HDF5' file.

```
hydro = struct();  
hydro = readCAPYTAIN(hydro, 'Buoy_BEM.nc');  
hydro = radiationIRF(hydro, 60, [], [], [], []);  
hydro = radiationIRFSS(hydro, [], []);  
hydro = excitationIRF(hydro, 60, [], [], [], []);  
writeBEMIOH5(hydro)  
plotBEMIO(hydro)
```



WEC-Sim

To create a power matrix the following two scripts are used. The input file is used to define the simulation parameters, the waves, the body and the WEC PTO parameters. **wecSimInputFile.m**:

```
%%% Simulation Data
simu = simulationClass(); % Initialize Simulation Class
simu.simMechanicsFile = 'CADcog.slx'; % Location of Simulink Model File
simu.solver = 'ode4'; % simu.solver = 'ode4' for fixed step
simu.mode = 'normal'; % 'normal', 'accelerator', 'rapid-accelerator'
simu.explorer='off'; % Turn SimMechanics Explorer (on/off)
simu.startTime = 0; % Simulation Start Time [s]
simu.rampTime = 100; % Wave Ramp Time Length [s]
simu.endTime=400; % Simulation End Time [s]
simu.dt = 0.1; % Simulation time-step [s]

%% Wave Information
% Irregular Waves
waves = waveClass('irregular'); % Initialize Wave Class and Specify Type
waves.height = 0.0:0.5:8; % Wave Height [m]
waves.period = 0:14; % Wave Period [s]
waves.spectrumType = 'JS'; % Specify Spectrum Type

wave_height= waves.height;
wave_period= waves.period;
num_height = length(waves.height);
num_period = length(waves.period);

%% Body Data
% Float
body(1) = bodyClass('../hydroData/cadwaterline.h5'); % Initialize bodyClass for Float
body(1).geometryFile = '../geometry/cadcog.stl'; % Geometry File
body(1).mass = 'equilibrium'; % Mass [kg]
body(1).inertia = [4806 4806 9120]; % [kg*m^2]

%% PTO and Constraint Parameters
% Translational PTO
pto(1) = ptoClass('PTO1'); % Initialize PTO Class for PTO1
pto(1).stiffness = 0; % PTO Stiffness [N/m]
pto(1).damping=80e3; % PTO Damping [N/(m/s)]
pto(1).location = [0 0 0]; % PTO Location [m]
```

The following script writes the power matrix (in kW) to a .csv file based on simulations for each sea state:
UserDefinedFunctionsMCR.m:

```
%Store data

mcr.Avgpower(imcr) = mean(output.ptos.powerInternalMechanics(2000:end,3));
mcr.CPTD(imcr) = pto(1).damping;

close all

% Script for last MCR case
if imcr == length(mcr.cases)
    H = mcr.cases(:,1);
    T = mcr.cases(:,2);
    P = abs(mcr.Avgpower);

    % Intermediary step before rotating counterclockwise 90 degrees
    O = reshape(P,num_period,num_height);
    power_matrix = rot90(O);
    power_matrix_kW = power_matrix/1000;
    writematrix(power_matrix_kW,'power_matrix_kW.csv')
end
```



Wave Scatter Diagrams

After extracting time series for the significant wave height H_s and peak period T_p the .csv files can be used to create wave scatter diagrams for that time period. The following lines of code was used in Python:

```
import numpy as np
import scipy as sp
import matplotlib.pyplot as plt
import pandas as pd

Hs = np.genfromtxt('Data/2019-2020/hs_NORA3.csv', delimiter=',', skip_header=1,
usecols=(1))
Tp = np.genfromtxt('Data/2019-2020/tp_NORA3.csv', delimiter=',', skip_header=1,
usecols=(1))

# Define the bin range
Tp_bins = np.arange(-0.5, 15.5, 1)
Hs_bins = np.arange(-0.25, 12.75, 0.5)

statistic, xedges, yedges, binnumber = sp.stats.binned_statistic_2d(Tp, Hs,
values=None, statistic='count', bins=[Tp_bins, Hs_bins])

# Create a meshgrid
x, y = np.meshgrid(xedges, yedges)

# Total count of data
total_count = np.sum(statistic)

# Creating the DataFrame
# the [::-1] command flips the order of the rows where the positive vertical
# direction is upwards instead
wavescattertable = pd.DataFrame(statistic.T[::-1] / total_count,
index=[12.0, 11.5, 11.0, 10.5, 10.0, 9.5, 9.0, 8.5, 8.0, 7.5, 7.0, 6.5, 6.0,
5.5, 5.0, 4.5, 4.0, 3.5, 3.0, 2.5, 2.0, 1.5, 1.0, 0.5, 0.0],
columns=[0, 1, 2, 3, 4, 5, 6, 7, 8, 9, 10, 11, 12, 13, 14])
print(wavescattertable)

# Save to csv file
wavescattertable.to_csv("wavescattertable.csv")
```

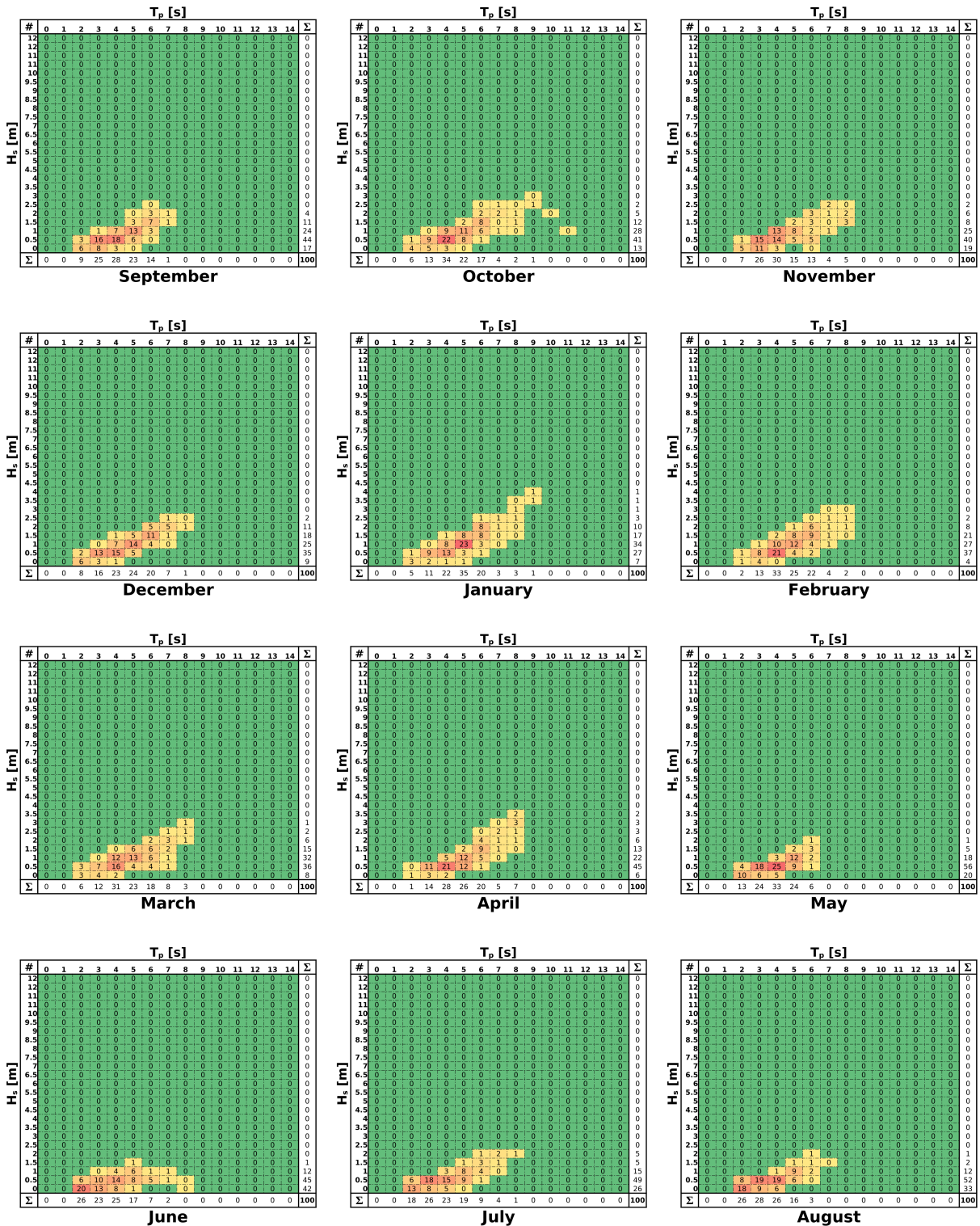


Figure D.1: Monthly wave scatter diagram season 2019-2020 Ice Free

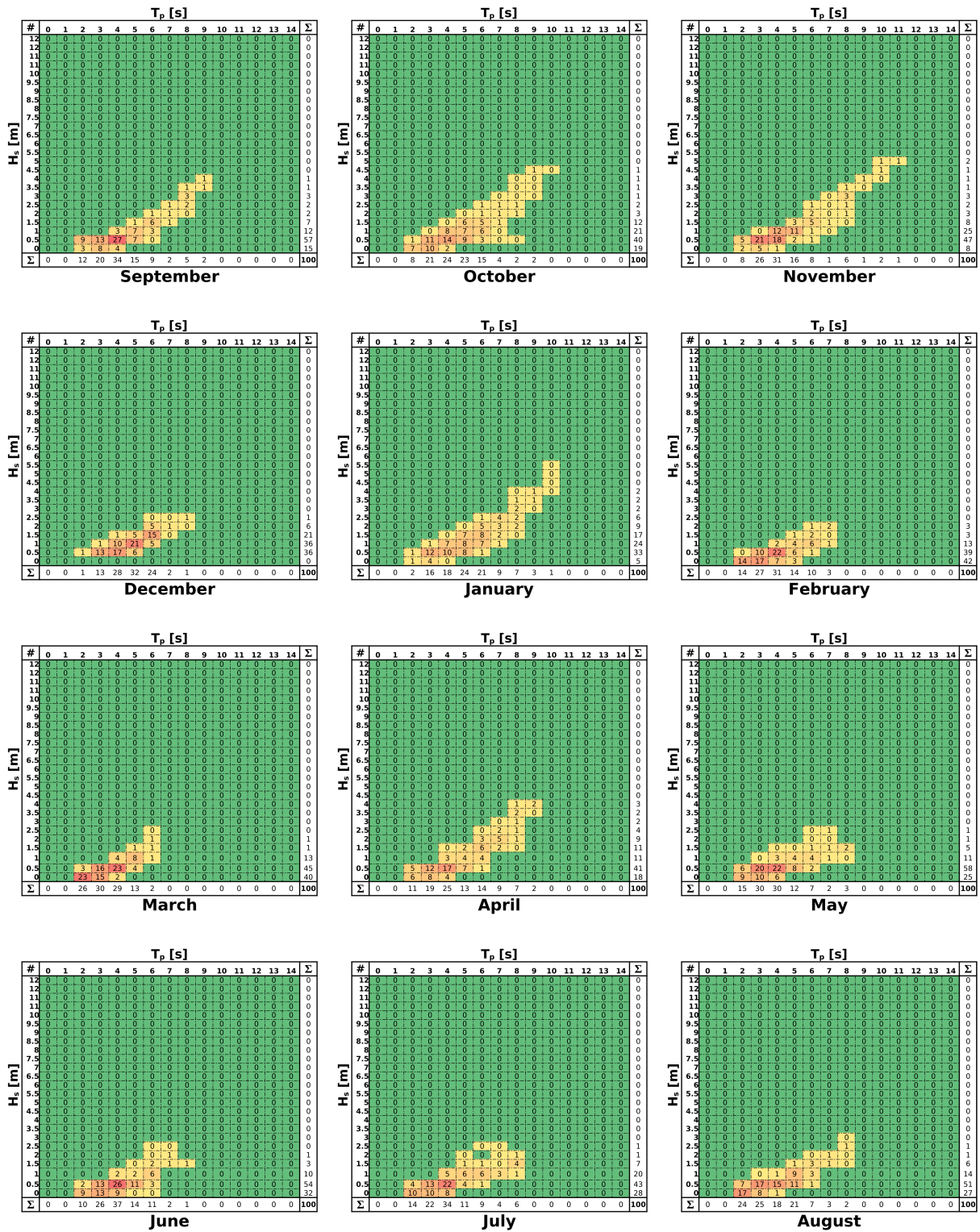


Figure D.2: Monthly wave scatter diagram season 2006-2007 Mild Ice Conditions

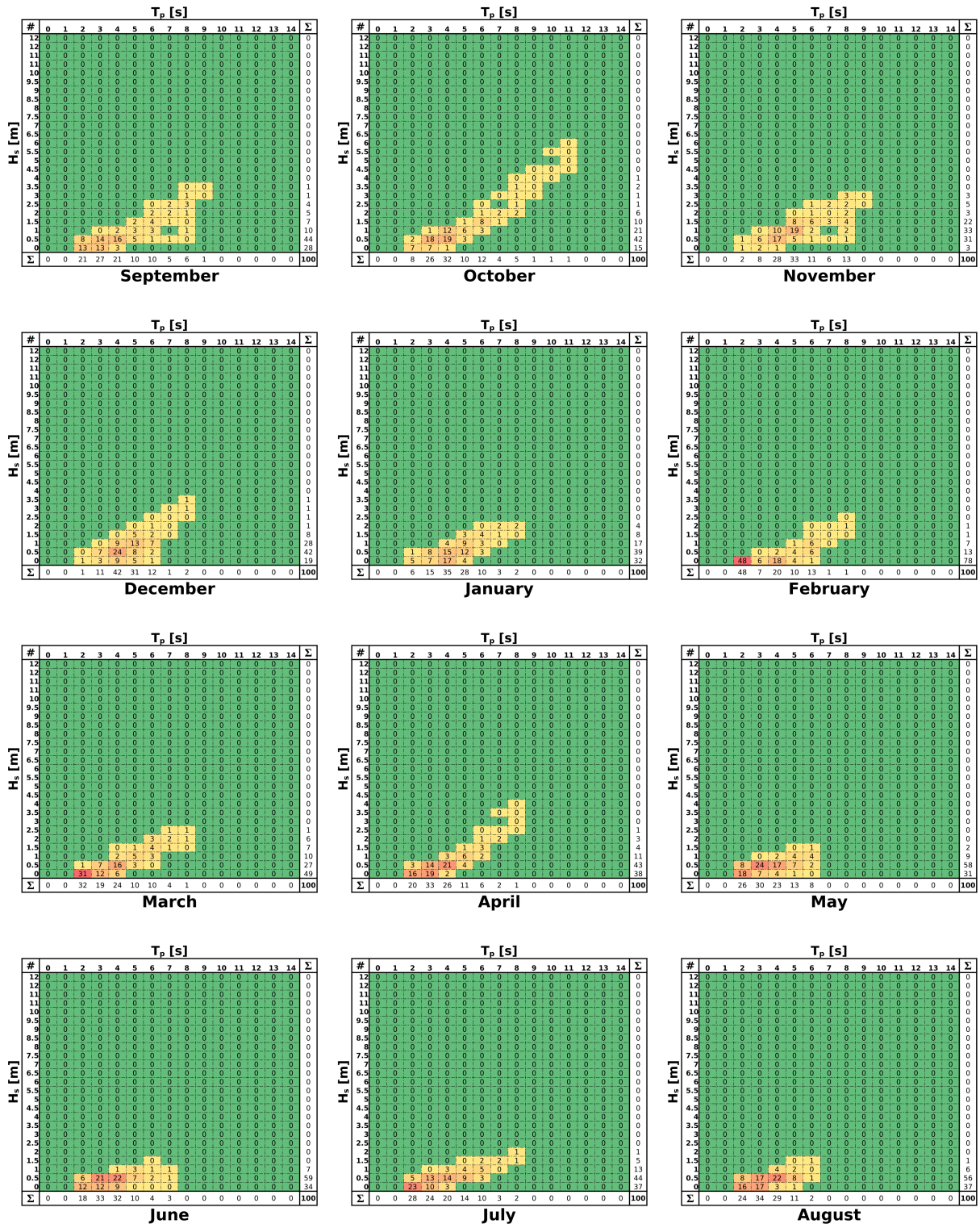


Figure D.3: Monthly wave scatter diagram season 2010-2011 Moderate Ice Conditions

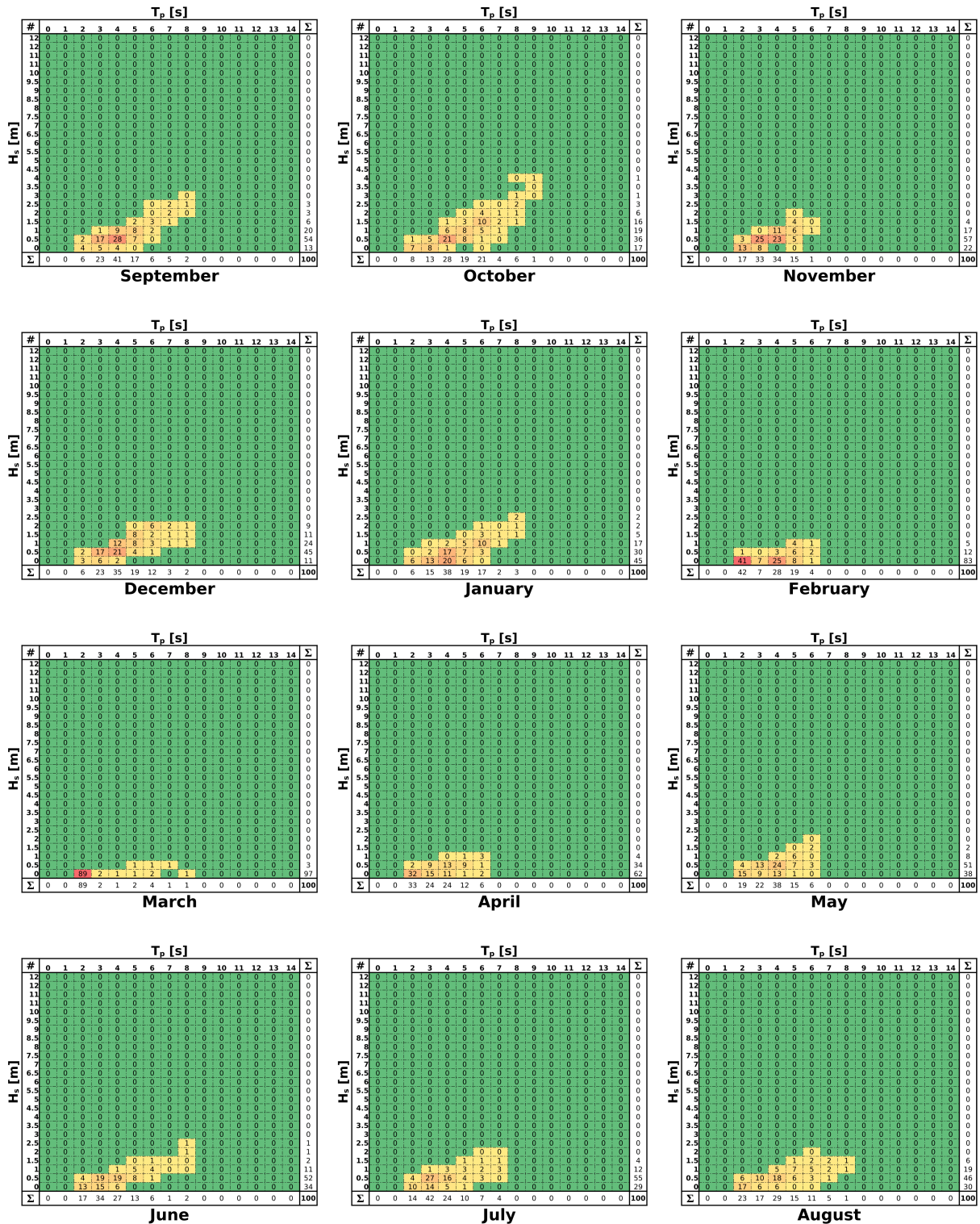


Figure D.4: Monthly wave scatter diagram season 2009-2010 Severe Ice Conditions